Faculteit Wetenschappen

Departement Bio-ingenieurswetenschappen

Een studie van plasmon systemen met Layer-by-Layer gesynthetiseerde core-shell nanodeeltjes

Proefschrift voorgelegd tot het behalen van de graad van doctor in de bio-ingenieurswetenschappen aan de Universiteit Antwerpen door

Ramesh Asapu

Promotoren:

Prof. dr. Silvia Lenaerts

Prof. dr. ir. Sammy Verbruggen

Antwerpen, 18th September 2018

Faculty of Science

Department of Bioscience Engineering

A study of plasmonic systems using Layer-by-Layer synthesized core-shell nanoparticles

Thesis submitted to obtain the doctorate degree in
Bioscience Engineering at the University of Antwerp by

Ramesh Asapu

Members of the jury:

Prof. Dr. Ir. Siegfried Denys	(President) University of Antwerp
Prof. Dr. Silvia Lenaerts	(Promotor) University of Antwerp
Prof. Dr. Ir. Sammy Verbruggen	(Promotor) University of Antwerp
Prof. Dr. Dirk Lamoen	University of Antwerp
Prof. Dr. Christophe Detavernier	Gent University
Prof. Dr. Sara Bals	University of Antwerp
Dr. Anshuman Awasthi	Mercedes-Benz R&D India

Antwerp, 18th September 2018

Samenvatting

De toepassing van plasmon nanodeeltjes heeft zijn weg gevonden in meerdere onderzoeksdomeinen zoals zonnecellen, plasmon versterkte fotokatalyse, Raman-spectroscopie en biofotonica. Plasmon materialen hebben een specifieke eigenschap die oppervlakte plasmon resonantie (SPR) wordt genoemd, waarbij een invallende lichtstraal een oscillerende elektronenwolk creëert. Goud en zilver worden het vaakst onderzocht omdat ze SPR over een breed golflengtegebied vertonen en hun SPR-eigenschappen kunnen worden afgestemd zodat de straling van de zon kan gebruikt worden. De toepassing van plasmon nanodeeltjes op het gebied van verontreinigingsbeheersing en alternatieve energie heeft geholpen bij het overwinnen van de nadelen die samenhangen met conventionele UV licht TiO_2 fotokatalyse. In het afgelopen decennium werd wijdverspreid onderzoek verricht naar plasmon-versterkte halfgeleidende fotokatalyse vanwege hun unieke kenmerken - het verbeteren van het ladingsscheidings- en overdrachtsproces en het verhogen van de absorptie van zichtbaar licht. De mechanismen die verantwoordelijk zijn voor de verbetering van de fotokatalytische efficiëntie zijn een versterkt elektrisch veld, elektronenoverdracht en verbeterde foton-absorptie.

Het doel van dit proefschrift is om de belangrijkste mechanismen te bestuderen die verantwoordelijk zijn voor Ag-TiO_2 en Au-TiO_2 plasmon versterkte fotokatalytische systemen. Om dit te bereiken werd een plasmon versterkt fotokatalytisch systeem zodanig gesynthetiseerd dat zilver/goud en TiO_2 nanodeeltjes contac maken via een scheidingslaag. De dikte van de isolerende scheidingslaag werd vergroot om het elektrische veld uit te sluiten, terwijl een geleidende scheidingslaag, die dik genoeg is om het elektrisch veld uit te sluiten, de elektronenoverdracht mogelijk maakt. Het idee van mechanisme-verheldering werd in detail beschreven in het inleidingshoofdstuk met een korte bespreking van luchtverontreiniging en fotokatalyse. Daarom worden in het eerste hoofdstuk zilver-polymeer kern-schil nanodeeltjes gesynthetiseerd met behulp van de colloïdale laag-na-laag (LbL)

methode. De dikte van de polymeermantel die ook de scheidingslaag is, wordt op nanoschaal gecontroleerd, typisch in de orde van minder dan één nanometer. Deze zilver-polymeer kern-schil nanodeeltjes werden afgezet op dunne TiO_2 (Degussa P25) films. De activiteit van de aldus gesynthetiseerde films werd getest met aceetaldehyde, een typische organische polluent in binnenlucht. Een diepgaande analyse van de ultrastabiele zilver-polymeer kern-schil nanodeeltjes bestond uit verschillende karakteriseringstechnieken. Fotokatalytische activiteitsmetingen toonden aan dat Ag-TiO_2 systemen stabieler waren wanneer polymeer ingekapselde zilveren nanodeeltjes werden gebruikt. Elektromagnetische modellering en simulaties werden uitgevoerd in het tweede hoofdstuk met het COMSOL Multiphysics®-programma. Theoretische berekeningen met behulp van de Mie-theorie werden ook uitgevoerd om het effect van de polymeerlaag op de optische eigenschappen van zilver nanodeeltjes te bestuderen. Als volgende stap werden meerdere pogingen ondernomen om geleidende polyelektrolyt scheidingslagen te synthetiseren om ladingsoverdracht mogelijk te maken. Het was echter niet succesvol omdat het in-situ polymerisatieproces een lage pH had als vereiste voor initiatie van de polymerisatie en zilver colloidale nanodeeltjes waren zeer reactief en onstabiel onder dergelijke omstandigheden. In het vierde hoofdstuk werd Raman spectroscopie gebruikt als een experimenteel bewijs ter ondersteuning van de simulaties die het concept uitleggen dat veldversterking beschikbaar is binnen een afstand van twee nanometer van het oppervlak van Au en Ag nanodeeltjes. In het vijfde hoofdstuk werd een mechanistische benadering toegepast op Au-TiO_2 systemen met behulp van een geleidende of een isolerende scheidingslaag met afstembare dikte. Vergelijking van de fotokatalytische degradatie van stearinezuur door verschillende Au-TiO_2 systemen verschafte de hypothese dat de twee belangrijkste mechanismen, directe elektronenoverdracht en elektromagnetisch veld geïnduceerde ladingdragergeneratie, een synergetisch effect hebben op de fotokatalytische efficiëntie. In het laatste hoofdstuk worden alle resultaten van dit proefschrift samengevat en worden de toekomstperspectieven van de bevindingen van deze studie gepresenteerd.

Abstract

The application of plasmonic nanoparticles has found its way in multiple domains of research such as solar cells, plasmonic photocatalysis, Raman spectroscopy and biophotonics. Plasmonic materials possess a specific property called surface plasmon resonance (SPR). The SPR property of noble metal nanoparticles is a unique phenomenon, which is an oscillation of electron cloud generated in the close vicinity of nanoparticle, when in resonance with the incident electromagnetic radiation. Among the noble metals that exhibit surface plasmon resonance, gold and silver are most commonly investigated as they display SPR over a wide wavelength range and their SPR properties can be fine-tuned to utilize the visible light spectrum of the abundant solar radiation. The application of plasmonic nanoparticles in photocatalysis has found wide applications in the fields of pollution control and alternative energy; and has helped in overcoming the long existing problem to utilize the photocatalysts in a wide light spectrum and overcome the drawbacks associated with conventional UV light TiO_2 photocatalysis. Since the past decade, widespread research is being done on plasmon-enhanced semiconductor photocatalysis because of their unique features - enhancing the charge separation and transfer process and increasing the visible light absorption. The mechanisms responsible for enhancement of photocatalytic efficiency are near-electric field, electron transfer and enhanced photon absorption, which are the major ones depending on the design of nanoscale systems.

The objective of this thesis is to study the major mechanisms responsible for Ag-TiO_2 and Au-TiO_2 plasmonic photocatalytic systems. To accomplish this, a plasmonic photocatalytic system was fabricated in such a way that silver/gold and TiO_2 nanoparticles are in contact through a spacer layer. The insulating spacer layer thickness was increased to rule out the near-electric field whereas a conductive spacer layer thick enough to exclude near-electric field allows the electron transfer. The idea of mechanism elucidation was described in detail in the introduction chapter with a brief review on air pollution and photocatalysis. Consequently, in the second chapter,

silver-polymer core-shell nanoparticles are synthesized using colloidal layer-by-layer (LbL) method. The thickness of the polymer shell that forms the spacer layer is controlled at nanoscale level, typically in the order of less than one nanometre, which is supported by transmission electron microscopy measurements. These silver-polymer core-shell nanoparticles were deposited on TiO_2 (Degussa P25) thin films. The activity of the as prepared films was tested with a gas phase pollutant acetaldehyde, which is an indoor volatile organic compound. In depth analysis of the stability of the silver-polymer core-shell nanoparticles were performed by heat treatment, salt ion tests and conductivity measurements. Compared to the silver nanoparticles, silver-polymer core-shell nanoparticles had better optical properties and stability in oxidative or ambient conditions. Photocatalytic activity measurements showed that Ag-TiO_2 plasmonic photocatalytic systems were more stable when polymer encapsulated silver nanoparticles were used. Electromagnetic modelling and near-field simulations performed in third chapter using COMSOL Multiphysics® program also supported this hypothesis. Theoretical calculations using Mie theory were also done to corroborate the effect of polymer shell on the optical properties of silver nanoparticles. As a next step, multiple attempts were made to synthesize conductive polyelectrolyte spacer layer/shell to allow for charge transfer. However, it was not successful as the in-situ polymerization process had low pH as a requirement for the initiation of polymerization and, silver colloidal nanoparticles were highly reactive and unstable under such low pH conditions.

In the fourth chapter Raman spectroscopy was used as an experimental evidence to support the near-field simulations explaining the concept that near-field enhancement is available at a distance of less than two nanometres form the surface of Au and Ag nanoparticles. In the fifth chapter, a mechanistic approach was applied to Au-TiO_2 plasmonic photocatalytic system, using the idea of a conducting and insulating spacer layer with tuneable thickness. The insulating spacer layer is the shell of the gold-polymer core-shell nanoparticle synthesised using LbL method. The conductive spacer layer is the polyaniline shell synthesized using in-situ polymerization

of aniline in gold colloidal solution. The synthesized core-shell nanoparticles were characterized using spectrophotometric, conductive-tip AFM and TEM techniques. Comparison of the photocatalytic degradation of stearic acid by different Au-TiO_2 plasmonic photocatalytic systems provided the model reaction to clarify on different mechanisms. The major mechanisms i.e., direct electron transfer and near-field induced charge-carrier generation have a synergetic effect boosting the efficiency of gold-plasmon enhanced photocatalysis. In the final chapter, the results of this thesis are summarized and the future prospects of applying the findings of this study are presented.

This thesis is dedicated to my mother to whom I owe everything.

"అమ్మ" కి అంకితం

"There is something about losing a mother that is permanent and inexpressible – a wound that would never quite heal" – Susan Wiggs

Acknowledgements

I would like to express deep appreciation and respect for my promotors Prof. Dr. Silvia Lenaerts and Prof. Dr. Ir. Sammy W. Verbruggen for their continuous encouragement, support, and guidance during the entire period of my doctoral program. I am extremely thankful to Prof. Dr. Ir. Siegfried Denys for his support with COMSOL Multiphysics modeling and simulation program without which this thesis would be incomplete. I am grateful to Prof. Dr. Christophe Detavernier and Prof. Dr. Sara Bals for giving me the opportunity to work on the ALDFOTOKAT and GOA projects and providing the financial support for my research.

I am very grateful to Nathalie (EMAT, University of Antwerp) for providing the crucial analysis with transmission electron microscopy, which is one of the significant components of this thesis. I would also like to thank Prof. Dr. Pegie Cool and Radu (LADCA, University of Antwerp) for Raman spectroscopy measurements; Matthias (CoCooN, Gent University) and Sree (COK, KU Leuven) for providing crucial samples with respect to collaboration in ALDFOTOKAT project. The kind and friendly support from all the colleagues of DuEL had made my four years of stay in Belgium a memorable part of my life and I would carry some beautiful memories back home. A special note of thanks to Tom for his support in the gas lab and Hilde for her tireless helping nature in the chemical lab.

Finally, I would like to thank all my family members for their support throughout my doctoral studies. I am forever indebted to my parents Basavaraju and Mahalakshmi, for their endless love and moral support. I would also like to express deepest gratitude to my brother Siva for his guidance and advice, sisters Sunitha and Sirisha for their unwavering affection and care, throughout my life. Last but not the least, to my dear wife Sushma - I am thankful for your love and affection that kept me in a joyful state in contrast to an otherwise serious and complicated world of doctoral research work.

Table of Contents

List of Figures

List of Tables

Symbols and Abbreviations

3D	Three-dimensional
a.u	Arbitrary units
Abs.	Absorbance
Ag	Silver
Ag_LX	Silver nanoparticles encapsulated with X (X=0/4/6/8/12) number of polymer layers
a_n, b_n	Scattering coefficients in Mie theory
AQI	Air Quality Index
Au	Gold
Au_LX	Gold nanoparticles encapsulated with X (X=0/4/8/12) number of polymer layers
C-AFM	Conductive tip atomic force microscopy
C_{ext}, C_{sca}, C_{abs}	Extinction, scattering and absorption cross sections of a particle in Mie theory
CO_2	Carbon dioxide
C_{surf}, C_{norm}	Concentration of Raman probe dye solution in surface enhanced mode and normal mode respectively
DET	Direct electron transfer
DPSS	Diode-pumped solid-state laser
E / E-field / $\vec{E}$	Electric field of electromagnetic radiation
E_0, E_{inc}	Incident electric field
e^-	Electron
E_{cb}, E_{vb}, E_{red}	Energy levels of conduction band, valance band and reduction potential respectively
EF	Enhancement factor
e^-- h^+	Electron-hole pair
FDT	Full diamond tip
FEM	Finite element method
FWHM	Full width at half maxima

h	Planck's constant (value = 6.626 x 10^{-34} m^2Kg/s)
$\vec{H}, \vec{H}^*$	Magnetic field vector and its complex conjugate respectively
H, H_{inc}	Magnetic field at a point and of incident electromagnetic radiation respectively
h^+	hole / electron hole
HAADF-STEM	High-angle annular dark-field scanning transmission electron microscopy
HVAC	Heating ventilation and air conditioning
IDE	Interdigitated electrode
Int.	Intensity
I_{surf}, I_{norm}	Intensity of Raman signal in surface enhanced mode and normal mode respectively
IV	Current-Voltage
K	Refractive index number - imaginary part or extinction coefficient
K_0	Wavenumber in free space
LbL	Layer-by-Layer
l_m, l_{mb}	Mean free path length of conduction band electrons in gold nanoparticle and bulk gold respectively
LSPR	Localized surface plasmon resonance
m	Relative refractive index, ratio of refractive index of different media in Mie Thoery
n	Refractive index number - real part
NASA	National aeronautical space administration
NEFCG	Near-electric field induced charge carrier generation
NOx	Nitrogen oxides
NP	Nanoparticle
N_{surf}, N_{norm}	Number of molecules probed in surface enhanced mode and normal mode respectively
P25_AgLX	Titanium oxide nanoparticles loaded with silver-polymer core-shell nanoparticles, where X=number of polymer layers encapsulating the silver core, i.e., X=0/4/8/12
PAA	Polyacrylic acid

PAH	Polyallylamine hydrochloride
PANI	Polyaniline
PCO	Photocatalytic oxidation
PM_{10}, $PM_{2.5}$	Particulate matter with mean particle size of 10 and 2.5 µm respectively
PML	Perfectly matched layers
PSS	Polystyrene sulfonate
Ref	Reference
R6G	Rhodamine 6G dye used as Raman probe compound
S_{inc}, S_{sca}, S_{ext}	Poynting vector/energy flux at a point in incident, scattered and extinction wave mode respectively in Mie theory
SERS	Surface enhanced Raman spectroscopy
SEM	Scanning electron microscopy
SHE	Standard hydrogen electrode
Sim	Simulated values
SOx	Sulfur oxides
SPR	Surface plasmon resonance
TEM	Transmission electron microscope
TiO_2	Titanium dioxide / titanium oxide(IV)
TiO_2_AuL0/4/8/12	Titanium oxide nanoparticles loaded with gold-polymer core-shell nanoparticles where X in LX represents polymer layer, i.e., X = 0/4/8/12
TiO_2_AuPANI30/180	Titanium oxide nanoparticles loaded with gold-polyaniline core-shell nanoparticles where PANIX represents polymerization time X = 30/180 minutes
TiO_2_ref	Titanium dioxide nanoparticle film used for reference measurements
UHV	Ultra high vacuum
UV	Ultraviolet
UV-vis	Ultraviolet – visible
VOC	Volatile organic compound
V_{surf}, V_{norm}	Volume of Raman dye solution (R6G) used in surface enhanced and normal mode respectively

W_{abs}, W_{sca}, W_{inc}, W_{ext}	Rate of electromagnetic energy absorbed, scattered, incident and extinction modes respectively in Mie theory
$Z_0, Z0\_const$	Impedance of free space ~ 120π or 376.73 Ω
c	Speed of light / speed of electromagnetic radiation in vacuum
$\hat{e}, \hat{e}_r$	Direction vector of incident and scattered electromagnetic radiation respectively.
$ewfd.Q_h$	Power dissipation density variable in the built-in variable list of COMSOL Multiphysics®
$ewfd.relPoav_{x,y,z}$	Poynting vectors / time averaged power field in x, y and z-axes in the built-in variable list in wave optics module of COMSOL Multiphysics®
ε_r, ε_0	Permittivity of the medium and in free space respectively
n_x, n_y, n_z	x, y and z component of refractive index in COMSOL Multiphysics®
$\hat{n}$	Unit vector normal to imaginary sphere in Mie theory
η	Characteristic wave impedance of material, defined as $\sqrt{\mu_r/\varepsilon_r}$
k	Wavenumber defined as $2\pi/\lambda$ for electromagnetic radiation
λ_{inc}	Wavelength of incident light wave/electromagnetic radiation
λ_{spr}	Surface plasmon resonance wavelength
ξ_n, ψ_n	Ricatti-Bessel functions in Mie theory
μ_r, μ_0	Permeability of the medium and in free respectively
ν	Frequency of electromagnetic wave propagation
x	Size parameter in Mie theory
σ	Electrical Conductivity of material in S/m
ω	Angular frequency of the electromagnetic radiation

Chapter 1

Introduction:

A brief review on air pollution, photocatalysis and an approach for mechanistic study of plasmon-enhanced photocatalysis

"Research is what I'm doing when I don't know what I'm doing." – Werner Von Braun

1.1 *Air pollution*

"Somewhere something incredible is waiting to be known" - Carl Sagan, is an apt quote for every field of science, it applies to either an invention for human advancement or discovering a phenomenon caused by human influence resulting in decline of our environment. During the rapid industrialization period of the post second world war era, it was incredible to believe that human activity was causing air quality deterioration in the cities throughout the world. Nowadays air pollution has become one of the major causes for concern. World Health Organization defines air pollution as "contamination of the indoor or outdoor environment by any chemical, physical or biological agent that modifies the natural characteristics of the atmosphere"[1]. The health issues associated with living in an environment with bad air quality can lead to numerous health issues such as respiratory and cardiac diseases, central nervous system disorders, stroke and lung cancer[1–5]. It is reported that annually around seven million premature deaths are caused by air pollution and results in even more cases of sickness and hospitalization[2,6–9]. Air pollution not only effects the human health, but it also has adverse effects on the ecosystems leading to localized climate change and reduction in crop yields[10,11]. Both indoor and outdoor air pollution are a serious cause for concern with significant number of deaths in millions are linked to them[2].

The initial steps to remediation and mitigation is monitoring followed by identifying the point sources of air pollution. The primary cause for indoor air pollution are volatile organic compounds released by the building materials, electronics and improper ventilation. Indoor air quality could be improved by proper circulation of fresh air and installation of air filters in the HVAC (Heating, Ventilation and Air Conditioning) lines of the building. Tighter regulations on the type of materials being used for building constructions is improving upon the indoor air quality factor[12]. The major pollutants responsible for outdoor air pollution are carbon dioxide, sulfur oxides (SOx), nitrogen oxides (NOx), carbon monoxide, particulate matter, which are called the primary pollutants. Secondary pollutants such as ozone and smog form due to

photochemical factors i.e., the interaction of UV radiation from sunlight and primary pollutants such as VOCs and NOx[13]. The sources for air pollution are both anthropogenic and natural. Some of the natural sources of air pollution are volcanic activity, wildfires, dust storms etc.; surprisingly, recent research has revealed VOC emissions from plants too[14,15]. The anthropogenic sources are mainly industrial and vehicular emissions, but also come from large-scale forest burning for agricultural and animal feedlots. In the recent decades, research[16–20] has revealed that one of primary pollutants, carbon dioxide, has forced the world to reconsider the use of fossil fuels for our energy needs. For thousands of years the concentration of carbon dioxide (CO_2) has been within the 200-280 ppm levels and crossed the 400 ppm mark after the post second world war industrialization period in the 1950s as studied by NASA[21] graphic shown in Figure 1.1. The increase in carbon dioxide levels has been successfully linked with the rise in global average temperatures by many research studies. One such graphic is shown in Figure 1.2, which shows the global temperature changes for the past 160 years that clearly shows a rise in global average temperature.

Apart from CO_2, pollutants such as SOx and NOx that are released from industrial and vehicular emissions, VOCs, ozone and particulate matter (PM) have become a serious hazard for urban air quality. Particulate matter is suspended air particulates which are composed of organic/inorganic particles that are small enough to be inhaled along with air and water including mineral dust, smoke, pollen and soot. PM is additionally divided into two subcategories based on the mean aerodynamic diameter i.e., PM 2.5 - particles of size less than or equal to 2.5 µm and PM10 - particles of size between 2.5 µm and 10 µm [13,22–24]. $PM_{2.5}$ particularly poses a very serious threat to human health as very small particulates can penetrate deep into the lung tissues and enter the blood stream, because of which WHO has designated $PM_{2.5}$ as a Group 1, carcinogen[4,25,26]. Numerous research studies have associated elevated PM levels in the urban areas with increased mortality rates and serious health disorders[23,27–30]. Air quality index (AQI) is a number indicator, which is being used throughout the world nowadays to monitor the air quality in the urban areas.

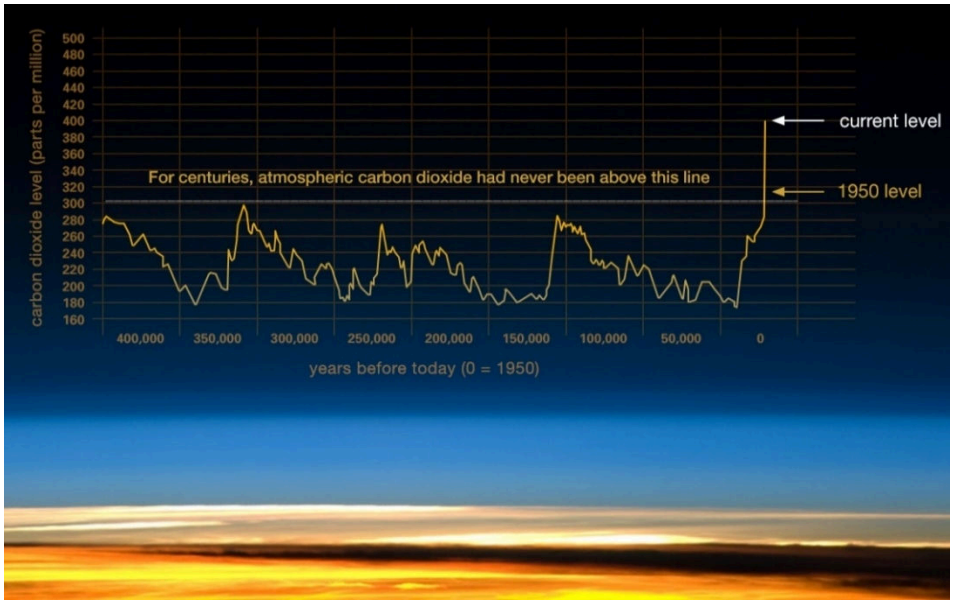

Figure 1.1. CO_2 levels for the past 400,000 years compiled from multiple research studies by NASA. Adapted from Ref.[21]

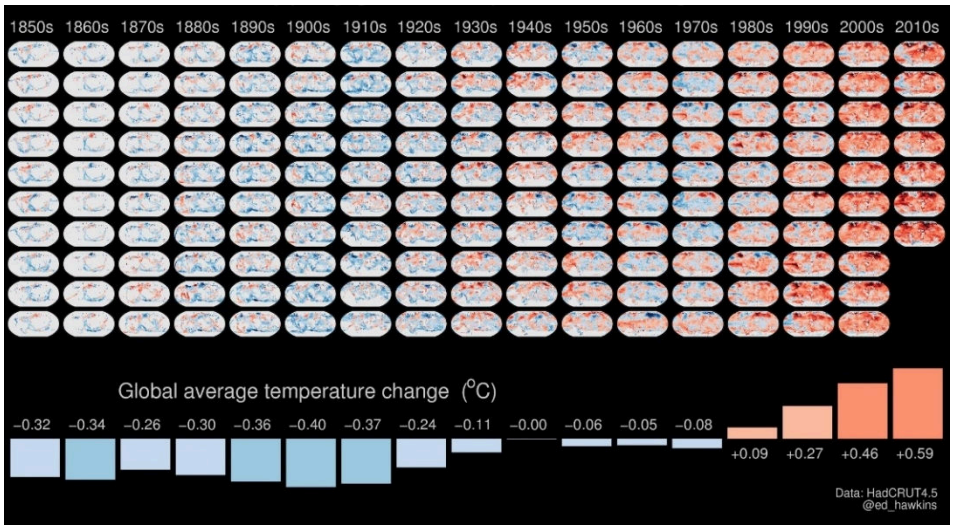

Figure 1.2. Mapping of global average temperature change on a world map from 1850-2017. Adapted from illustration by Prof. Ed Hawkins, University of Reading, UK[31].

AQI compares the prevailing levels of pollution in an area with a standard limit of exposure to pollutants on a daily average basis. These maximum permissible limits vary as per different regions, government agencies and organizations, some of which are listed in the Table 1.1.

	$PM_{2.5}$	PM_{10}	NO_2	SO_2	Ozone
WHO[4]	10*/25**	20*/50**	40**	20**	100#
EU[32]	25*	40*/50**	40*/200##	125**	120#
Japan[33]	15*/35**	100**	40-60**	40**	60##
US EPA[34]	15*/35**	150**	53*	75##	70#
China[35]	15*/35**	40*/50**	40*/80**	20*/50**	100#
India[36]	40*/60**	60*/100**	40*/80**	50*/80**	100#

*Annual mean, **24-hour mean, #8-hour mean and ## 1-hour mean values in $\mu g/m^3$

Table 1.1. Air quality standards as outlined by different organizations.

As it can be observed that most of the standards set up by different organizations vary significantly but they only serve as guidelines for local government to identify the areas with unhealthy ambient air quality. The air quality index (AQI) is categorized to indicate how the prevailing levels of pollutants deviate from the standard limits. Therefore, the AQI provides a much simpler way of communicating with the public to know the ambient air quality in localized areas. A map of the European AQI is shown in the Figure 1.3 and the color legend corresponds to the pollutant levels of AQI listed in Table 1.2. The indices also vary with the location as per the monitoring agencies, but a number of social enterprise projects were started in last decade to standardize the AQI with a "World air quality index" by mapping the pooled data from public and private air monitoring stations[37–39]. One such project (aqcin.org) which is based in Beijing, China has collaborations around the world and accesses data from over 10,000 air quality monitoring stations in 800 metropolitan cities from 70 countries. A snapshot of the world air quality map as shown in Figure 1.4 shows that severe air pollution has become ubiquitous, especially in the developing countries in Asia. Countries such as India and China, who have adopted rapid industrialization by meeting the energy needs through fossil fuels, are bearing the brunt as air quality worsens.

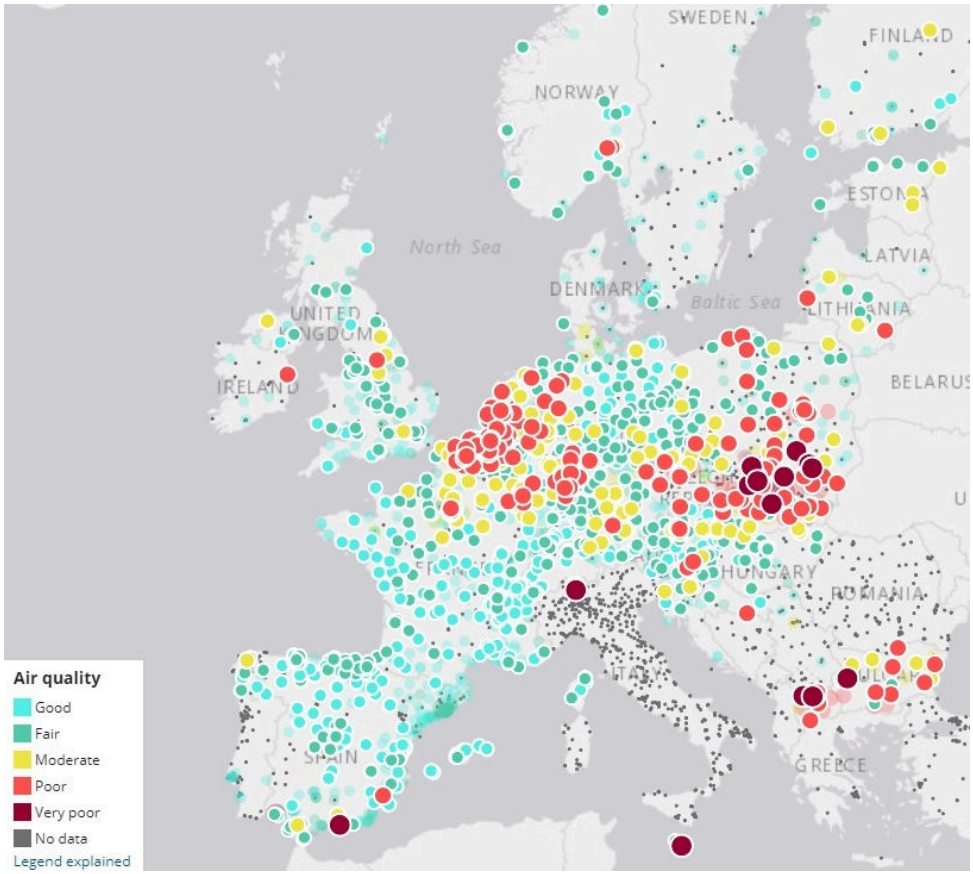

Figure 1.3. European air quality index map. Image acquired with mean values of AQI averaged over a period of 24-hours[40] http://airindex.eea.europa.eu/

Pollutant	Index level (based on pollutant concentrations in µg/m³)				
	Good	Fair	Moderate	Poor	Very poor
Particles less than 2.5 µm ($PM_{2.5}$)	0-10	10-20	20-25	25-50	50-800
Particles less than 10 µm (PM_{10})	0-20	20-35	35-50	50-100	100-1200
Nitrogen dioxide (NO_2)	0-40	40-100	100-200	200-400	400-1000
Ozone (O_3)	0-80	80-120	120-180	180-240	240-600
Sulphur dioxide (SO_2)	0-100	100-200	200-350	350-500	500-1250

Table 1.2. The European air quality index is categorized and the corresponding color coding used in the mapping of air quality index in Figure 1.3. Table adapted from Ref.[40]

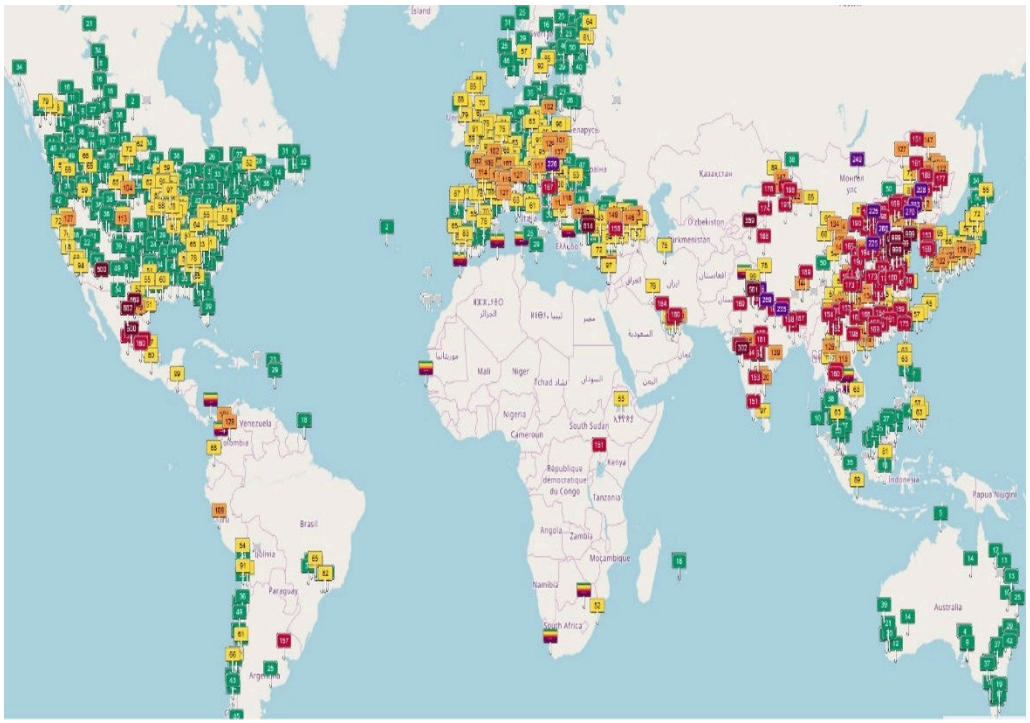

Figure 1.4. World mapping of air quality index, the scale of green as good and deep red as hazardous.[37]

It can also be observed that much of the African countries either lack the resources necessary for air monitoring stations or have no policy in place to monitor air quality. It is reported that more than 92% of world population lives in places, which are exposed to unhealthy ambient air quality. Around 88% of the premature deaths because of the air pollution occurs in low-middle income countries[4]. The initial counter measure to address the air pollution problem is to identify the point sources of pollutants. In developing countries of Southeast Asia, incineration of agricultural wastes and stubble burning is also a leading contributor of smog in the cities during the post-harvest seasons. In the developed countries of western European region, vehicular and industrial emissions are one of the major sources for air quality deterioration. Many successful strategies could be implemented to reduce the air pollution such as adopting cleaner technologies to remediate industrial smokestack emissions and appropriate planning of urban transportation system. Numerous cities in Europe have achieved success by giving priority to public transportation systems,

building extensive bicycle paths, and creating low emission zones by restricting entry to vehicles that do not meet the emission standards[41–43]. Additionally, stringent regulations are being imposed on vehicle manufacturers to improve upon the catalytic converter technologies used in vehicular exhausts. Advanced research is also being pursued on using cleaner forms of energy for transportation by means of electric and solar driven vehicles or a combination of both in the form of hybrid vehicles. Even with all the countermeasures in place, the uncontrollable nature of the direction of wind patterns result in non-localized sources of air pollution. In such cases, the only way to remediate air pollution is through use of technologies such as photocatalysis. Photocatalysis can be applied to convert the harmful gaseous pollutants by chemically breaking them down to harmless compounds by using the energy of light or photons. Now a brief review on photocatalysis and its application in pollution remediation is provided in the subsequent section.

1.2 *Photocatalysis*

Catalysis under the irradiance of electromagnetic spectrum of light or photons is termed as photocatalysis. It is based on the phenomenon of photons activating the catalyst, which leads to formation of free radicals that convert the chemical molecules, which are physically adsorbed onto the photocatalyst. Over the past four decades, photocatalysis has received widespread attention from the scientific community throughout the world. Researchers are focusing their attention on utilizing photocatalysis as a means to find solutions for alternative energy and pollution remediation[44–46]. Heterogeneous photocatalysis using semiconductor materials constitutes a similar process to that of a conventional heterogeneous catalytic system. Due to the largely insoluble nature of the catalysts during application, a heterogeneous catalytic system adheres to the five discrete processes associated with it:

1. Transfer of liquid or gaseous phase reactants to the catalytic surface
2. Adsorption of at least one reactant
3. Reaction in the adsorbed phase

4. Desorption of product(s)

5. Removal of products from the interface region

A photocatalytic reaction occurs in the adsorbed phase i.e., in the third process, in the presence of light or photons and in close proximity to the catalytic surface[45]. In the case of homogenous photocatalysis, the transport phenomenon of molecules by adsorption and desorption is an intrinsic process as the catalyst and reactants are in the same phase. In semiconductor photocatalysis, conventional thermal activation of the catalyst is usually replaced by photonic activation. Semiconductor photocatalysis comprises a large variety of reactions and processes, e.g. photocatalytic oxidation (PCO), photocatalytic reduction, dehydrogenation, hydrogen transfer, O_2^{18}-O_2^{16} and deuterium-alkane isotopic exchange, metal deposition, water detoxification, gas-phase pollutants removal, and a host of other environmental applications[44]. PCO is most noteworthy within the family of semiconductor photocatalysis reactions and usually involves irradiation from a light source of appropriate wavelength depending on the band gap energy of the semiconductor. This activation generates highly reactive hydroxyl and other oxygenated radicals that facilitate oxidative degradation of organic, inorganic, and metallic pollutants to render end-products such as water, CO_2 and mineral acids.

There are different materials which fall into the category of semiconductor photocatalysts such as, metal oxides i.e., TiO_2, ZnO, MoO_3, CeO_2, ZrO_2, WO_3, $SrTiO_3$, Fe_2O_3 etc.; and non-oxides i.e., GaAs, CdS, InP, ZnS, CdSe WS_2, MoS_2 etc. Semiconductors have been employed in a wide spectrum of photocatalytic applications[45,46]. Among these materials, titanium dioxide (TiO_2) has received the most attention because of its high photocatalytic activity, resistance to photocorrosion, photostability, low cost, and non-toxicity[47,48]. Over four decades back, in 1972, Akira Fujishima and Kenichi Honda discovered a ground-breaking phenomenon of photolysis of water splitting into hydrogen and oxygen using platinum cathode and UV irradiated TiO_2 photoanode[49]. This led to a widespread usage of TiO_2

in multiple fields of research and commercial applications, which include beneficial effects of using TiO_2 in construction materials, energy sector and pollution remediation techniques[50–52]. Some of the applications are depicted in Figure 1.5, which involves the usage of ultraviolet (UV) spectrum of light for the activation of photocatalyst.

Titanium dioxide, titanium(IV) oxide or simply titania, occurs mostly in three mineral forms in nature, namely rutile, anatase and brookite (Figure 1.6), among which rutile is the most common and stable form[53]. Antase and brookite both convert to rutile phase when heated to temperatures in the range of 600 - 800 ^{0}C. Some of the properties of different crystal forms of titanium dioxide are listed in table 1.3. There are different types of commercial crystalline TiO_2 photocatalysts available in the market i.e., P25, PC500, P90 etc., which differ in the crystallite size, surface area and band gap. Majority of these commercial photocatalysts consists of the anatase phase of TiO_2, which is a better photocatalyst than rutile. However, there is no clear consensus on the reason behind the better performance of the anatase TiO_2. Some studies have attributed the better transport of excitons from the bulk to the surface and the diffusive nature of reactive oxygen species in anatase TiO_2 compared to the confined reaction zone in rutile phase[54–56].

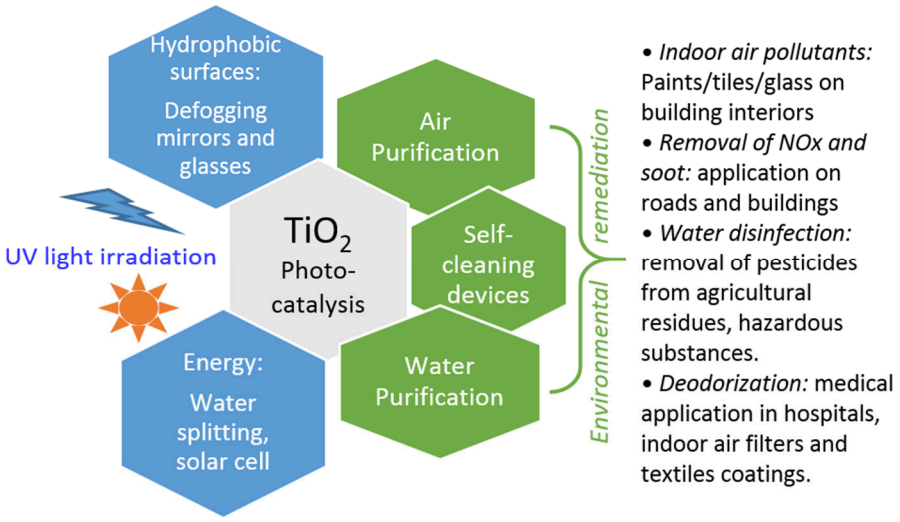

Figure 1.5. Multiple applications of TiO_2 photocatalysis

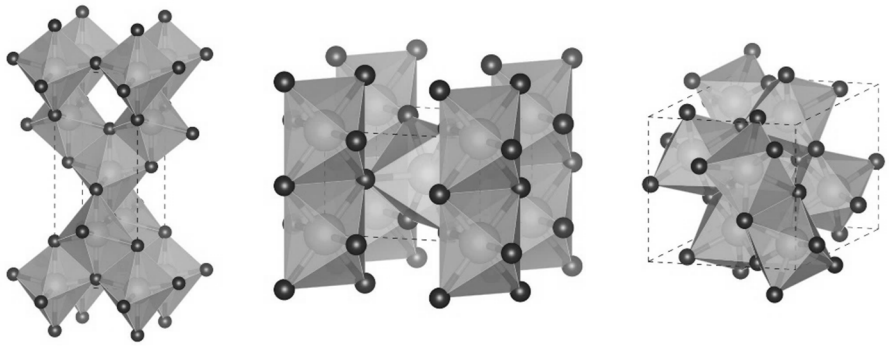

a) Anatase b) Rutile c) Brookite

Figure 1.6. Crystal structures of a) anatase, b) rutile and c) brookite forms of TiO_2 drawn using the crystallographic software program VERSA ver. 3.4.4.

Crystal Structure	System	Band gap (eV)	Electron mobility, μ (cm^2/V.sec)	Density (Kg/m^3)
Rutile	Tetragonal	3.0	1	4240
Anatase	Tetragonal	3.2	10	3830
Brookite	Rhombohedral	-	-	4170

Table 1.3. Crystal properties of anatase, rutile and brookite forms of TiO_2[53].

TiO_2 has been touted as one of the main photocatalyst that could be used to remediate the environmental pollutants, but the commercialization of photocatalyst-based nanotechnology for environmental cleanup has been slow. This is because of some drawbacks associated with the usage of TiO_2. One of the drawbacks is the band gap of the TiO_2 photocatalyst, which is in the range of 3-3.2 eV[53] that requires energy from the UV spectrum of the light. Therefore, any remediation technology employing TiO_2 requires additional UV light irradiation source, as the radiation from sunlight that reaches the surface of the earth consists of less than 5% UV[57]. Another drawback associated with the usage of TiO_2 is the recombination effect of the excitons i.e., electron (e^-) and hole (h^+) regime within the TiO_2 domain before the excited charges reach the surface of the particle to initiate the redox reactions[58]. These drawbacks could be overcome by the different strategies such as doping of metals and non-metals, inducing defects to acts as charge trapping centers and utilizing the localized

surface plasmon resonance (LSPR) properties of noble-metal nanoparticles to create visible light active photocatalysts[48,59]. The most promising strategy that has made a significant impact in increasing the efficiency of TiO_2 photocatalysis is the coupling of noble metal nanoparticles with TiO_2[60–64]. Therefore, the consecutive section will provide an overview of the plasmonic enhancement of photocatalysis. The term localized surface plasmon resonance will be shortened to surface plasmon resonance (SPR) for ease of use at some instances, henceforth in this thesis as the discussion is mostly restricted to the confined effects of LSPR in small noble metal nanoparticles.

1.3 *Plasmonic photocatalysis*

The enhancement of photocatalysis by coupling the plasmonic properties of noble metal nanoparticles with a semiconductor photocatalyst such as TiO_2 is termed as plasmonic or plasmon-enhanced photocatalysis. In the past decade, there has been a tremendous increase in the research on plasmonic photocatalysis for environmental remediation and photovoltaic devices for alternative energy technologies[63–66]. The SPR property of noble metal nanoparticles is a unique phenomenon, which is an oscillation of electron cloud generated in the close vicinity of nanoparticle, when in resonance with the incident electromagnetic radiation (Figure 1.7). The resonance is possible when the wavelength of incident light matches the SPR wavelength of the nanoparticle, which changes with the size and shape of the nanoparticle.

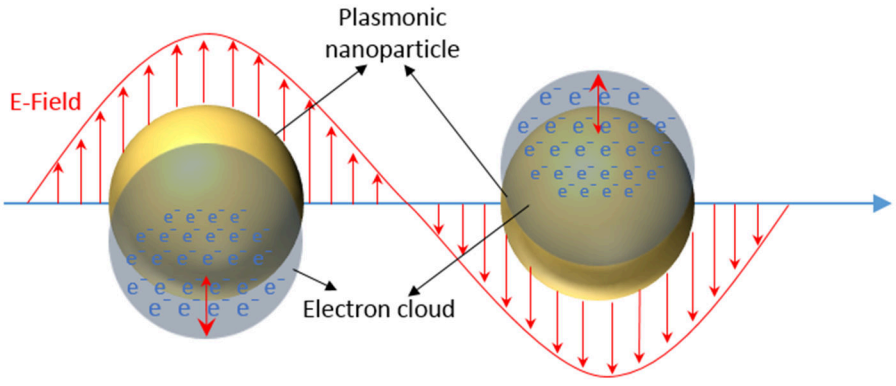

Figure 1.7. Schematic representation of plasmon resonance for a spherical nanoparticle, showing the oscillation of electron cloud in resonance with incident electric field. Adapted from ref.[67] ©American Chemical Society.

Silver, gold and platina are examples of such noble metals that possess the exclusive SPR property because of the wavelength dependent dielectric data. This phenomenon generates intense electric fields that are localized within a few nanometers in the close vicinity of plasmonic nanoparticle surface. The localized surface plasmon resonance is a direct result of interaction between the noble metal nanoparticle and the oscillating electric field of incident electromagnetic radiation. Consequently, the conduction band electrons oscillate causing a displacement relative to the nuclei. This generates restoring coulombic forces of attraction between the electrons and the nuclei, which further causes the electrons to oscillate in the opposite direction. This harmonic oscillation specific in the direction of polarization is called as dipole plasmon resonance. Higher forms of resonance such as quadruple resonance is displayed by plasmonic nanoparticles (diameter > 50 nm) when the electron cloud oscillates in more than one direction of applied field[67,68]. The dipolar plasmon resonance phenomenon is shown as a schematic representation in Figure 1.7. The optical physics involved in the plasmonic materials and the underlying Mie theory for studying the interaction of light and plasmonic nanoparticles using the Maxwell's electromagnetic wave equations are described in more detail in chapter 3.

The SPR properties of the plasmonic materials such as Ag/Au is highly beneficial when the noble metal nanoparticles are incorporated into a semiconductor photocatalyst such as TiO_2 leading to a promising technology of plasmonic photocatalysis. The most important feature of plasmonic coupling with TiO_2 is that it induces visible light activity, which would utilize the visible light spectrum of the solar radiation[69]. Ag and Au nanoparticles in the size range of tens of nanometers have good UV and visible light harvesting properties, which has driven research to successfully utilize the broadband UV-visible light spectrum resulting in drastic improvement of TiO_2 photocatalysis. The feasibility to tune the excitation wavelength of the plasmonic photocatalyst by taking advantage of the size-dependent optical properties of plasmonic nanoparticles has given rise to a new dimension of research in achieving maximum possible enhancement[70,71]. This is possible by targeting the

overlap of the wavelengths of surface plasmon resonance with the semiconductor band-gap energy and light illumination source[72]. In this way, the electron-hole (e^-- h^+) pair excitons of semiconductor and oscillating electron cloud of plasmons are excited at the same time, which result in a plethora of possibilities boosting the photocatalytic efficiency[73,74]. The favorable effects responsible for plasmonic enhancement of photocatalysis are shown in Figure 1.8.

In order to understand the beneficial effect of the plasmonic photocatalysis, a schematic comparison is shown between the common TiO_2 photocatalysis (Figure 1.9a) and gold plasmon-enhanced photocatalysis (Figure 1.9b). A typical TiO_2 system has oxygen defects leading to excess electrons, which makes it an n-type semiconductor. The recombination effect, a major drawback of TiO_2 photocatalysis, occurs when the e^-- h^+ pairs recombine within the bulk and/or at the surface of the particle (Figure 1.9a). So the generated charges are available for redox reactions for extremely short time durations, in the range of couple of hundred femtoseconds. Whereas, the e^-- h^+ pairs recombine within 1-10 picoseconds at the surface[58]. This has serious implications for achieving better quantum yields for TiO_2 photocatalysis[75]. When a plasmonic nanoparticle such as gold is coupled with TiO_2, photons from the visible light are absorbed by gold, independent of the UV light absorption by TiO_2 (process 'A' in Figure 1.9b). This creates an oscillating electron cloud because of the LSPR phenomenon, which excites more electrons and holes. The Schottky contact formed at the metal-semiconductor junction keeps the e^-- h^+ pair separated, reducing the recombination rate in the space charge region[64,73,74]. The LSPR induced internal electric field (E) at the interface drives the excited electrons from the gold surface through the space charge region and are injected into the conduction band of TiO_2 (process 'B' in Figure 1.9b)[76,77]. The synergetic nature of all these effects play a favorable role in the improvement of quantum efficiency of plasmonic photocatalyst. The important parameter influencing the efficiency of photocatalytic reactions are the energy band positions of materials, which provides a perspective of optimal light absorption wavelength and feasibility aspects of redox reactions.

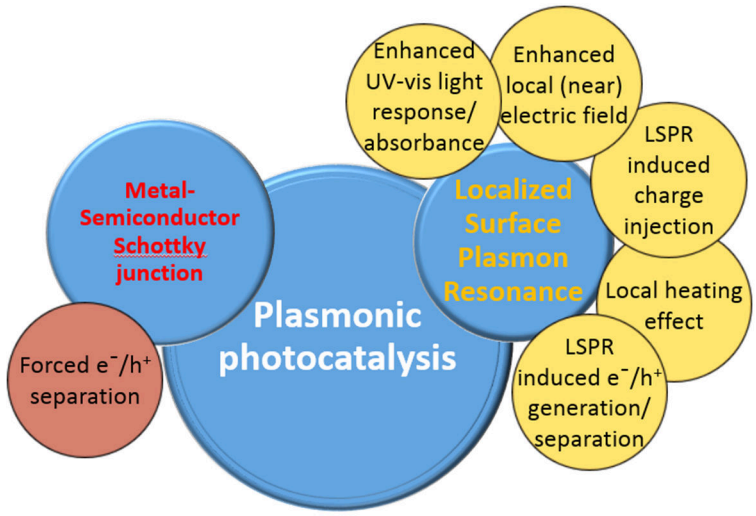

Figure 1.8. Major mechanisms leading to plasmon enhancement of photocatalysis. Adapted from ref.[73,74].

For a typical TiO_2 photocatalytic system, the energy of the incident light source has to be greater than the band gap energy for the generation of electron and hole ($E_{inc} = h\nu \geq E_{CB} - E_{VB}$) as shown in Figure 1.10a. The excited electron and hole have energies E_{CB} and E_{vB} respectively, which are transferred to intermediate energy levels E'_{CB} and E'_{vB}. The redox reactions proceed with donation of electron at E'_{CB} and extraction of electron by hole at E'_{vB} provided the energy requirements i.e., $E'_{CB} \geq E_{red}$ and $E'_{vB} \geq E_{ox}$ are met[74]. In Figure 1.10a, the energies are expressed in potential levels of electrons with the energy reference at vacuum level taken as zero.

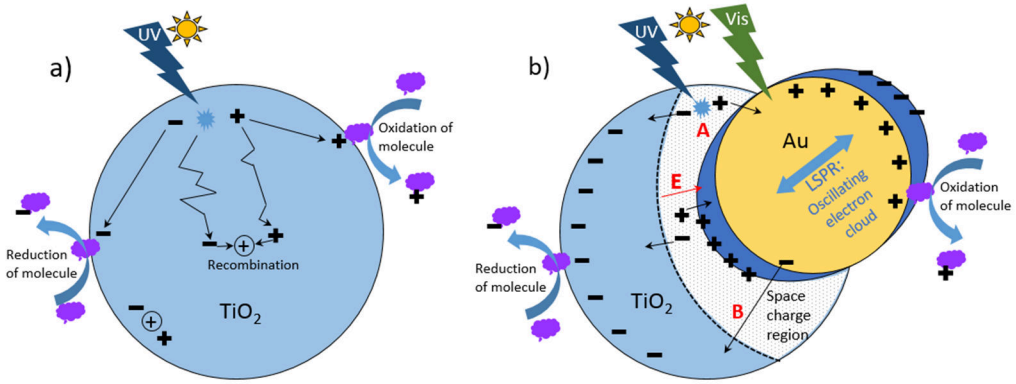

Figure 1.9. Processes in **a)** common TiO_2 photocatalysis and **b)** Au-plasmon photocatalysis. Adapted from ref.[74] ©IOP Publishing.

In the case of plasmonic photocatalyst, LSPR phenomenon of metal nanoparticle leads to electron transfer through many pathways, which will be discussed now. The band positions of commonly used photocatalysts and work functions of noble metals are shown in Figure 1.10b. In plasmonic photocatalysis, the energy dissipation from the plasmonic metal to the semiconductor is possible through multiple pathways[67,68,74,78,79], which could be condensed into two i.e., either radiative or non-radiative decay. Radiative decay of the plasmon resonance and the resulting energy transfer is significant for large nanoparticles (diameter > 50 nm). This is possible because of the enhanced optical path length of the photons due to the scattering phenomenon of nanoparticles larger than 50 nm in diameter[80].

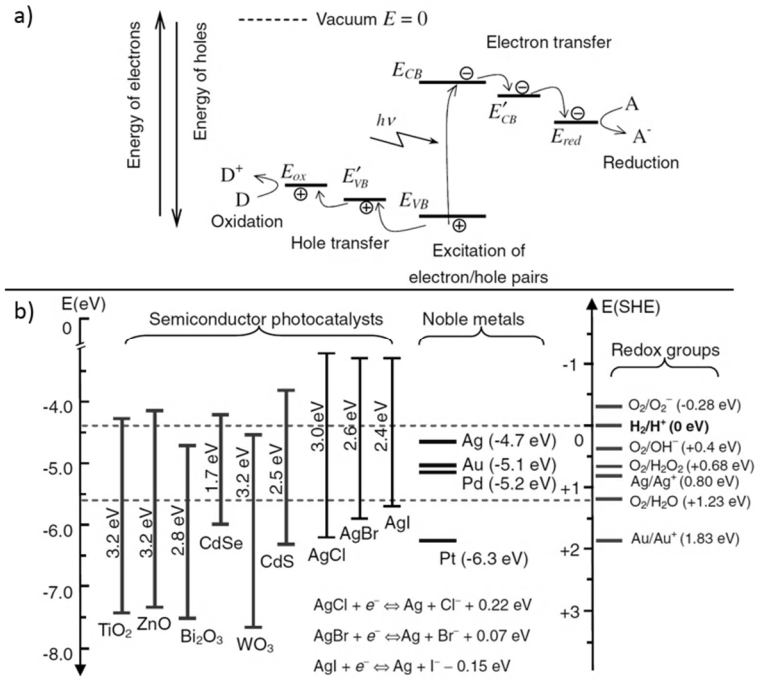

Figure 1.10. a) Typical electron-hole energy transfer processes in photocatalysis and **b)** Energy band positions and work functions of some commonly used materials in plasmonic photocatalysis, and the electrochemical potentials of redox reactions with standard hydrogen electrode (SHE) as reference. Reprinted from ref.[74] ©IOP Publishing.

The non-radiative decay results in energy transfer through multiple electron-phonon interactions[79]. In this thesis, it is not the intention to study the quantum mechanics involved in these atomic level interactions. So only, the generic nature of these electron-phonon interaction's effects on the noble metal-semiconductor interfacial charge transfer will be outlined. This framework is heavily dependent on the crucial insights provided by the exceptional review articles of Linic et al.[64], Clavero[65] and Zhang et al.[74]. The electron transfer due to non-radiative decay of LSPR could be represented in Figure 1.11. When visible light is incident on the plasmonic photocatalytic system, it activates the LSPR induced electron cloud, and the electrons have higher energy than the semiconductor conduction band. This leads to direct injection of a hot electron (shown as DET in Figure 1.11) from the plasmon metal to semiconductor, which is similar to photosensitization effect[77,81,82]. The LSPR induces intense near-electric field in the space-charge region driving the formation of more charge carriers (shown as NEFCG in Figure 1.11) in the close vicinity of the metal-semiconductor interface, and more importantly at the surface of photocatalyst. This leads to enhanced charge carrier generation at the surface of material, instead of in the bulk, reducing the probability of recombination centers[62,81].

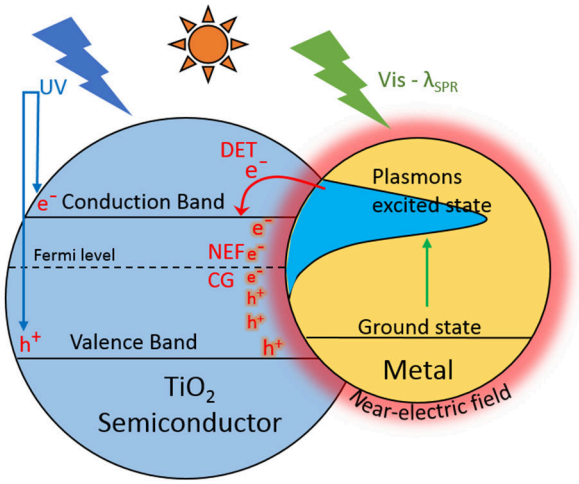

Figure 1.11. Schematic representation of mechanisms for the direct electron transfer (DET) and near-electric field induced charge carrier generation (NEFCG) at the surface/interface of plasmonic photocatalyst.

The intensity of the near-electric field is quite high at the metal-semiconductor interface, which is also dependent on the refractive index of the surrounding medium. The field intensity is distance dependent with an exponential relationship and is more intense towards the semiconductor side, which facilitates more charge carrier generation leading to better utilization of e^-- h^+ pairs at the semiconductor surface[64]. It is important to note that; excitation of plasmonic metal requires the overlap of incident light wavelength with the LSPR wavelength of the metal[72,83]. This is independent of the excitation of electron-hole pair generated in TiO_2 that could be an exclusive or mutually synergetic effect of charge carrier generation in a plasmonic photocatalyst depending on the incident light energy. The local heating effect is also an important mechanism[84,85], but is beyond the scope of this thesis due to technical factors of such an experimental setup. Overall, the clear nature of plasmonic enhancement of photocatalysis is still under debate, as the complex nature of plasmonic photocatalysis requires in depth understanding of interdisciplinary topics of atomic physics, surface science and photochemistry. Additionally, the plasmonic enhancement of photocatalysis depends on the multiple parameters such as design, synthesis and surrounding medium of the system. This thesis limited the discussion of processes inside and at the surface of plasmonic nanoparticle and the TiO_2 photocatalyst and avoided the discussion of reaction pathways such as interaction of excitons and redox groups. In the next section, a mechanistic approach is provided to study the different mechanisms.

1.4 *Motivation and outline of the thesis*

The main goal of this thesis is to identify the main mechanisms responsible for plasmon-mediated TiO_2 photocatalysis. As discussed in the prior section, there is still a lot of debate going on regarding the definitive mechanism responsible for plasmon-enhanced photocatalysis. However, the two important mechanism that play a crucial role are:

- *Direct electron transfer*
- *Near-electric field*

The dominant mechanism responsible for enhancement is also dependent on design of the plasmon-semiconductor interface. To achieve the objective of elucidating the mechanism, different architectures of plasmonic photocatalytic systems are possible based on the contact form between the metal and semiconductor. Examples of such designs include metal nanoparticle embedded inside TiO_2 matrix; metal nanoparticles deposited on the surface of TiO_2 particles or film; and partial embedment of metal inside the TiO_2 films that was used in the well-known work of Awazu et al.[62] using the Ag-TiO_2 plasmonic photocatalytic system. In the work of Awazu et al., the spacing between the metal and semiconductor was controlled using a SiO_2 interfacial layer. In the work of Kumar et al., the field effects were analyzed by depositing films of silver and TiO_2, which were separated by fine tuning the ALD deposited SiO_2 layer thickness[86]. In this work, a simple yet direct interface or contact between the plasmonic nanoparticle (Ag/Au) and semiconductor photocatalyst (TiO_2) was maintained as shown in Figure 1.12. The tuning of spacing or distance between the plasmonic nanoparticle and TiO_2 was achieved by building a polyelectrolyte layer with tunable thickness, that could be either conductive or insulating. Increasing the thickness of the encapsulating shell, the spacer layer would also become thick, thereby altering the magnitude of LSPR induced near-electric field that is available at the surface of TiO_2. An insulating layer would inhibit the direct electron transfer process and at the same time, the distance dependency of the near-electric field for achieving the plasmonic enhancement of photocatalysis could be investigated.

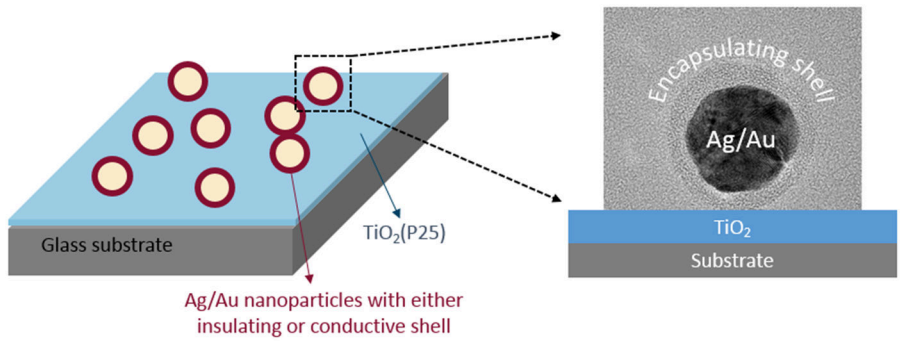

Figure 1.12. Proposed architecture of Ag/Au plasmon enhanced TiO_2 photocatalytic system used in this thesis to study the effects of the near-electric field and direct electron transfer.

Building on the information of effective thickness which rules out the near-electric field mechanism, a system with a thick conductive shell around the plasmonic nanoparticle which would act as a conductive spacer layer and would show the significance of the direct electron transfer process. Comparison of photocatalytic activities of all these systems would provide a clear picture on the major mechanism responsible in plasmon-enhanced photocatalysis. It is also important to note that a plasmonic photocatalytic systems designed with an architecture shown in Figure 1.12 would also avoid the formation of schottky contact at the metal-semiconductor interface. Moreover, the activity measurements with a direct contact between noble metal and semiconductor photocatalyst would shed light on the mechanistic impact of schottky contact in plasmonic photocatalysis.

With the proposed approach, the next step would be the synthesis of thickness tunable shell i.e., the spacer layer. The polyelectrolyte layer cannot not be built directly in-situ at the interface of plasmonic nanoparticle and TiO_2, because it is difficult to achieve such arrangement using wet chemical methods. Therefore, the spacer layer was built as a shell around the plasmonic nanoparticle, which creates a system consisting of plasmonic core@shell nanoparticle in contact with TiO_2 (Figure 1.12). It is also important to have a good degree of control to fine tune the thickness of the shell at nanoscale level. Layer-by-Layer (LbL) method is one such method that provides a high level of control over the thickness of polyelectrolyte layer.

LbL method is a versatile wet-chemical synthesis technique, which was introduced by Prof. Gero Decher in 1997[87]. It is based on the principle of sequential adsorption of alternatively charged (positive/negative) polyelectrolytes onto substrates to form thin films as shown in Figure 1.13. Electrostatic attraction between oppositely charged molecules is the driving force for adsorption and multilayer build-up at nanoscale level. The simple wet chemistry involved in LbL method led to widespread application in different fields that would require assembly of thin films and coatings such as catalysis, optics, energy, biosciences and membrane technology[88]. The synthesis of thin films is possible using dip coating, spin coating or spray coating

methods. The parameters which effect the film thickness are: concentration of polyelectrolytes, time of deposition, speed of coating method and the pH of the polyelectrolyte. The film synthesis is based on the surface charges on the polyelectrolyte chains, so significantly fast build-up which is termed as exponential LbL (e-LBL), could be achieved by maintaining partial charge on the chains by controlling the pH of the polyelectrolyte solution[89,90].

The implementation of LbL methodology on colloidal templates involves similar adsorption principle, but the resulting material has a core-shell morphology as shown in Figure 1.14. The encapsulation of colloidal templates using LbL method has widespread application in biological sciences for drug delivery and sensing applications[91–94]. In the colloidal LbL methodology, achieving complete coverage of the three-dimensional surface of the colloidal nanoparticle requires an excess of polymer chains during the deposition process. The crucial parameters that effect the efficiency of the formation of core-shell morphology are the polymer chain length i.e., molecular weight and the concentration of polymer solutions. The molecular weight of the polymer has a significant influence on the morphology of the nanostructures prepared using LbL method. High molecular weight polymers (50,000 – 70,000 g/mole) will have very long polymer chain molecules and would result in formation of nanoclusters with encapsulation of multiple nanoparticles within the polyelectrolyte layer. So, medium or low molecular weight polymers, in the range of 2,000-20,000 g/mole, would be optimal for single nanoparticle encapsulation[95]. The ionization of the polymer chain is also crucial, as some of the polyelectrolytes have weak surface charges along the chain if the solutions are not prepared at either high or low pH values. Whereas strong polyelectrolyte solutions tend to be have a fully ionized polymer chain at all pH values[96]. Some of the polyelectrolytes are listed in Table 1.4, which are extensively used in this thesis for synthesis of core-shell nanoparticles. During the LbL synthesis, removal of excess polyelectrolytes and washing with high purity water (resistivity > 10 MΩ) is done by centrifuging the mixture of colloidal nanoparticles and polyelectrolyte solutions.

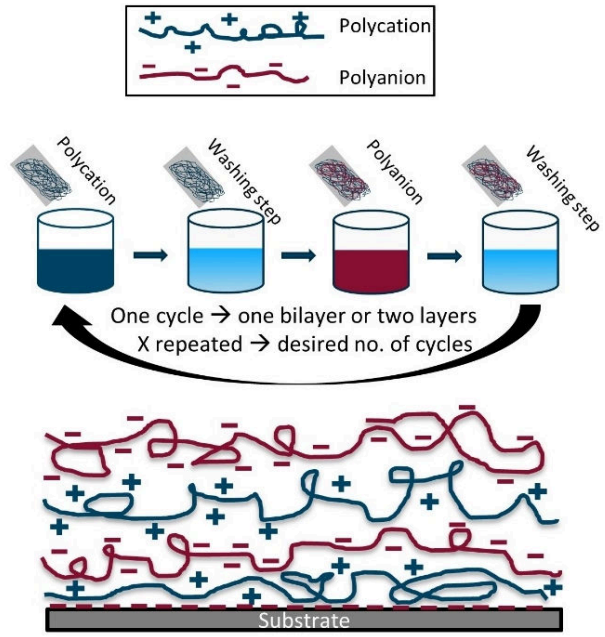

Figure 1.13. Layer-by-Layer (LbL) synthesis of thin films using dip coating method.

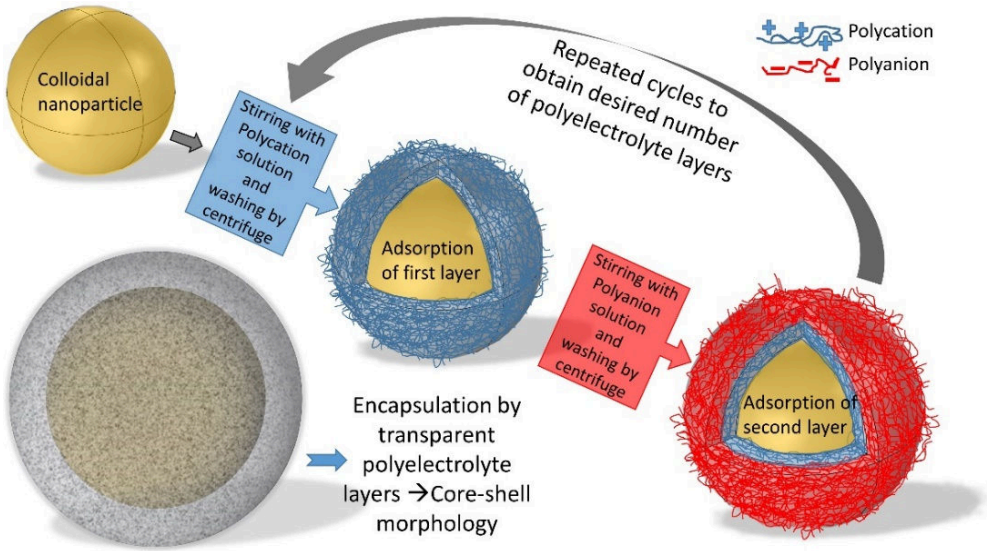

Figure 1.14. Layer-by-Layer (LbL) synthesis on colloidal templates resulting in core-shell nanoparticles.

Polycations: Positively charged polyelectrolytes	Polyanions: Negatively charged polyelectrolytes
Poly(allylamine hydrochloride) PAH – weak fully ionized at pH<5.0 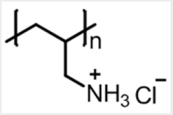	Poly(sodium styrene sulfonate) PSS - Strong 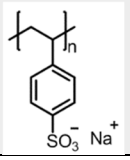
Polyethylenimine PEI – Weak, fully ionized at pH<3.0 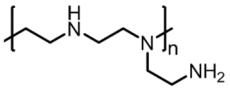	Poly(acrylic acid) PAA –Weak, fully ionized at pH>9.0 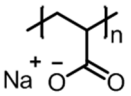

Table 1.4 List of polyelectrolyte used in this work for LbL colloidal synthesis

The centrifuge speed is an important parameter that should be taken care of to avoid irreversible formation of hard pellets of nanoparticles. The duration of the centrifuge step is the only drawback associated with the synthesis protocol of colloidal LbL method, as sometimes it could involve long centrifuge times. However, researchers have found a workaround by developing a faster way of LbL assembly of polyelectrolyte layers on colloidal templates using the principles of flow chemistry[97,98].

An insulating polyelectrolyte layer could be built around the plasmonic metal nanoparticle by the colloidal LbL method. However, the same principle could not be applied to build a conductive shell, since the low molecular weight conductive polyelectrolyte raw materials needed for LbL colloidal synthesis are not readily available. However, after some significant amount of research and experimental trials with a different strategy of coupling a conductive polymer, which was available, with a non-conductive polymer did not induce conductivity in the polyelectrolyte layer. In addition, the LbL synthesis was not successful with no hints of encapsulation of plasmonic metal nanoparticle as observed from spectrophotometric measurements. Therefore, an alternative synthesis method was used to build a conductive polymer i.e., polyaniline (PANI), around the nanoparticle. This was based on the in-situ polymerization of aniline around the nanoparticle under acidic pH conditions[99]. It is also important to have a good control over the acidity of the final product, since the conductive properties of polyaniline are dependent on the doping levels of hydrogen

ions[100,101]. The advantage of using PANI is that the conductive nature of the end product could be identified by the color of the solution[102], which is not apparent with other conductive materials such as polypyrrole. The protonated emeraldine salt form is green colored and is the most conducting form, whereas the blue color of the emeraldine base is the non-conducting form. With the prosed idea of polyelectrolyte layer acting as a spacer layer between the TiO_2 and plasmonic metal (Figure 1.12), chapter 2 is the application of this approach for Ag-TiO_2 system followed by theoretical studies in chapter 3. In chapter 4, the near-electric field is quantified using SERS as an experimental evidence of the distance dependence decay of near-electric field and corroborated with theoretical estimations. In the fifth chapter, the mechanistic approach is applied to Au-TiO_2 systems to elucidate the major mechanisms of plasmonic photocatalysis, followed by the overall conclusions and outlook in the final chapter.

Chapter 2

Plasmon enhanced TiO_2 photocatalysis using ultrastable silver nanoparticles

Based on:

***Ramesh Asapu**, Nathalie Claes, Sara Bals, Siegfried Denys, Christophe Detavernier, Silvia Lenaerts, Sammy Verbruggen, Silver-polymer core-shell nanoparticles for ultrastable plasmon enhanced photocatalysis. "Reprinted (adapted) with permission from **Applied Catalysis B: Environmental** 200 (2017) 31-38. © 2016 Elsevier B.V."*

Contributions: Nathalie Claes, EMAT, University of Antwerp, for TEM and EDX elemental analysis.

Matthias Minjauw and Tareq Ahmad, CoCooN, Gent University, for C-AFM measurements.

Sreeprasanth Pulinthanathu Sree, COK, KU Leuven, for SEM images.

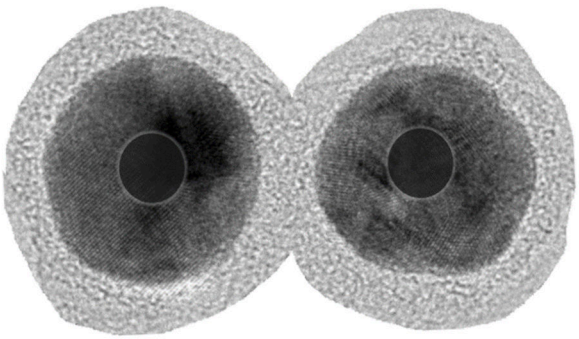

"When you look into the nanoparticles, the nanoparticles look back at you"

2.1 *Introduction*

The application of plasmonic nanoparticles has found its way in different areas of research such as solar cells[103], plasmonic photocatalysis[62–64,70,104,105], surface-enhanced Raman scattering (SERS)[106] and biophotonics[107]. Among the noble metals that exhibit surface plasmon resonance (SPR), gold and silver are most commonly investigated as they display SPR over a wide wavelength range and their SPR properties can easily be tuned through their size, shape and (alloy) composition[70,108]. The synthesis of stable (functionalized) plasmonic nanoparticles is of high importance as they carry unique surface properties with applications in various research domains, e.g. encapsulation of plasmonic nanoparticles is of particular interest to biomedical science with applications in drug delivery[109] and imaging[110]. Overall, gold nanoparticles are more stable and easy to functionalize, explaining the major literature focus on this type of metal. Functionalization of gold nanoparticles using thiols and ligands capping the nanoparticles[111], as well as encapsulation using polyelectrolytes has been documented well[95,112,113]. In contrast, functionalization of silver nanoparticles is less obvious, as it is challenging with respect to stability, aggregation and size control. Also, silver nanoparticles are prone to oxidation when left over prolonged periods, which hinders functionalizing the surface. A solution to these challenges is the preparation of stable silver nanoparticles with a core-shell structure consisting of a silver core surrounded by a thin protective shell that prevents oxidation of the silver nanoparticle. In the context of silver encapsulation, the use of organic linkers (e.g. thiol-derivatives, xanthate, etc.)[114–116] has been reported as well as various (mostly one-pot) synthesis strategies for capping with inorganic shells (e.g. silica, inorganic carbon)[117–120]. The main drawback in all of these aforementioned methods is that they do not present complete freedom to accurately control the shell thickness, though this is one of the most crucial parameters in many plasmonic applications such as SERS[110], where slight changes in shell thickness can alter the near-field enhancement to a large extent. The Layer-by-Layer (LbL) method is a simple yet powerful technique to apply ultra-thin shells on colloidal templates[87,113]. Fabrication

of silver core-shell nanoparticles using the LbL method has only been reported on silver nanocubes by prior functionalization of the surface using surfactants and washing with buffers during the layer deposition process [121]. In this work, the LbL method is directly applied to as-prepared spherical silver nanoparticles without the use of any additional surfactants or supporting layers, this way avoiding supplementary washing steps with buffers. Preparing silver-core polymer-shell nanoparticles in such fashion is a facile and versatile strategy with the freedom to control the shell thickness at the nanoscale, typically even less than one nanometer. Furthermore, synthesis with the less expensive negatively charged polyelectrolyte, polyacrylic acid (PAA) was also successful, in contrast to the more expensive poly(styrene sulfonate) (PSS) which is traditionally used for nanoscale colloidal systems, in combination with the positively charged polyelectrolyte poly(allylamine hydrochloride) (PAH). The main objectives of this work are to study (i) the effect of the polymer shell on the plasmonic field enhancement properties and (ii) the stability of the resulting capped silver nanoparticles when deposited on TiO_2 for photocatalytic environmental remediation. More in particular the plasmon-enhanced photocatalytic degradation of acetaldehyde, a common hazardous indoor air pollutant, is studied. In such systems the silver core-shell nanoparticles serve a dual purpose: (i) the polymer shell protects the silver nanoparticle from oxidation and clustering and (ii) the SPR properties of silver create intense local electric fields that enhance the charge carrier generation and thus improve the photocatalytic acetaldehyde degradation reaction.

2.2 *Experimental methods*

2.2.1 Synthesis of Silver-polymer core-shell nanoparticles

Stock solutions of polyelectrolytes polyallylamine hydrochloride (PAH, MW 17.5 kDa Sigma-Aldrich), polyacrylic acid (PAA, MW 2 KDa Sigma-Aldrich) and poly(styrene sulfonate) sodium salt (PSS, MW 15 KDa Polymer Standard Services GmbH) were prepared in Milli-Q water by sonication for 30 min and used as required. 12 mL of the as prepared silver colloidal solution (procedure reported elsewhere[122])

was centrifuged at 8000 rpm for 100 min and redispersed in Milli-Q water. This was done to remove most of the citrate in the colloidal silver solution, in order to reduce the interference of charge on the citrate molecule and to have optimal deposition of the first polycation layer (PAH). 12 mL of this centrifuged silver colloidal solution was added dropwise to 6 mL of 5 g/L PAH solution under vigorous stirring in a glass vial. The stirring was continued at room temperature for 20 minutes in dark. The resulting colloidal solution was centrifuged in 1.5 mL Eppendorf tubes to remove the excess polyelectrolyte. Around 1460-1480 µl of supernatant was discarded and the remaining dark-brownish gel-like pellet was redispersed in Milli-Q water. The centrifuge process was repeated one more time as a washing step and the final redispersion in Milli-Q water was adapted to obtain 12 mL of colloid. A small aliquot of this PAH coated silver colloid sample was stored for characterization purposes and the deposition of the second layer i.e. polyanion PAA (10 g/l) was continued using the same procedure as described above. The centrifuge speed was slightly adapted after each deposition step to avoid formation of hard pellets that cannot be redispersed. The centrifuge speeds are listed in Table 2.1.

Polyelectrolyte	Centrifuge step	Speed (rpm)	Duration
PAH	1st	12000-13000	40 minutes
PAH	2nd	11000-12000	40-60 minutes
PAA/PSS	1st	10000	60 minutes
PAA/PSS	2nd	7000-8000	60-90 minutes

Table 2.1. Centrifuge speeds and time duration for different stages of LbL synthesis.

2.2.2 Characterization

Spectroscopy measurements were performed with a Shimazdu 2501 spectrophotometer in a UV-cuvette of 10 mm path length to locate the SPR peak. Scans were performed in the spectral range of 300-800 nm with a resolution of 0.2 nm and an average of three measurements was taken. Zeta potential measurements were

done using Brookhaven's ZetaPlus zeta potential analyzer to monitor the surface charge on the core-shell nanoparticles. A FEI Tecnai Transmission Electron Microscope (TEM) operated at 200 kV was used to visualize the core-shell structure of nanoparticles. In a typical procedure 20 µL of the colloidal solution was absorbed during 5 min on a quantifoil copper grid coated with a 3.19 nm carbon film. For HAADF-STEM measurements, spin coated material (as described in section 2.2.3) was scraped off the glass substrate and dispersed in ethanol before sampling. Current-Voltage (IV) measurements were performed using a potentiostat (Versastat 3, Princeton Applied Research, AMETEK Sci. Inst.). Photometric measurements were performed to determine the silver mass concentration per unit volume in the colloids by appropriate dilution to detection limits using a standard Spectroquant® silver test kit. For the nanoscopic measurements using conductive atomic force microscopy (C-AFM), dilute colloidal solution of silver-polymer core-shell nanoparticles were dropcasted on a substrate pre-coated with gold, in order to attain monolayer coverage. Substrates were attached to a stainless steel sample plate using conductive carbon tape. The sample was loaded in an Omicron VT XA ultra-high vacuum (UHV) AFM, which operates at a base pressure of 10-10 mbar. Durable B-doped full diamond tips (FDT) were used for optimum electrical contact, reproducibility and suitable tip resistance.

2.2.3 Photocatalytic activity tests

The Ag-TiO_2 plasmonic photocatalytic system was prepared with a 5 wt.% suspension of commercial TiO_2 (P25, Evonik) nanoparticles in ethanol and stirred ultrasonically. 100 µL of the suspension was spin coated at 1500 rpm for 60 seconds onto several piranha cleaned glass slides of size 1.5 cm x 2.5 cm. The substrates were dried overnight at 100°C followed by spin coating with 75 µL of the colloidal solution of bare silver or silver-polymer core-shell nanoparticles at 1500 rpm and finally air dried at 80 °C for 6 hours. Two identical slides were used to perform one photocatalytic test. As such, three different samples were prepared i.e., a pristine P25 reference film; a P25 film coated with bare silver nanoparticles, denoted P25_Ag; and a P25 film coated with four layered core-shell silver nanoparticles, denoted P25_Ag_L4. The

photocatalytic activity of above prepared films is measured online by monitoring the gas phase degradation of acetaldehyde under UVA irradiation in a glass slit reactor using FTIR detection. Measurements were repeated over a period of 16 weeks in order to study the stabilizing effect offered by the protective shell. The reactor design, set-up and operation is explained in detail in previous work of our research group [123,124].

2.3 *Results and discussions*

2.3.1 LbL synthesis of silver-polymer core-shell nanoparticles

Silver nanoparticles with diameter around 18 nm were synthesized by reduction of silver nitrate with tannic acid and trisodium citrate as described elsewhere[122]. A schematic representation of the silver colloidal synthesis procedure is shown in Figure 2.1. Silver-polymer core shell nanoparticles were prepared by the LbL method, i.e. sequential cycles of adsorption and washing of alternatively charged polyelectrolytes as shown in Figure 2.2. However, the pre-centrifuge step as described in the experimental section is a crucial step as a significant amount of stabilizing citrate ions would interfere with the positively charged polyelectrolyte. After the pre-centrifuge step at 8000 rpm for 100 min, and redispersion in equal amount of water that was aspirated out, there is no change in the plasmon peak position as seen from Figure 2.3a. Additionally, if the pre-centrifuge step is not performed before the beginning of the LbL method, there would be a blue shift in the plasmon peak position as shown in Figure 2.3b. This may be because the charge of negative citrate ions, which are present in stock colloidal solution, would interact with positively charged polyelectrolyte chains.

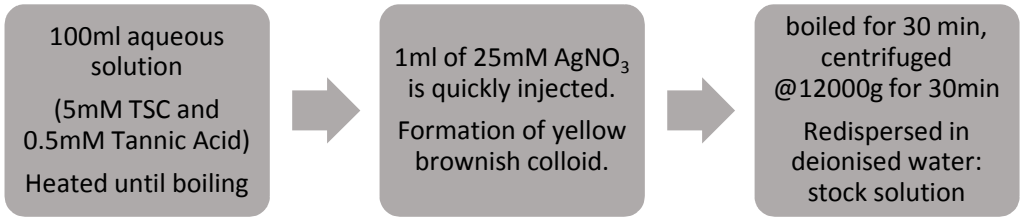

Figure 2.1. Synthesis of silver nanoparticle colloidal solution[122].

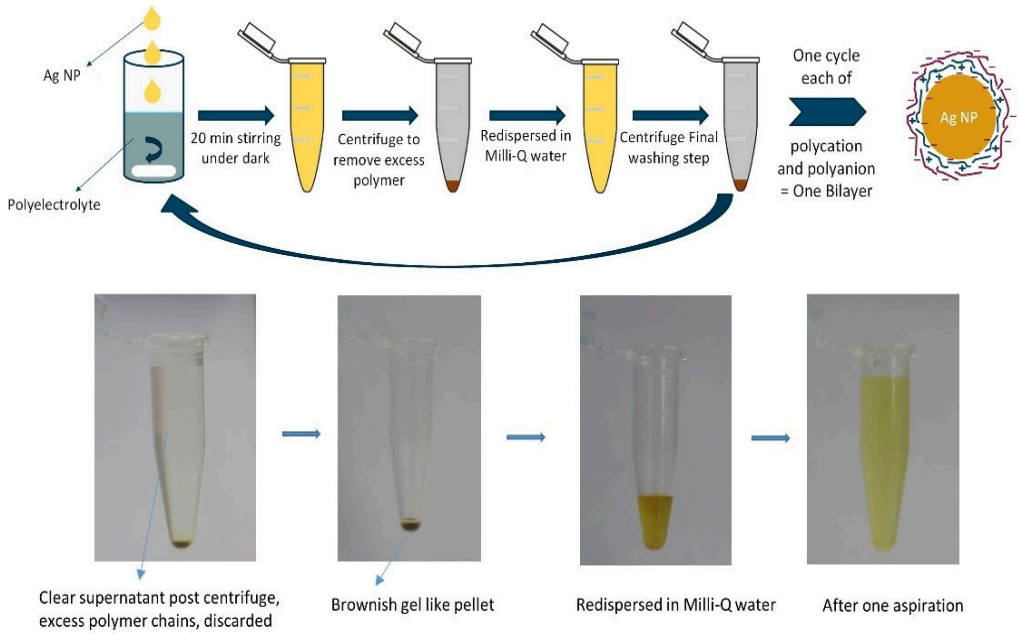

Figure 2.2. LbL synthesis of silver-polymer core-shell nanoparticle colloid.

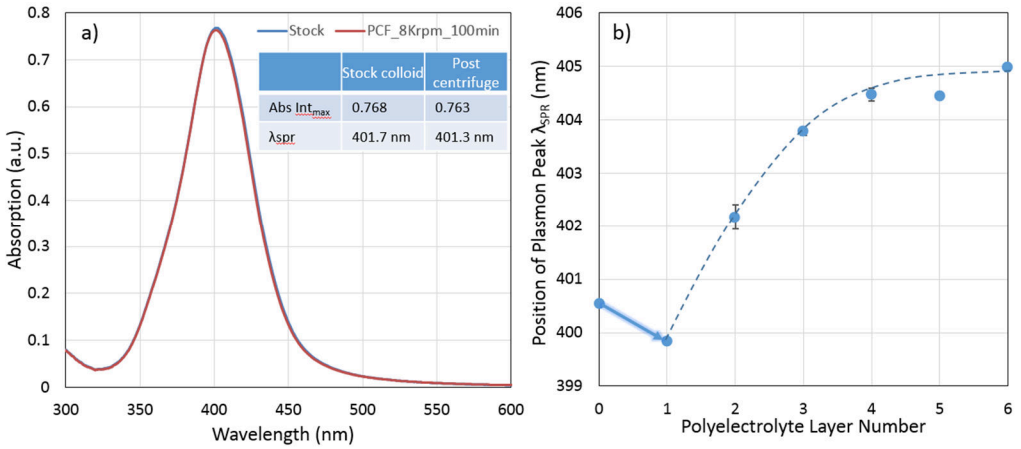

Figure 2.3. a) Pre-centrifuge step before LbL method and b) effect of plasmon peak position during the LbL process for a batch without the pre-centrifuge step.

The alternate deposition of polycation and polyanion chains was continued until the desired number of layers was obtained that result in the encapsulation of the silver core by a thin polymer shell. Zeta potential measurements after each adsorption cycle show the inversion of surface charge on the core-shell nanoparticles with the deposition of alternatingly charged polyelectrolytes, evidencing the success of the LbL strategy (Figure 2.4a). The UV-vis absorption spectrum of the core-shell nanoparticles

was also recorded after each deposition step (Figure 2.4b). By measuring the absorption intensity, it could be determined that on average 85-90% of silver nanoparticles was retained after each deposition cycle, which is in line or above the optimized LbL procedure on gold nanoparticles[95]. A clear red shift of the SPR peak with increasing number of adsorbed layers can also be observed in Figure 2.5a, which indicates the gradual increase in particle size as more LbL layers are added. Traditionally, the strong – yet expensive – polyelectrolyte PSS is used as the polyanion in the LbL synthesis. At the beginning of this study, the possibility of replacing PSS by the weaker but cheaper low-molecular weight PAA polyanion was also investigated. For comparison purposes, two sets of silver-polyelectrolyte systems were prepared, i.e. with PAH/PAA and PAH/PSS.

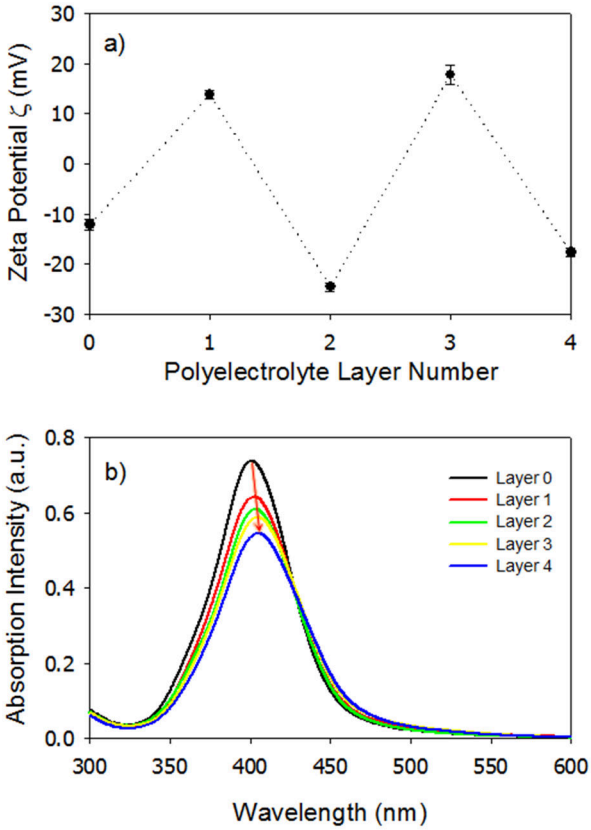

Figure 2.4. a) Zeta potential of core-shell silver nanoparticles Ag/(PAH/PAA)$_2$ as a function of adsorbed polyelectrolyte layer. b) UV-vis absorption spectra of core-shell silver nanoparticles as a function of adsorbed polyelectrolyte layer. The red arrow indicates the red shift in SPR peak position.

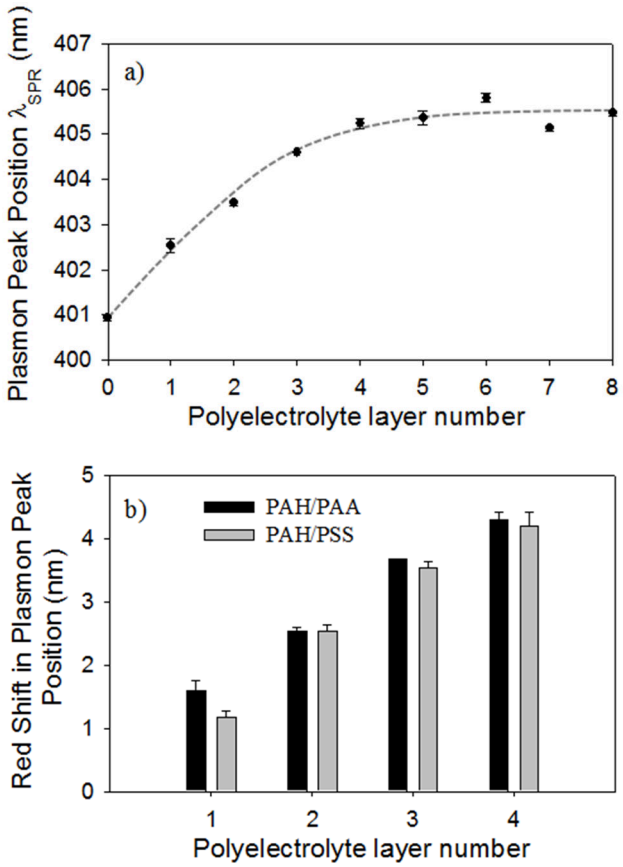

Figure 2.5 a). Plasmon peak position of the silver core-shell nanoparticles as a function of number of adsorbed PAH/PAA polyelectrolyte layers. b) Comparison of red shift in SPR peak position in different polyelectrolyte systems PAH/PAA and PAH/PSS.

As seen from Figure 2.5b, the SPR peak red shift for silver nanoparticles using the polyelectrolyte system of PAH/PSS shows similar behavior when compared to the PAH/PAA polyelectrolyte system. In addition, the corresponding shell thicknesses are similar (Figure 2.6), confirming the feasibility of using PAA as the polyanion for the LbL synthesis as a cost-effective alternative to PSS. From the UV-vis spectrophotometric measurements, it may be inferred that the red shift of the SPR peak after the first four layers is comparatively less significant, though an increase in shell thickness is confirmed by the TEM images in Figure 2.6. As seen from these images (Figure 2.6a and 2.6b), the four- and eight-layered core-shell nanoparticles, denoted as Ag_L4 and Ag_L8, are encapsulated by a thin shell of thickness (1.4 ± 0.4) nm and (2.4 ± 0.7) nm respectively, as derived from 100 shell thickness measurements in TEM. This

demonstrates the continuous growth of the shell with increasing number of polyelectrolyte layers. During TEM analysis, the particles were also tilted over a series of different angles. The shell can be clearly observed from every projection, which is an evidence that the silver particles are completely and homogeneously covered by the polyelectrolytes (Figure 2.6d). As an additional evidence to prove that more layers were being deposited around the nanoparticle even in the absence of a red shift in plasmon peak position, a new batch of core-shell nanoparticles were synthesized encapsulated with 12 layers of polyelectrolytes. The red shift in plasmon peak position for this batch is shown in Figure 2.7. As discussed before, it seems that there is no significant red shift in plasmon peak position beyond eight layers, but the TEM images (Figure 2.8) clearly show an increase in shell thickness from L4→L6→L8→L12. From the TEM measurements, a linear relationship could be estimated between the layer number and shell thickness for the silver-polymer core-shell nanoparticles (Figure 2.9).

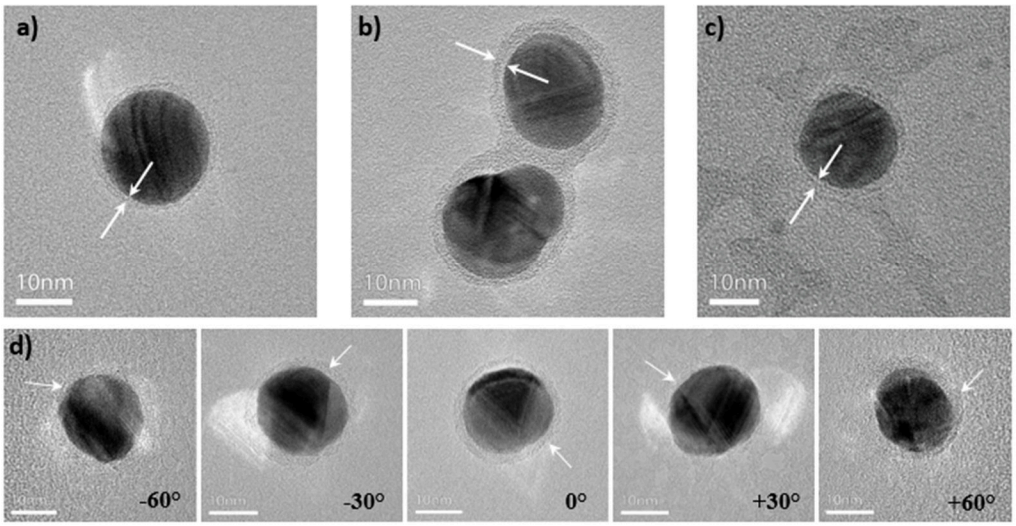

Figure 2.6. Silver core-shell nanoparticles with silver core and an ultrathin shell composed of a) four polyelectrolyte layers (Ag_L4) Ag/$(PAH/PAA)_2$ of thickness 1.4 ± 0.4 nm, b) eight polyelectrolyte layers (Ag_L8) Ag/$(PAH/PAA)_4$ of thickness 2.4 ± 0.6 nm, c) four polyelectrolyte layers (Ag_L4) Ag/$(PAH/PSS)_2$ of thickness 1.6 ± 0.4 nm, d) TEM tilt series of Ag_L8 core-shell nanoparticles. All the inset bars represent a scale of 10 nm. The shell thickness distribution is based on 100 measurements.

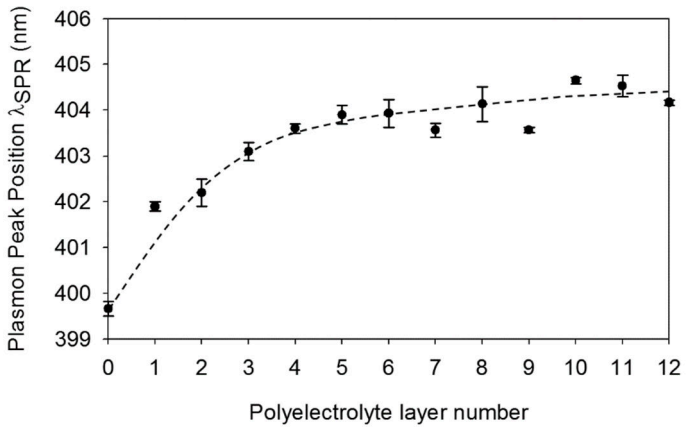

Figure 2.7. Plasmon peak position of silver core-shell nanoparticles (Ag_L12) as a function of number of adsorbed polyelectrolyte layers. $Ag(PAH/PAA)_6$ i.e., 6 bilayers.

Although the shell thickness differs slightly in the order of ± 0.2 nm between the different batches, care was taken to use the samples from appropriate batch for a particular set of application. The repeatability studies and average measurements of shell thickness is studied in more detail in the next chapter where theoretical calculations are performed and the average measurements are more appropriate.

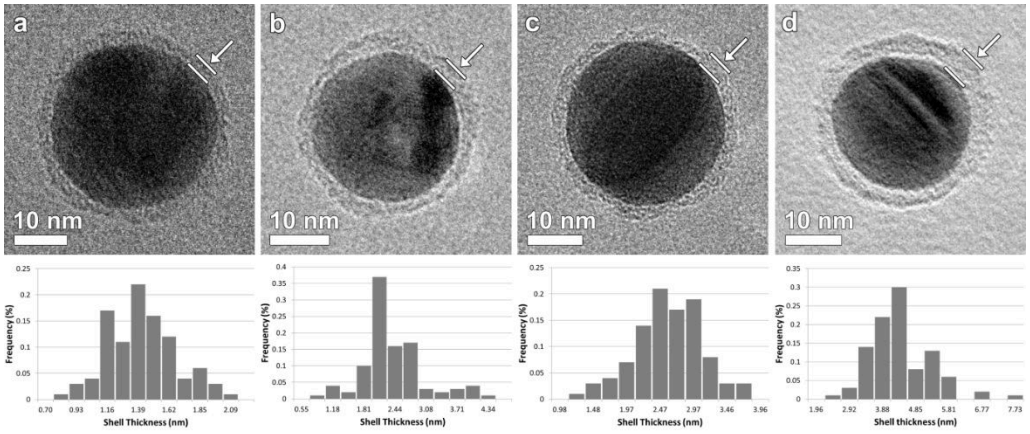

Figure 2.8. TEM images of silver core-shell nanoparticles: from left to right Ag_L4, Ag_L6 Ag_L8, and Ag_L12. The shell size distributions are shown at the bottom. Reproduced from Ref.[125] with permission from ©The Royal Society of Chemistry.

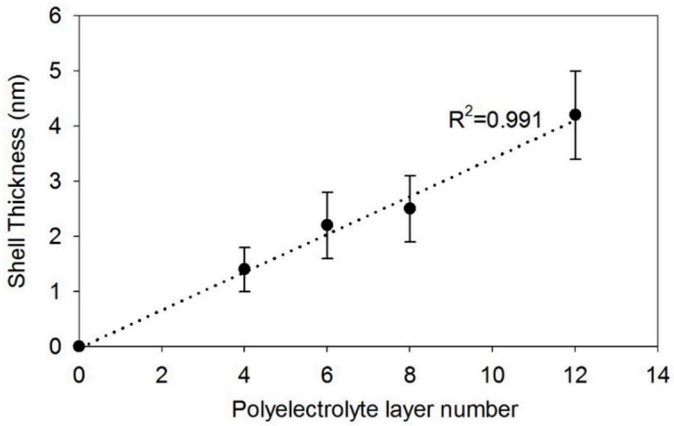

Figure 2.9. Relationship between the shell thicknesses of silver core-shell nanoparticles as a function of number of adsorbed polyelectrolyte layers.

2.3.2 Ultra-stability of silver-polymer core-shell nanoparticles

As previously mentioned, the intention is to use these plasmonic nanoparticles in a gas phase photocatalytic system in an oxidative atmosphere (acetaldehyde in air). It is therefore crucial to *a priori* evaluate the stability of the prepared nanoparticles in order for this approach to succeed. Also, other plasmon-based application such as SERS and most of bio-sensing applications heavily depend on the stability of the system in stressful conditions. The latter application, for instance, requires colloidal stability in the presence of salt buffers. Hence, as a first test, the stability of the as-prepared silver and silver-polymer core-shell colloidal nanoparticles was studied upon addition of sodium chloride salt. So 150 µL of 1 M NaCl solution was added to 1.5 mL lots of colloidal solution of stock Ag and polymer encapsulated Ag_L4 nanoparticles. An immediate color change was observed for bare Ag nanoparticles, whereas the core-shell nanoparticles retained their bright yellow color displaying the stability and resistance of the polymer shell to the permeation of chloride ions as seen from Figure 2.10a. For the bare silver colloidal solution, dark precipitates were observed at the bottom of the test vial after the solutions were aspirated and allowed to stand overnight. A second stability test consisted of subjecting the colloidal nanoparticles to a harsh hot-air treatment. Keeping in mind the photocatalytic application of acetaldehyde degradation, this test will already reveal the potential of the

nanoparticles to resists harsh oxidative conditions. For this test colloidal solutions of unprotected Ag and protected Ag_L4 nanoparticles were concentrated by centrifugation and drop casted on cleaned quartz substrates. Initially both the concentrated unprotected Ag and Ag_L4 nanoparticles have a similar orange-like color as seen from figure 2.10b. After the heat treatment at 105 °C overnight in the presence of air, a drastic color change from to greyish black is observed for unprotected silver nanoparticles, which is characteristic of silver oxide. On the other hand, the silver-polymer core-shell nanoparticles Ag_L4 retain the orange color displaying their ultrastable nature. This proves that the polymer shell is acting as a protective barrier for silver nanoparticles against oxidation and will help retaining the plasmonic properties.

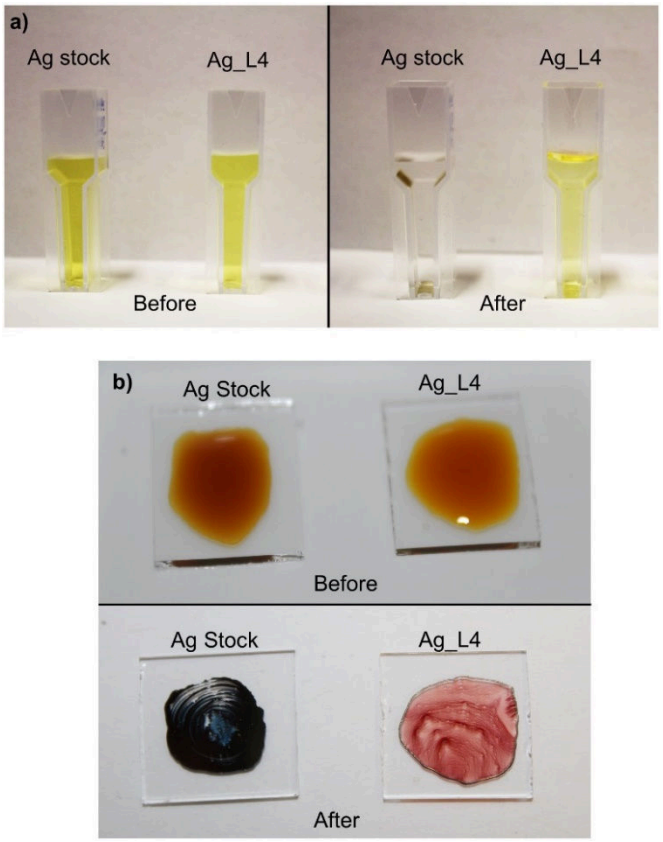

Figure 2.10. a) Photographic images showing the effect of salt addition on unprotected Ag *versus* protected Ag_L4 colloidal nanoparticles and b) Photographic images showing the effect of hot air treatment on unprotected Ag *versus* protected Ag_L4 nanoparticles.

2.3.3 Long term photocatalytic activity tests

As mentioned before, the main goal of developing the silver core - thin polymer shell nanoparticles was to protect the silver nanoparticles against oxidation and clustering when applied on a photocatalytic substrate to be used in an oxygen-rich environment. Silver-modified TiO_2 substrates were prepared by spin coating 75 µL of the colloidal nanoparticle suspensions onto glass substrates pre-coated with TiO_2 P25 (details in section 2.2.3). The presence of Ag on the TiO_2 surface was confirmed by HAADF-STEM (EDAX) analysis as shown in Figure 2.11. In EDAX measurements, a peak at energy 2.983 keV is expected in the presence of Ag (Ag Lα = 2.983 keV). At different

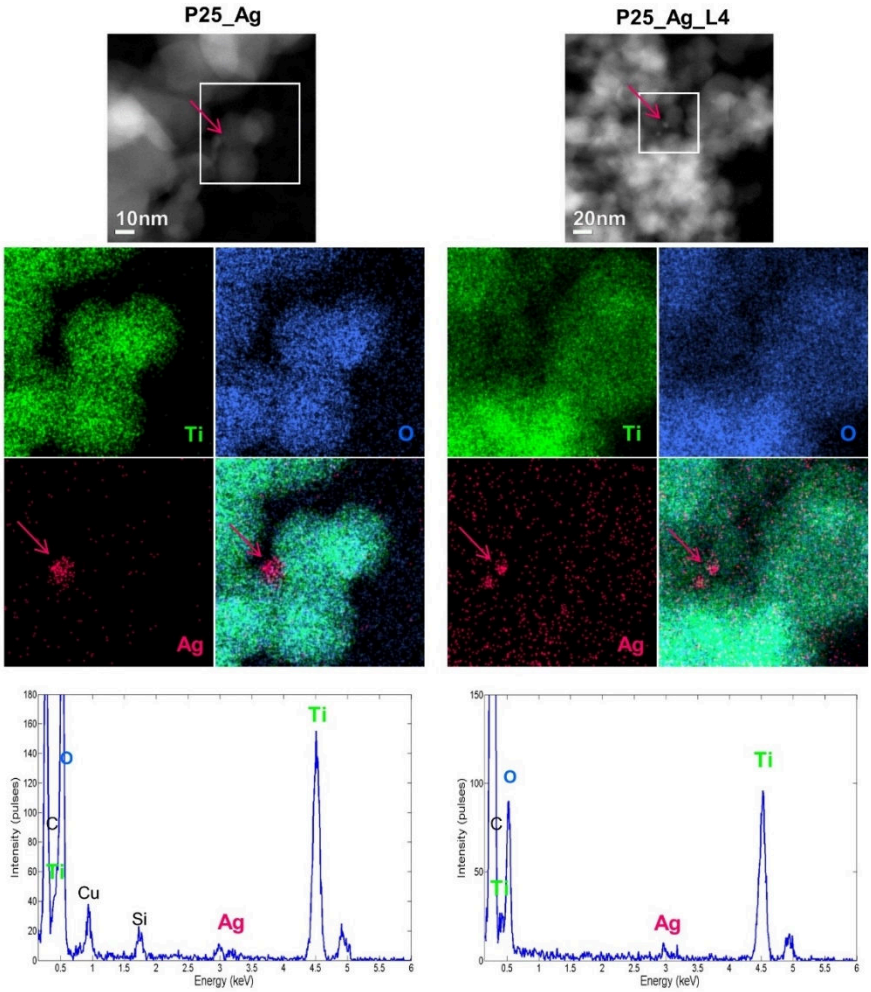

Figure 2.11. High angular annular dark field – STEM (HAADF-STEM) images (top) and EDX spectra (bottom) of P25_Ag (left) and P25_Ag_L4 (right) samples. The elemental maps show the presence of the Ag nanoparticles on the surface of TiO_2.

positions in the sample, a peak for Ag could be observed in the EDX spectrum but unfortunately, the amount of Ag deposited was too low for accurate and reliable quantification. The spin coated P25 films have a uniform distribution of the photocatalyst on the glass substrate surface as seen from the scanning electron micrograph (SEM) images in Figure 2.12. In addition, repeated reference measurements performed with the pristine TiO_2 samples revealed a relatively small deviation in the photocatalytic activity. To verify the success of the strategy of silver plasmon-enhanced semiconductor photocatalysis, a long-term time study was conducted on the photocatalytic activity of the Ag-TiO_2 plasmonic systems toward the degradation of acetaldehyde in air (Figure 2.13). This demanding environmental application was deliberately selected to subject the samples to a stringent oxidative atmosphere in order to verify the effect of the absence and presence of a protective LbL shell, also in the long term. Therefore, a comparison was made between pristine TiO_2 (P25, Evonik), TiO_2 modified with bare Ag nanoparticles and TiO_2 modified with core-shell Ag_L4 nanoparticles. Ag_L4 core-shell nanoparticles were selected as they present the best overlap of the plasmon band and the peak wavelength of the irradiation source used in the photocatalytic experiment (365 nm). This topic is discussed in more detail in the next chapter which deals exclusively with the theoretical modeling of plasmonic nanoparticles.

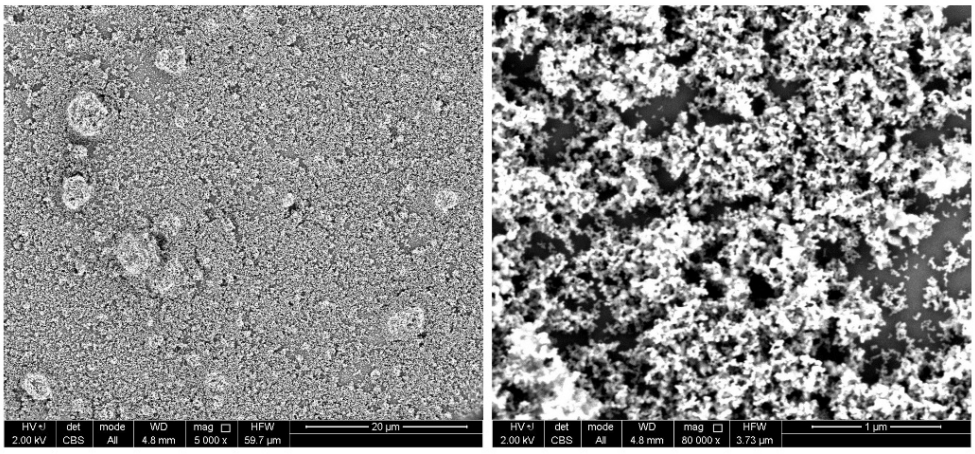

Figure 2.12. SEM images of the Degussa P25 spin coated on glass substrates. On the left is a low resolution and on the right is a high-resolution image at 1 µm scale.

The pristine TiO_2 films retained their activity well over the entire experimental period of 16 weeks, as expected. For TiO_2 films loaded with bare silver nanoparticles (P25_Ag), initially at time t = 0 (i.e. freshly prepared), a considerable activity enhancement was observed, which can be ascribed to plasmonic enhancement induced by the metallic Ag nanoparticles present on the surface. After three weeks, however, a significant drop in the activity enhancement was observed and no enhancement at all remained after 16 weeks. This effect is attributed to progressive oxidation of the bare Ag nanoparticles, with resulting loss of their plasmonic properties. It has in fact been observed that upon ageing of such systems, a thin diffuse silver oxide (Ag_2O) shell of approximately 2 nm is formed at the surface[126,127]. To confirm the detrimental effect of oxidation on the near-field enhancement of the silver nanoparticles, modeling studies are performed in the next chapter. In contrast, the system involving Ag nanoparticles protected by a thin polymer shell on TiO_2 (P25_Ag_L4) retained its activity enhancement (15% increase) even after 16 weeks of ageing in air. It should be noted that this plasmonic catalyst has not been optimized towards parameters such as particle size and silver loading. A given set of experimental conditions was arbitrarily chosen and kept fixed for accurate comparative analysis. Therefore, the observed increase of 15% is probably not maximally attainable and not the goal of this study.

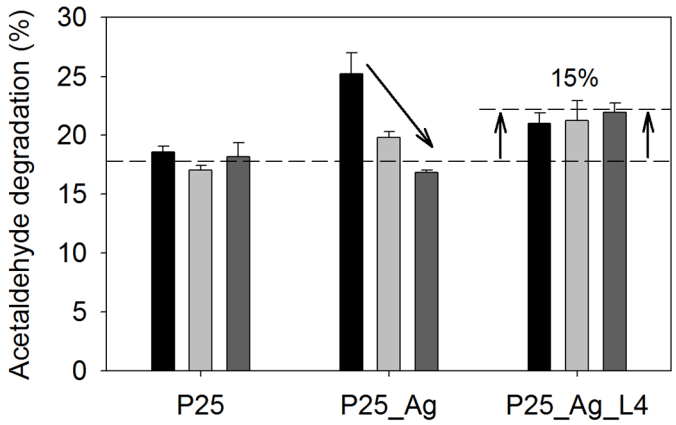

Figure 2.13. Long-term photocatalytic activity test. The photocatalytic degradation of gaseous acetaldehyde is evaluated at t=0 (i.e. freshly prepared, black), after three weeks (light grey) and after 16 weeks (dark grey) of ageing in air. The dotted line indicates the average acetaldehyde degradation by reference system P25.

Still, the data clearly prove that the thin polymer shell stabilizes the Ag nanoparticles without compromising the plasmonic properties, making them particularly suited for such demanding applications, even in the long-term.

2.3.4 Mechanism elucidation of silver-TiO_2 plasmonic photocatalytic systems

As outlined in the introduction chapter that the main goal of this thesis is to identify the main mechanism responsible for plasmon enhanced photocatalysis. There are many possibilities through which electrons could play either a positive or a negative role when a semiconductor material like TiO_2 is in direct contact with metal. The direct contact between the plasmonic metal and semiconductor photocatalyst was avoided by building a polyelectrolyte spacer layer as discussed so far. In addition, it is essential to know about the electronic/electrical properties of the polyelectrolyte interface material. This was done by performing the conductivity measurements on the polyelectrolyte layer. The nanoscale electrical properties for polyelectrolyte bilayers are greatly affected by various parameters such as thickness and ambient conditions[128]. So it becomes crucial that the conductivity measurements are not performed on individual polyelectrolyte bilayers, but rather for the end product material, which is the silver-polymer core-shell nanoparticles.

Cyclic Voltammetry studies were used to estimate the conductivity behavior of the as prepared core shell nanoparticles. In the initial step, gold coated inter digitated electrode (IDE) chips which were lithographically pre-patterned with micrometer gaps were acquired. A small section of the patterned gold was etched to widen the micrometer gap for multiple IDE chips, represented by the discontinuity of gold pattern lines as shown in the optical microscopic and photographic images in Figure 2.14. These gaps were then bridged carefully by dropcasting a concentrated microliter drop of stock silver colloidal nanoparticles and silver@polymer core@shell nanoparticles as shown in Figure 2.14a and Figure 2.14b respectively. The samples were allowed to dry in the desiccator for couple of days. The optical microscopic images from the Figure 2.14 clearly indicate the difference in color between the bare and polymer protected

silver nanoparticles demonstrating the protective nature of polyelectrolyte layers. The ends of the IDE chips were clamped to the electrodes of the potentiostat to perform the IV cyclic voltammetry. The placement of the samples in the IDE pattern bridge avoids the direct contact between the potentiostat electrode and the material that is being tested, so that the contact resistance does not become one of the influencing variables of the experiment. The cyclic voltammetry data (Figure 2.15) indicates that the IDE chip bridged with Ag_L4 is relatively non-conducting in nature compared to Ag because the slope of the IV curves is directly related to conductivity of the sample.

Additional conductivity measurements were performed using a conductive tip atomic force microscope (C-AFM) to get further confirmation regarding the electrically insulating nature of the polyelectrolyte layer. The reason for using C-AFM to determine the electrical properties of the core-shell nanoparticles is that the polymer blends have unique electrical properties depending on the type of polymers used. Merely measuring the current-voltage (IV) properties of the as-prepared silver-polymer core-shell nanocluster film can lead to false interpretations when using a typical four-point probe method to determine the resistivity.

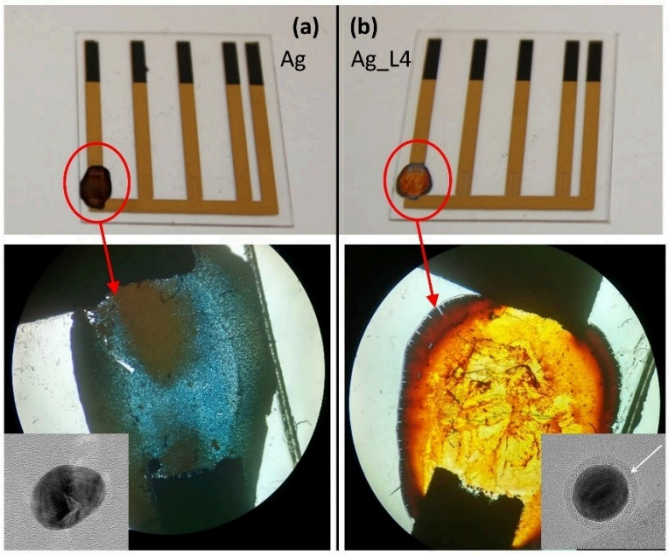

Figure 2.14. Photographic and corresponding optical microscopic images of the etched IDE chips bridged by **(a)** stock silver colloid nanoparticles AgL0 and **(b)** polectrolyte encapsulated silver nanoaprticles Ag_L4. TEM images of silver and silver@polymer core@shell nanoaprticle are for shown in inset for representative purpose only.

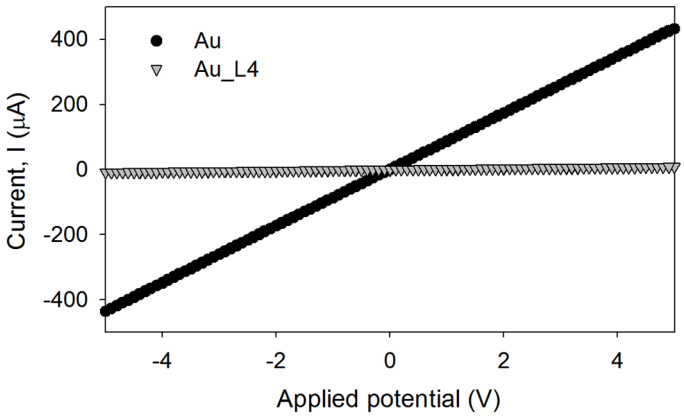

Figure 2.15. IV cyclic voltammetry of Ag nanoparticles measured using a potentiostat.

This is because in a dried nanocluster film the polymer shells of adjacent nanoparticles are in contact and the resulting resistance is in fact that of a long nanoparticle chain. So, a more robust methodology is adapted by immersing a gold coated Si wafer in a dilute colloidal solution of silver-polymer core-shell nanoparticles to make sure single isolated core-shell nanoparticles could be imaged by AFM. The nanoparticle located by AFM surface mapping, was investigated by applying a voltage through the conductive cantilever tip of the AFM; and the detected current levels indicate the resistance of the core-shell nanoparticle on the gold substrate. From Figure 2.16, it could be observed that a core-shell nanoparticle with a shell thickness of 1.4 nm is highly insulating and resists charge transfer. Both the particles in the AFM surface image showed no passage of current with the increase in voltage until the AFM

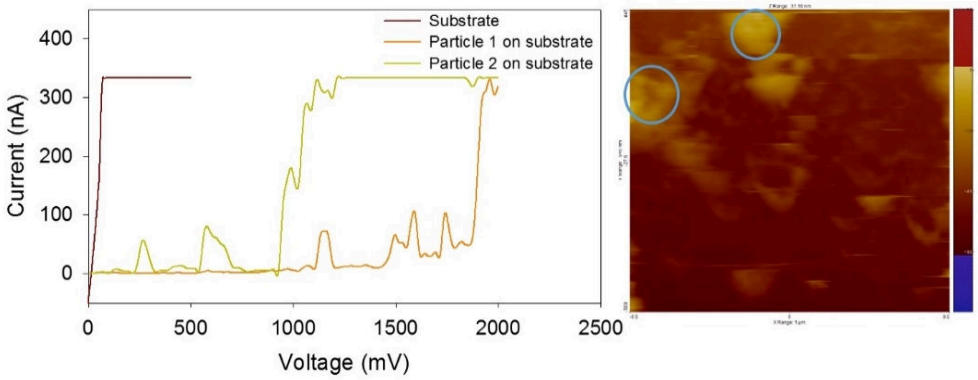

Figure 2.16. Conductive tip AFM measurements performed on gold substrate and on two core-shell nanoparticles (Ag_L4) deposited on substrate, the AFM surface image on the right shows the location of two particles.

cantilever tip tunneled through the particle and made contact with the gold substrate underneath. This is a classic tunneling IV profile for high resistance or insulating materials. It has been established through multiple experimental evidence that the encapsulating polyelectrolyte shell are insulating in nature. Therefore, it could be assumed that when the silver@polymer nanoparticles are in contact with the TiO_2 and when UV light is incident on this system, the polymer layer does not allow electrons or charges to flow through towards or outwards from the core silver nanoparticle. In an Ag-TiO_2 plasmonic photocatalytic system with such an arrangement, the polyelectrolyte layer becomes an insulating spacer layer which prevents the charge transfer between the metal and semiconductor photocatalyst. Moreover, when the spacer layer thickness is increased, the near-electric field could be suppressed. With this idea, a comparison was made between the photocatalytic activity of a reference pristine photocatalyst TiO_2 and plasmonic photocatalyst consisting of TiO_2 and silver nanoparticles with the polyelectrolyte acting as a spacer layer. All the samples were prepared as described in the experimental section with the exception of spin coating technique used to coat the glass substrates. Instead, the silver and silver-polymer core-shell nanoparticles are drop casted onto the dried drop-casted (100 µL of 0.5 wt% suspension) pristine P25 TiO_2 films. The silver nanoparticles concentration was kept same in all the samples i.e., P25_Ag, P25_AgL4 and P25_AgL12, by drop-casting of equal volume (100 µL, $4x10^{11}$ NPs/mL) of colloidal solutions. The FTIR spectra recorded from the online measurement of different systems for acetaldehyde degradation is shown in Figure 2.17 depicting the different stages of photocatalytic reaction.

The online FTIR spectra indicate the different stages involved in the gas phase photocatalytic degradation of acetaldehyde under UV illumination. As shown in Figure 2.17, the different stages involve 20 minutes of pretreatment, 10 minutes of by-pass, 15 minutes of adsorption phase and 20 minutes of illumination stage of the photocatalytic reaction. From the spectra, it is clearly observed that the photocatalytic systems of P25_Ag and P25_AgL4 show better degradation compared to the reference pristine TiO_2 P25 system. This is also corroborated by higher levels of carbon dioxide

being formed during the illumination phase of the photocatalytic reaction. The percentage of degradation for all the photocatalytic systems is calculated based on the molecules of carbon dioxide formed per molecule of acetaldehyde degraded. These values are plotted in Figure 2.18 along with the carbon balance accounting for the formation of two molecules of carbon dioxide formed because of complete degradation of one molecule of acetaldehyde. Figure 2.18 shows that TiO_2 coated with bare silver (P25_Ag) and silver-polymer core-shell nanoparticles of shell thickness 1.4 nm (P25_AgL4) shows an increase of 27% compared to the reference P25 system. But, when silver-polymer core-shell nanoparticles of shell thickness 4.2 nm (P25_AgL12) are used, there is no enhancement in the photocatalytic degradation of acetaldehyde. The loss of photocatalytic activity for P25_AgL12 could be ascertained as a result of suppression of near-field enhancement due to the increased shell thickness. For systems coated with silver-polymer core-shell nanoparticles i.e., P25_AgL4 and P25_AgL12, charge transfer is not possible and these nanoparticles cannot act as charge trap centers[62,105,129]. Therefore, it could be inferred that near-field enhancement plays a dominant role in the Ag-TiO_2 plasmonic photocatalytic systems.

In all the Ag-TiO_2 plasmonic photocatalytic systems discussed until now were prepared by a simple loading of nanoparticles in the form of wet solutions on top of the pre-cast TiO_2 films on glass substrates. This would lead to assumption that further increase in enhancement could be achieved by higher metal loadings on TiO_2. In order to achieve an optimal loading of silver nanoparticles on TiO_2, powders of the samples were prepared by a photo deposition method as described in literature[129]. Briefly, bare silver nanoparticles and silver-polymer core-shell nanoparticles were stirred in TiO_2 suspensions under UV illumination followed by centrifugation to separate the photocatalyst from the water solvent. The color gradient of photocatalyst paste indicate the extent of the deposition process and the process was continued. The powder samples were dried in air at 100 ^{0}C and tested for photocatalytic degradation of stearic acid. However, after the drop-casting of powder suspensions onto silicon wafers, the color of the dried powder films changed to greyish indicating the oxidation

of silver nanoparticles. This indicates that the encapsulating polyelectrolyte layer could not withstand the wet chemical process of photo-deposition.

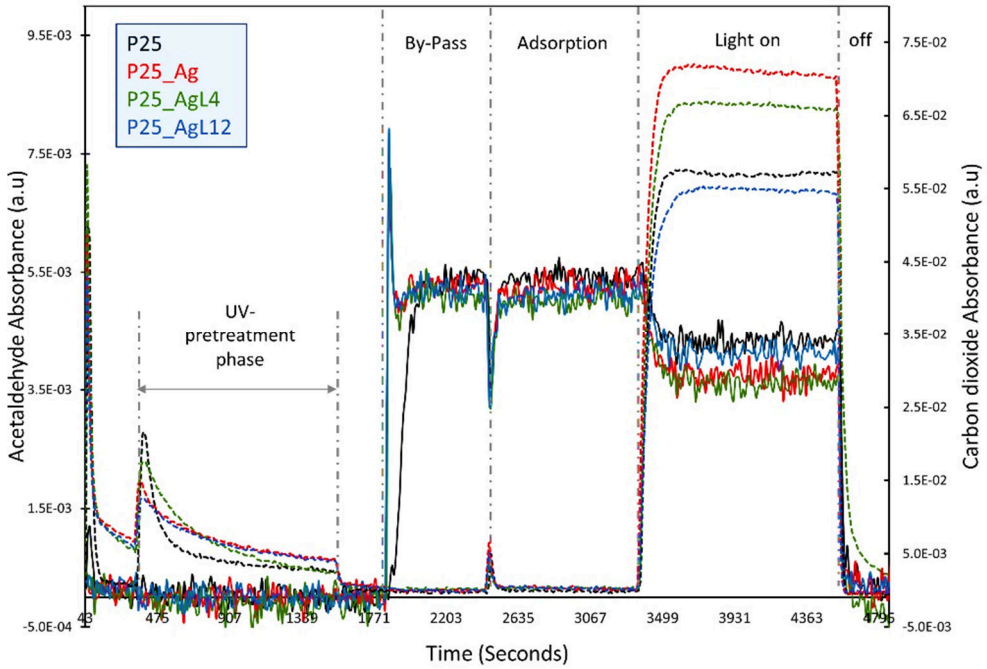

Figure 2.17. FTIR absorption spectra of acetaldehyde (solid lines) and carbon dioxide (dotted lines) recorded for different photocatalytic systems: pristine reference TiO_2 system P25 in black, P25_Ag in red, P25_AgL4 in green and P25_AgL12 in blue. The different stages involved in a single run of the photocatalytic reaction are also shown.

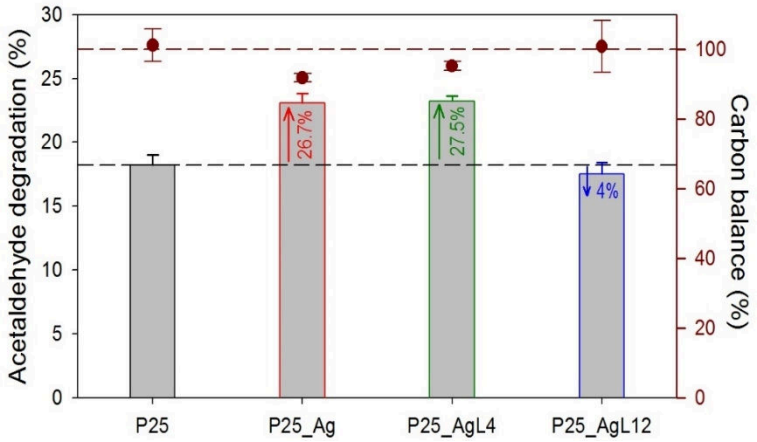

Figure 2.18. Photocatalytic degradation of acetaldehyde (bars) for different systems and the dotted black line indicates the degradation of reference pristine P25 system. The carbon balance for each of the system is shown in dark red.

Moreover, this provides a serous hindrance in utilizing the silver-polymer core-shell nanoparticles in any application that involves wet chemical post processing of nanoparticles as the polyelectrolyte layer is susceptible to damage. At this juncture, it makes sense to test the interaction of polymer with the pristine photocatalyst TiO_2 since UV illumination generate free radicals which are highly reactive. It could be crucial to check whether or not the polyelectrolyte layer is susceptible to damage during the UV irradiation of the Ag-TiO_2 photocatalytic system prepared with silver-polymer core-shell nanoparticles. To that end a pristine TiO_2 P25 film was coated with a polymer solution by dropcasting followed by drying and tested for any formation of carbon dioxide during UV illumination under continuous flushing with air. As seen from Figure 2.19, there was no evidence of formation of intermediate organic molecules, carbon monoxide or carbon dioxide due to the degradation of polymer coating by the free radicals formed by the photocatalytic substrate.

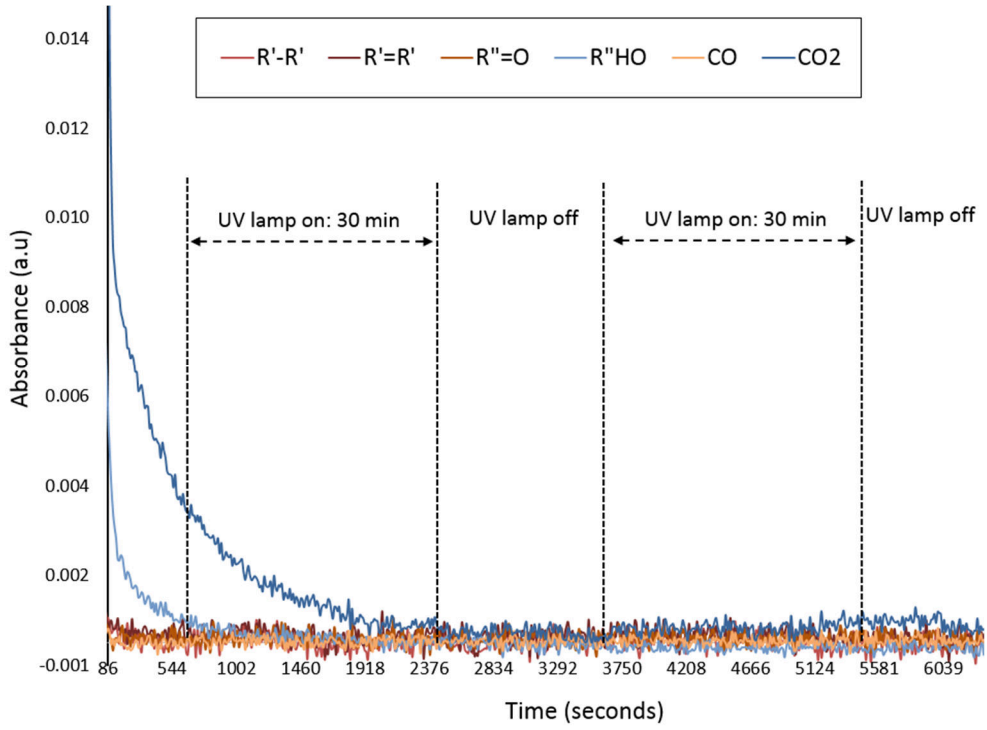

Figure 2.19. Effect of UV light illumination on polymer coated TiO_2 substrate under flushing with air. R'-R', R'=R', R"=O, R"OH, CO and CO_2 represent alkanes, alkenes, aldehydes, carbon monoxide and carbon dioxide band stretch positions respectively in FTIR spectra.

Therefore, it could be concluded that the polyelectrolyte layer is stable during the UV-illumination phase of Ag-TiO_2 plasmonic photocatalytic system prepared by using ultrastable silver@polymer core@shell nanoparticles. In addition, the higher levels of carbon dioxide formed in the photocatalytic tests of the system P25_AgL4 in Figure 2.17 is not due to degradation of polymer present in silver-polymer core-shell nanoparticles.

2.4 *Conclusions*

It was shown that the LbL technique is a versatile and highly controllable strategy to prepare core-shell silver nanoparticles encapsulated by a thin layer of polymer with control up to the sub-nanometer level. Furthermore it is demonstrated that PAA can be used as a cost-effective alternative to PSS in this synthesis method with equally good results. The polymer encapsulation protects the Ag nanoparticles from oxidation and clustering, without compromising the plasmon-induced enhancement of the near--field. This was demonstrated by means of finite element simulations and a long-term photocatalytic environmental experiment toward the degradation of acetaldehyde in air. The plasmonic TiO_2 photocatalyst modified with protected Ag nanoparticles retained its activity enhancement of 15% even after 16 weeks of ageing in air, whereas a similar system fabricated with bare Ag nanoparticles lost its entire activity enhancement over the same time period. With this, an important step in the development of reliable and durable silver-based plasmonic systems was showcased. Additionally a significant further step in understanding the mechanism of near-electric field in Ag-TiO_2 plasmonic photocatalytic systems was achieved, by using the non-conducting polyelectrolyte layer as a spacer layer to suppress the near-field.

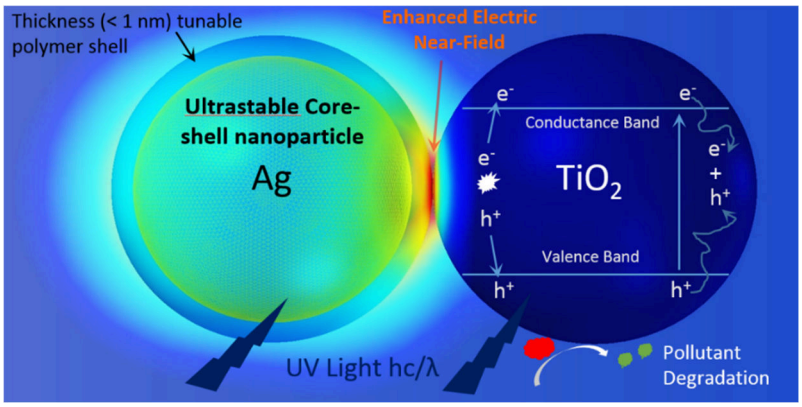

Figure 2.20. A graphical representation of the summary of the chapter.

Chapter 3

Theoretical Mie calculations, modeling and estimation of near-field enhancement

Based on:

***Ramesh Asapu**, Radu-George Ciocarlan, Nathalie Claes, Natan Blommaerts, Matthias Minjauw, Tareq Ahmad, Jolien Dendooven, Pegie Cool, Sara Bals, Siegfried Denys, Christophe Detavernier, Silvia Lenaerts, and Sammy Verbruggen, Plasmonic Near-Field Localization of Silver Core-Shell Nanoparticle Assemblies via Wet Chemistry Nanogap Engineering. "Reprinted (adapted) with permission from **ACS Appl. Mater. Interfaces**, 2017, 9 (47), pp 41577–41585. © 2017 American Chemical Society."*

Contributions: Nathalie Claes, EMAT, University of Antwerp, for TEM analysis.

"All Models are wrong, but some are useful" – George E. P. Box

3.1 *Introduction*

In the previous chapter, it was observed that when silver nanoparticles were encapsulated with a material having a refractive index different from the surrounding medium, the plasmon peak position is shifted. So, an in-depth analysis regarding the phenomenon which effects the near-field and optical properties of silver-polymer core-shell nanospheres, using Mie theory[130] and Finite Element Methods (FEM) is carried out. In brief this chapter looks into the Mie analytical solution for core-shell nanospheres or coated spheres (called BHCOAT in FORTRAN code by Bohren and Huffman[78]) which was implemented in a MATLAB by Adleman[131]. The absorption spectra obtained from the calculated extinction efficiencies based on Mie theory are compared with the experimental absorption spectra of silver-polymer core-shell nanoparticles as synthesized in previous chapter. Additionally studies were performed regarding the repeatability of the red shift in plasmon peak position and shell thickness with variation in batches. In another method, Maxwell's electromagnetic differential wave equations are solved discretized in space of the computational domain for 3D models, finite element method (FEM), in COMSOL Multiphysics. The results were compared with experimental spectra and the trend in red shift of the surface plasmon resonance peak is followed. Initially, Mie theory and its usage through different mathematical programs is studied in more detail. Then more information about the Mie implementation in COMSOL Multiphysics is explored along with the modeling details for estimation of near-field calculations, which will be used extensively in the later chapters of this thesis to support some of the hypothesis.

3.2 *Mie theory analytical calculations*

In 1908 Gustav Mie developed a theory to understand the various optical phenomena of scattering, absorption and extinction for small colloidal gold nanoparticles suspended in water[130]. The mathematics behind the theory consists of determination of a series of coefficients to solve for the vector wave equations derived from Maxwell's electromagnetic wave theory and provided the first framework to

compute scattering of light by small spherical particles. Over decades of research and innovation, Mie theory is now applied in a much broader field ranging from atmospheric science, metamaterials to engineering of plasmonics and near-field optics. Albeit, there is always some amount of assumptions involved, for example with respect to the nanoparticle shape. With a plethora of such simplifications, mathematical conjectures, analysis of pitfalls and potpourri of solutions to Mie theory, Bohren and Huffman compiled a work[78] in 1983, which is still regarded highly. The crucial step forward was the development of an algorithm that simplified the calculations and was compiled in FORTRAN code. This code was later implemented in different programs, by many researchers, to such an extent that as of today there are hundreds of open source codes, which help the nascent physicist to solve Mie equations analytically. In this work, the Mie solution was chosen for a coated sphere or core-shell nanosphere, developed as BHCOAT FORTRAN code by Bohren[78], which was implemented in MATLAB by Adleman[131] in his doctoral thesis. In brief, the code solves for numerous coefficients and calculates the extinction and absorption coefficients for a homogenous sphere after derivation of expressions for scattering and extinction coefficients. Further details on the code and the underlying equations used for these calculations is studied in brief in the following discussion. Consider a single nanoparticle (NP) embedded in a non-absorbing medium as shown in Figure 3.1 and illuminated by a plane wave $\vec{E}_{inc} = \vec{E}_0 e^{ikx - i\omega t}$, where the time-averaged poynting vector $\vec{S}$ i.e., the energy flux at any point in the medium surrounding the particle is expressed as[78]

$$\vec{S} = \vec{S}_{inc} + \vec{S}_{sca} + \vec{S}_{ext} = \frac{1}{2} Re\left[\vec{E} \times \vec{H}^*\right] \quad (1)$$

where "$*$" represents the complex conjugate, the net rate of electromagnetic energy absorbed by the particle within the surrounding sphere is:

$$W_{abs} = \oint_A \vec{S} \cdot \hat{e}_r \, dA \quad (2)$$

The net rate of electromagnetic energy absorbed by the particle can also be written in the form of:

$$W_{abs} = W_{inc} - W_{sca} + W_{ext} \quad (3)$$

For non-absorbing medium W_{inc} vanishes and W_{sca} is the energy rate scattered across surface A. Therefore W_{ext} can be written as the sum of the energy absorption rate and scattering rate:

$$W_{ext} = W_{abs} + W_{sca} \quad (4)$$

It is possible to calculate extinction and scattering cross sections by resolving the scattered field as shown in below equations:

$$C_{ext} = \frac{2\pi}{k^2}\sum_{n=1}^{\infty}(2\mathrm{n}+1)Re\{a_n + b_n\}, \quad C_{sca} = \frac{2\pi}{k^2}\sum_{n=1}^{\infty}(2\mathrm{n}+1)(|a_n|^2 + |b_n|^2) \quad (5)$$

Where k is the wavenumber and a_n, b_n are scattering coefficients computed from equations (6) and (7).

$$a_n = \frac{m\psi_n(mx)\psi'_n(x) - \psi_n(x)\psi'_n(mx)}{m\psi_n(mx)\xi'_n(x) - \xi_n(x)\psi'_n(mx)} \quad (6)$$

$$b_n = \frac{\psi_n(mx)\psi'_n(x) - m\psi_n(x)\psi'_n(mx)}{\psi_n(mx)\xi'_n(x) - m\xi_n(x)\psi'_n(mx)} \quad (7)$$

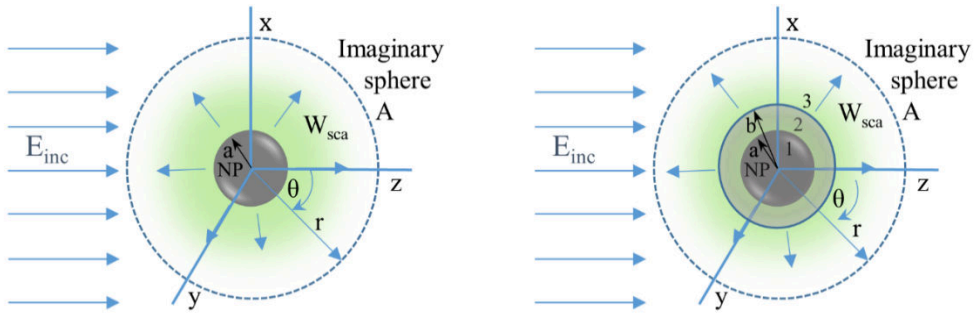

Figure 3.1. Scattering by a) single particle of radius "a" enclosed in medium of imaginary sphere A and b) coated sphere with 1, 2 and 3 as the core, shell and surrounding medium respectively

In the equations (6) and (7), ψ_n and ξ_n are Ricatti-Bessel functions; x is the size parameter $2\pi Na/\lambda$; and the relative refractive index m is N_1/N where N_1 and N are the refractive index of particle and medium respectively. For a coated sphere of uniform shell thickness, as shown in Figure 3.1, application of electromagnetic boundary conditions resolves for the scattering coefficients $a_n$and b_n.

$$a_n = \frac{\{\psi_n(y)[\psi'_n(m_2y) - A_n\chi'_n(m_2y)] - m_2\psi'_n(y)[\psi_n(m_2y) - A_n\chi_n(m_2y)]\}}{\{\xi_n(y)[\psi'_n(m_2y) - A_n\chi'_n(m_2y)] - m_2\xi'_n(y)[\psi_n(m_2y) - A_n\chi_n(m_2y)]\}} \quad (8)$$

$$b_n = \frac{\{m_2\psi_n(y)[\psi'_n(m_2y) - B_n\chi'_n(m_2y)] - \psi'_n(y)[\psi_n(m_2y) - B_n\chi_n(m_2y)]\}}{\{m_2\xi_n(y)[\psi'_n(m_2y) - B_n\chi'_n(m_2y)] - \xi'_n(y)[\psi_n(m_2y) - B_n\chi_n(m_2y)]\}} \quad (9)$$

where the coefficients $A_n$and B_n are given as,

$$A_n = \frac{m_2\psi_n(m_2x)\psi'_n(m_1x) - m_1\psi'_n(m_2x)\psi_n(m_1x)}{m_2\chi_n(m_2x)\psi'_n(m_1x) - m_1\chi'_n(m_2x)\psi_n(m_1x)} \quad (10)$$

$$B_n = \frac{m_2\psi_n(m_1x)\psi'_n(m_2x) - m_1\psi_n(m_2x)\psi'_n(m_1x)}{m_2\chi'_n(m_2x)\psi_n(m_1x) - m_1\psi'_n(m_1x)\chi_n(m_2x)} \quad (11)$$

In the above equations subscripts 1 and 2 refer to core and shell; a and b are the inner and outer radii of the core-shell particle as shown in Figure 3.1; x= ka, y= kb; and $\chi_n(z)$ corresponds to the Riccatti-Bessel function[78]. The algorithm implemented in MATLAB, which solves for absorption and extinction efficiencies for core-shell nanosphere was also used for simple a nanosphere. In the equations (10) and (11), which are used to calculate the coefficients A_n and B_n, if $m_1 = m_2$, then $A_n = B_n = 0$ and the coefficients reduce to those for homogenous sphere as of equations (6) and (7). All the above-mentioned equations were implemented in MATLAB in a sequential pattern where the main script calls multiple subroutines. These subroutines contain supporting functions calculated for each wavelength iteration, which are inputs for the main script. When performing the calculations, the dielectric data for silver, taken from literature[132–134], are implemented through a wavelength dependent data function, which is also called in the main script. The data for water was taken from Segelstein[135]

with a wavelength dependency instead of using a constant value of 1.33. In case of air as surrounding medium, a constant refractive index value of 1 is used. Whereas for polymer shell material, with a combination of either PAH/PAA or PAH/PSS a constant value of 1.48 is taken from literature[136]. A cubic spline function was implemented to plot the calculated extinction, absorbance and scattering efficiencies against the wavelength and the SPR peak position wavelength was identified.

3.3 *Finite Element Method modeling in COMSOL Multiphysics®*

Over the last decade, the evolution of faster computational machines has facilitated the finite element method (FEM) to be highly useful to solve for the differential equations of Maxwell's electromagnetic theory in three dimensions. FEM has the advantage as a highly useful application in coupling of fields and physical quantities, and the capability to solve for periodic structures and arbitrary shapes. The models involve differential equations that are solved for adaptive space discretization of the computational domain, which has a minor drawback with respect to time-consuming and large memory space requirement for complex 3D structures. Although with proper usage of resources and improvisation of solver algorithms with recent versions of computational programs such as COMSOL Multiphysics®, the complexity of 3D models is no longer a concern. In these modeling studies, the COMSOL Wave Optics module is used, in which Maxwell's wave equations are solved with respect to the scattered electric field $\vec{E}_{sca}$, which is:

$$\nabla \times \left[\frac{1}{\mu_r}\left(\nabla \times \vec{E}_{sca}\right)\right] - {k_0}^2\left[\left(\varepsilon_r - \frac{i\sigma}{\omega\varepsilon_0}\right)\right]\vec{E}_{sca} = 0 \quad (12)$$

where k_0 is wavenumber, ω is angular frequency, μ_r is relative permeability of medium, σ is electrical conductivity of medium and ε_0, ε_r are permittivity of free space and medium respectively. From equation (1), the incident energy flux i.e., time-averaged poynting vector is calculated as:

$$\vec{S}_{inc} = \frac{1}{2}\, Re\left[\vec{E}_{inc} \times \vec{H}^*{}_{inc}\right] \quad (13)$$

For an incident plane wave, the magnetic field is related to the electric field by:

$$\vec{H}_{inc} = \frac{1}{\eta}\hat{e} \times \vec{E}_{inc} \quad (14)$$

where $\hat{e}$ is direction vector of the incident wave propagation, $\eta = \sqrt{\mu_r/\varepsilon_r}$ is characteristic wave impedance. Hence, the incident energy flux becomes:

$$\vec{S}_{inc} = \frac{1}{2}c\varepsilon_r\left|\vec{E}_{inc}\right|^2\hat{e} \quad (15)$$

The rate of electromagnetic energy that is absorbed (W_{abs}) and scattered (W_{sca}) divided by the incident energy flux can be quantified as absorption and scattering cross sections[78]:

$$C_{abs} = \frac{W_{abs}}{\left|\vec{S}_{inc}\right|}, \quad C_{sca} = \frac{W_{sca}}{\left|\vec{S}_{inc}\right|} \quad (16)$$

In FEM models, the incident energy is calculated as a defined parameter as shown in equation (17). Whereas the total absorbed energy is derived by volume integration of energy loss over the particle and total scattered energy is derived by surface integration of scattered energy flux as represented by equation (18). These values are calculated using the built-in variables list in COMSOL as shown in equations (19) and (20).

$$\left|\vec{S}_{inc}\right| = \frac{{E^2}_0}{(2 * Z_0)} \quad (17)$$

$$W_{abs} = \iiint_{NP} Q_{loss}dV \quad \mathrm{W_{sca}} = \oiint_{\mathrm{A}} \vec{\mathrm{S}}_{\mathrm{sca}} \cdot \hat{\mathrm{n}}\mathrm{dA} \quad (18)$$

$$C_{abs} = \frac{\iiint \text{"}ewfd.Q_h\text{"}\, dV}{\mathrm{E^2}_0/(2 * \mathrm{Z}_0)} \quad (19)$$

$$C_{sca} = \frac{\oiint \text{"}relPoav\text{"}\, dA}{\mathrm{E^2}_0/(2 * \mathrm{Z}_0)} \quad (20)$$

Equations (17) through (20) were implemented in COMSOL where V and A represent the volume and surface area of imaginary sphere around the particle in Figure 3.1, "n̂" is the unit vector normal to the imaginary sphere and "E_0" is the incident electric field. Q_{loss} is rate of energy loss, Z_0 is the impedance of free space; which are denoted as total power dissipation density "$ewfd.Q_h$" and "$Z0\_const$" respectively in COMSOL built-in variables list. The integration variable for scattered energy flux is "$relPoav$" which is the time averaged pointing vector of scattered field obtained by the summation of three-dimensional components of the product of refractive index denoted as "n_x, n_y, n_z", and relative time averaged power field denoted as "$ewfd.relPoav_x, ewfd.relPoav_y, ewfd.relPoav_z$" in COMSOL built-in variables list. The absorption cross-section was integrated over the volumetric domain of the nanoparticle and scattering cross section was integrated over the surface domains in the model. The efficiencies were calculated by dividing the cross-section with the geometric cross section of the nanoparticle. The model with mesh structure and a histogram of the element quality are shown in Figure 3.2. The outer sphere is the perfectly matched layer (PML) to truncate the physical domain and avoid internal reflections to represent the physical system in an infinite space medium. The 3D sphere at the center is the silver nanoparticle with an encapsulating polymer layer that is meshed independently. In case of dimers or multiple nanoparticle clusters, the polarization was modified with respect to direction of alignment of nanoparticle arrays. It is important to know that wave optics physics module can only be used in the case when the size of the particle being modeled is very small compared to the incident light wavelength i.e., d<<λ. In all other cases ray optics and AC/DC models should be used when the geometry of the particles are comparable to incident electromagnetic radiation i.e., the incident light wavelength.

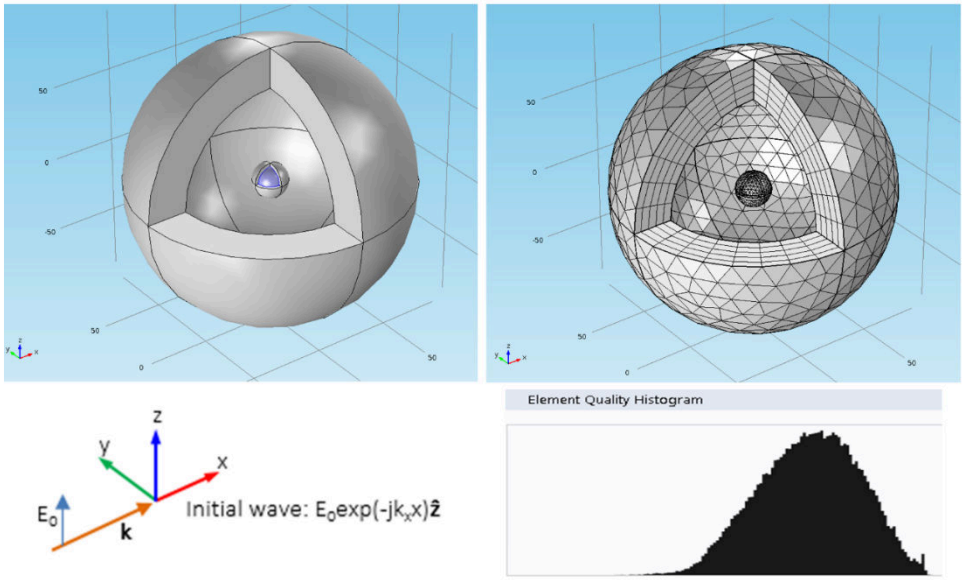

Figure 3.2. 3D FEM models with meshing and a histogram of element quality for a system representing silver-polymer core-shell nanoparticle.

3D models of bare silver nanospheres, silver-polymer core-shell nanospheres with varying polymer shell thickness were built in the wave optics physics in COMSOL Multiphysics (version 5.1/5.3). A plane wave polarized in the Z-axis direction and propagating along the X-axis direction was solved for the scattered field in a wavelength domain study. As mentioned before, to calculate the extinction and absorption efficiencies, the incident excitation wavelength of the monochromatic plane wave was varied in the range of 300-700 nm. COMSOL Multiphysics has built-in wavelength dependent refractive index data in its material database, adapted from Johnson and Christy[132], and the refractive index data for water is imported as a cubic interpolated data from Segelstein[135]. To represent the silver-polymer core-shell nanoparticle, a 3D sphere of 18/20 nm in diameter was built and a shell was added on the silver core with varying thickness to represent the polymer shell. The refractive index of the polymer shell system (n = 1.48) was taken from literature[136]. The polymer domain was meshed using a custom setting for a maximum element size of one nm and all the models had at least 105 tetrahedral elements with mesh quality of at least around 0.7.

3.4 *Results and discussions*

3.4.1 Comparison of experimental and theoretical optical properties

Silver-polymer core shell nanoparticles were prepared by sequential cycles of adsorption and washing of alternately charged polyelectrolytes, as described in more detail in previous chapter. The alternate deposition of polycation and polyanion chains was continued until the desired number of layers was obtained which results in the encapsulation of the silver core by an ultra-thin polymer shell. UV-vis absorption spectra of the core-shell nanoparticles were recorded after each deposition step as shown in Figure 3.3a. The decrease in intensity corresponds to loss of nanoparticles during the multiple cycles of washing and centrifuging. A red shift of the plasmon peak with increasing number of adsorbed layers can be observed in Figure 3.3b, which is an indication of the gradual increase in particle size due to an increase in encapsulating

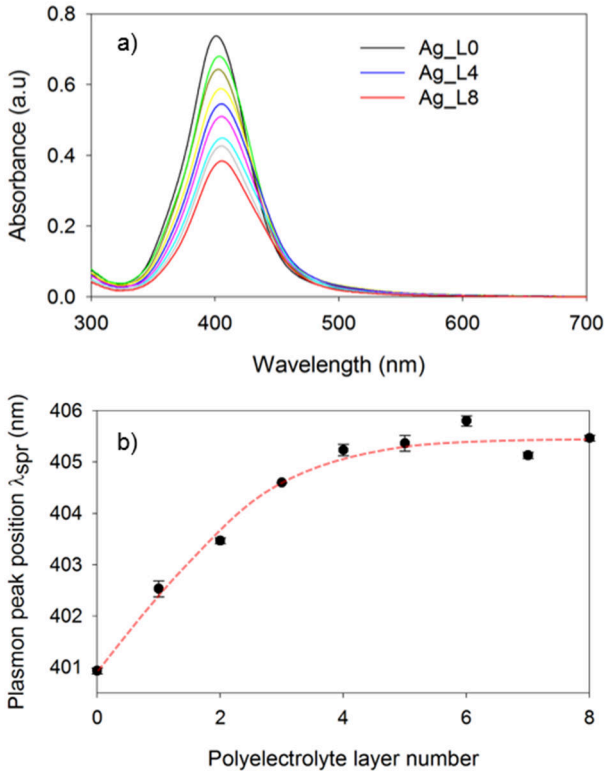

Figure 3.3. a) UV-vis absorption spectra and b) surface plasmon peak position of silver core-shell nanoparticles as a function of the number of adsorbed polyelectrolyte layers. The dotted red curve is a trend line of the shift in plasmon peak position.

polymer shell thickness as more LbL layers are added. As discussed in section 2.3.1 there is a small variation in the shell thickness of the core-shell nanoparticles for multiple batches. For theoretical calculations, average values of the shell thickness and nanoparticle size are required to input in both MATLAB script and COMSOL. So the LbL synthesis of an eight layered silver-polymer core-shell nanoparticles i.e., Ag_L8 or $Ag(PAH/PAA)_4$ was done in triplicate in order to get an idea regarding the repeatability and the error factor for these experiments.

As seen from the Figure 3.4a it is clear that there is a small variation (± 2 nm) in the absolute position of the plasmon peak (dotted lines). This may be because of the minor variation in stock silver colloidal solution and from the small fluctuations from the of UV-vis spectrophotometer on different days. However, it is clear that the magnitude of red shift in plasmon peak (solid lines) is of the same order for all the three different batches of replicated LbL syntheses protocol. The shell thickness measurements from the TEM images (Figure 3.4b) for all the three replicates are also in the same order with a variation of ±0.2 nm in the mean values. The individual TEM images for the three replicated batches are shown in Figure 3.4c. The average size of the silver nanoparticle, which also forms the core of the silver-polymer core-shell nanoparticles, is taken as 20 nm from the size distribution profile as obtained from the TEM analysis (Figure 3.4d). The absorbance calculated from Mie analytical MATLAB code and COMSOL was plotted with the experimental absorption spectrum as shown in Figure 3.5. The optical constants data used for these calculations was taken from literature. since there are numerous well known datasets, silver permittivity data from Johnson & Christy[132], Palik[133] and Ripken[134] were used and represented as Mie_J&C, Mie_Palik and Mie_Ripken respectively in the plots for convenience.

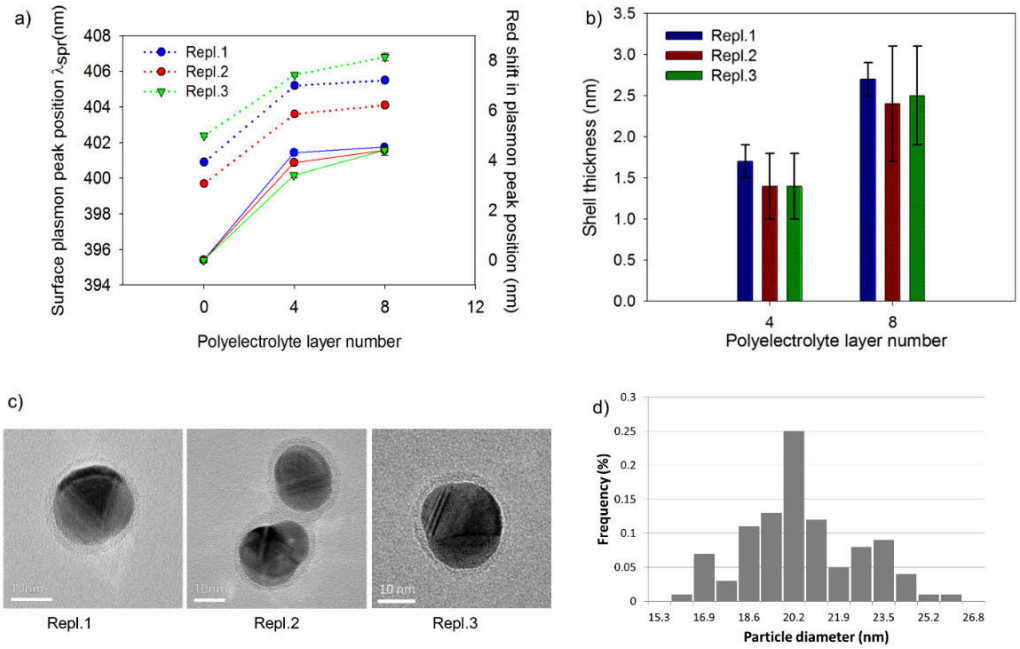

Figure 3.4 a) Absolute value of the surface plasmon peak position (dotted lines) and red shift in plasmon peak position (solid lines) as a function of polyelectrolyte layer number for three replicated experiments/batches: Repl.1, Repl.2 and Repl.3, b) shell thickness as a function of polyelectrolyte layer number as measured from TEM images for the three replicated experiments, c) BF-TEM images for eight layered (Ag_L8) silver-polymer core-shell nanoparticles from three replicated experiments and d) a histogram showing the silver nanoparticle size distribution with an average diameter of 20 nm.

From the plots, a clear red shift can be observed in all spectra for silver-polymer core shell nanospheres with a shell thickness of 2.7 nm (Ag_L8, Figure 3.5b) and this for all used datasets. There seems to be a striking difference in the absolute value of the peak position, as well as the shape of the spectrum when using multiple datasets as compared to experimental spectra for both bare Ag nanoparticle and core-shell nanoparticles. This can be attributed to the fact that in Mie analytical calculations and the COMSOL model, the nanoparticles are assumed perfectly spherical, of a single size and highly monodisperse, which is rarely the case in a true experimental scenario. The polydispersity of synthesized colloidal nanoparticles is related to the full peak width at half maximum (FWHM) of the spectra, which is not taken into account in Mie calculations nor the COMSOL model. These assumptions will always lead to plasmon

band narrowing and a minor shift in the band position for analytical calculations, which is well in line with the literature[67,137,138]. It is also important to note that the datasets used from different researchers vary because the experimental methods used to generate the optical constants are quite different. In addition, each method uses independent corrections in mean free path of electrons for the calculations of the dielectric parameters, in cases where particle sizes get too small. However, the trend in the red shift of plasmon peak position with increased shell thickness is mostly in agreement with the experiments (Figure 3.6). Still, for a shell thickness of 2.7 nm (Ag_L8), the red shift becomes less substantial than for thinner shells (also clear from the plateau that is reached in Figure 3.3b).

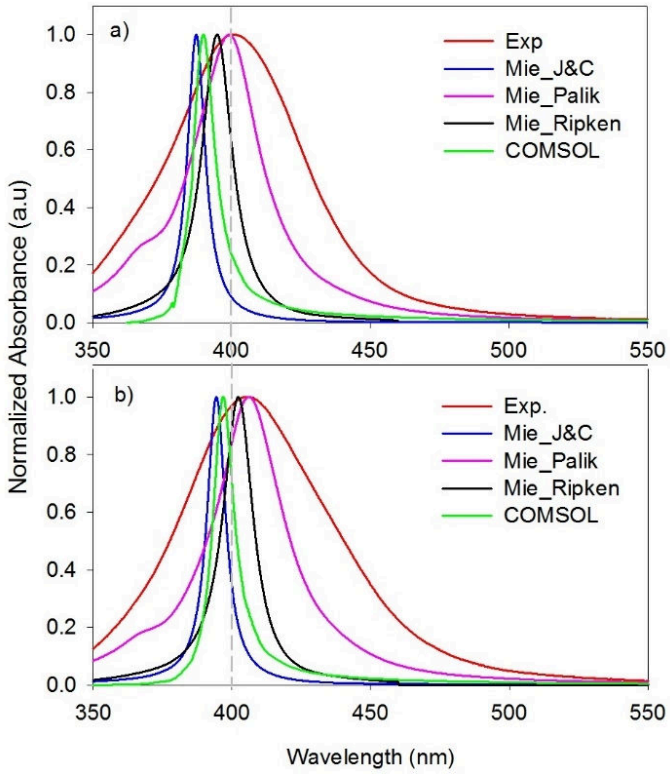

Figure 3.5. Comparison of normalized UV-vis experimental spectra with calculated theoretical absorption efficiencies for a) bare silver nanospheres and b) silver-polymer core-shell nanospheres with 2.7 nm shell thickness (Ag_L8).

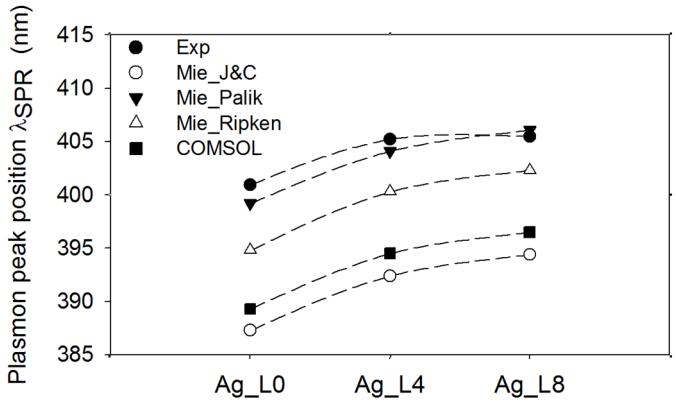

Figure 3.6. Comparison of experimental spectra with theoretical calculations in water, showing the Plasmon peak position of bare (Ag_L0) and core-shell nanospheres (Ag_L4, Ag_L8).

The theoretical calculations on the other hand still show a significant red shift with increase in polymer shell thickness. Such an experimental leveling off of the red shift is expected for core-shell nanoparticles with thick optically transparent shells, as the shift in the plasmon peak becomes insignificant[138]. It also depends on the refractive index of the surrounding medium, as obviously noticeable from the theoretical equations (section 3.1). Figure 3.7 depicts the trend in red shift of the plasmon peak with increasing shell thickness, calculated for air and water as surrounding media.

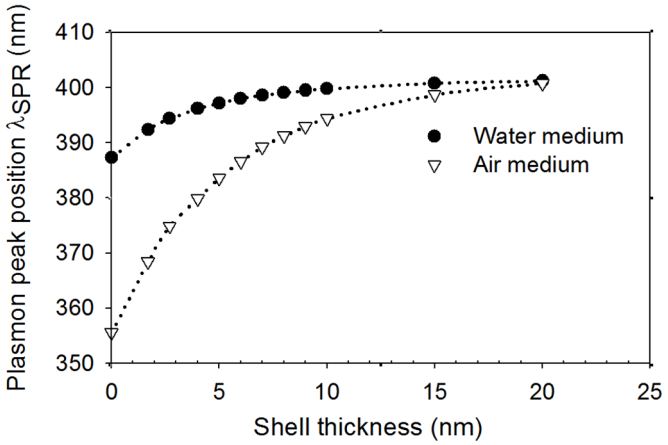

Figure 3.7. Mie analytical calculations showing the red shift in plasmon peak position as a function of increasing polymer shell thickness for core-shell nanospheres in air and water as the surrounding medium.

This implies that, as the ratio of the refractive indices of the shell *versus* the surrounding medium becomes closer to unity, the red shift in plasmon peak as a result of increasing shell thickness will slowly disappear. In other words, there would be a blue shift in plasmon peak position if the core-shell nanoparticles were suspended in a medium with a refractive index that is higher than the refractive index of encapsulating shell material. Among all the datasets, Mie_Palik seems to match best with the experimental red shift (Figure 3.6). For the experimental dataset a plateau value is reached, which is not yet the case for the theoretical calculations in this range of shell thickness. This deviation can potentially be attributed to the use of a constant refractive index for a composite of polyelectrolyte layers in the calculations. From a practical point of view, small deviations in shell thickness or imperfections within the polymer composite are also possible. Overall, it should be clear that the shell thickness is a crucial factor for plasmonic core-shell nanoparticles as it has a significant effect on both optical as well as near-field properties. Therefore, the effect of polymer shell thickness on the near-field enhancement was studied in the following discussion.

3.4.2 Near-electric field simulations using COMSOL Multiphysics®

Near-field enhancement of the silver nanoparticles was studied by finite element analysis using wave optics physics in COMSOL Multiphysics®[139]. To represent the bare silver nanoparticle, a 3D sphere of 18 nm in diameter was built and a shell was added on the silver core with varying thickness to represent the polymer shell. The effect of the polymer shell on the plasmonic near-field enhancement of the silver nanoparticles is studied by a finite element analysis. The accuracy and dependency of the results from the 3D COMSOL models was already validated by the Mie implantation as discussed in previous section. Since the results from COMSOL also show a similar trend as the experimental spectra and other Mie analytical solutions, the models can be considered as a representative system for estimating the near-field enhancement. In this section, the effect of polyelectrolyte layer thickness on the near-electric field at the surface of silver-polymer core-shell nanoparticles is analyzed. Figure 3.8 shows the normalized electric field enhancement $(|E|/|E_0|)^2$ emanating from the surface of a 20

nm bare silver nanoparticle, this silver particle encapsulated by a polymer shell of thickness 1.4 nm (alike Ag_L4) and finally the silver particle encapsulated by a polymer shell of thickness 2.4 nm (alike Ag_L8). The color map represents the normalized electric field intensity distribution visualized on the ZX plane. An incident monochromatic plane wave propagating along the X-axis and polarized along the Z-axis with $\lambda_{Incident} = \lambda_{SPR}$ (taking into account the red shift with increasing layer thickness) for each nanoparticle system is used for the numerical simulations. This means the incident excitation wavelength of the monochromatic plane wave was always kept the same as the surface plasmon resonance wavelength of the respective core-shell nanoparticle system. So for each system the maximal field enhancement was simulated after excitation at the SPR maximum with air as the surrounding medium. The numerical values of field enhancement near the vicinity of the nanoparticles along the Z-axis, i.e. in the direction of polarization, are on display below the corresponding field maps. It can be observed that the bare Ag nanoparticle and the Ag_L4 core-shell nanoparticle have similar field intensities propagating from the exterior particle surface, but Ag_L8 exhibits a much stronger field within the shell. This is an indication

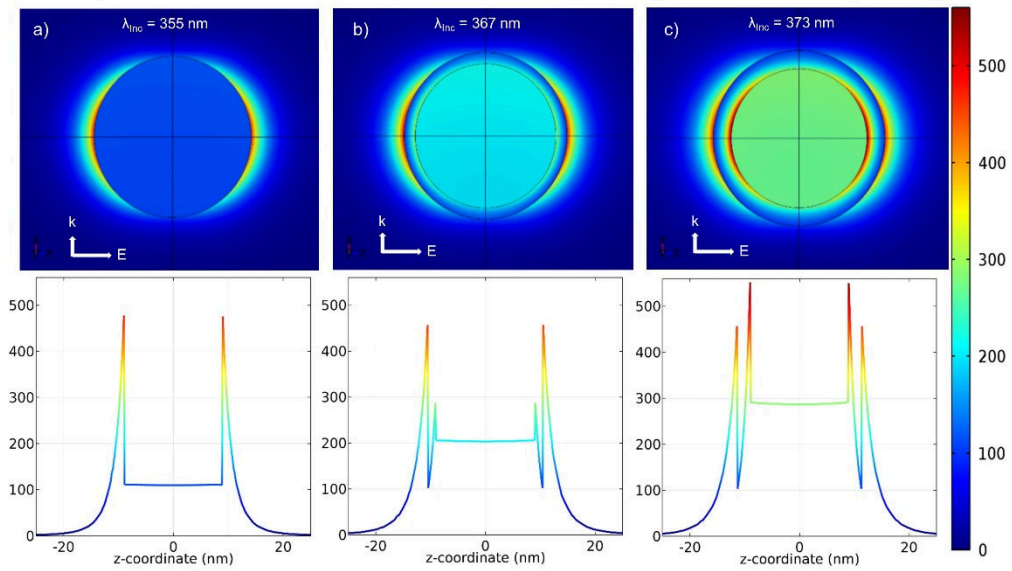

Figure 3.8. Electric field distribution maps $(|E|/|E_0|)^2$ for a) bare Ag NP, b) Ag NP encapsulated by a polymer shell of thickness 1.4 nm, alike Ag_L4 and c) Ag NP ecapsulated by a polymer shell of thickness 2.4 nm, alike Ag_L8. The field enhancement along the Z-axis, i.e. in the direction of polarization, is plotted below the corresponding field maps.

that as the polymer shell thickens; the field becomes localized within the shell, which will result in a drastic loss of the plasmonic enhancement effect near the particle surface. Since the near-electric field becomes localized within the polymer shell, an analysis regarding the dependence of emanating field intensity on the polymer shell thickness is performed. This was done by building models of silver-polymer core-shell nanoparticle with increasing shell thickness. Since it was already observed that as the shell thickness increases, there is a red shift in the plasmon peak position, so it is crucial to know the plasmon peak position for each core-shell nanoparticle system with different shell thickness. Using the Mie analytical solution, the plasmon peak position for core-shell nanoparticle with different shell thickness was identified. The values are listed in Table 3.1. All the 3D models with different shell thickness are simulated at an incident wavelength of the corresponding surface plasmon resonance peak wavelength of the core-shell nanoparticle system as listed in Table 3.1. The intensity of field enhancement is maximum when the light at a wavelength matching with the plasmon resonance peak wavelength excites the core-shell nanoparticle. This maximum field intensity is generally observed at the immediate vicinity at the surface, so the values of maximum field enhancement factor are logged for all the models and

Ag@poylmer core@shell nanoparticle in air: core 18 nm dia.	
Shell Thickness (nm)	Plasmon peak position (λ_{SPRmax})
0	355
1.4	367
2.4	373
3	377
4	381
5	385
7.5	387
10	395

Table 3.1. Effect of polymer shell thickness on maximum enhancement factor near the outer surface of core shell nanoparticle, as determined from finite element.

plotted in Figure 3.9. It can be observed that with the increase in shell thickness, up to a shell thickness of 3 nm, the drop in field enhancement factor is relatively insignificant. But the enhancement already drops by ca. 50% for a shell thickness of 5 nm and becomes almost non-existent for a core-shell nanoparticle with shell thickness of 10nm. In the previous chapter, different plasmonic photocatalyst systems were tested for gas phase photocatalytic activity using the polyelectrolyte as a spacer layer. The suppression of near-field is displayed as the polyelectrolyte layer thickness is increased as shown in Figure 3.8. The photocatalytic experiments were conducted by illuminating the samples using a 25W UVA lamp that has a peak light emission wavelength at 365 nm. So it would interesting to visualize the near-electric distribution maps at an incident light wavelength of 365 nm instead of the peak surface plasmon resonance wavelength of the nanoparticle system as disused before in previous paragraph. The near-field distribution maps obtained from the FEM simulations are shown in Figure 3.10. It could be observed that the silver@polymer core@shell nanoparticles with four layers (Ag_L4) i.e., shell thickness of 1.4 nm, shows a good overlap of the incident light wavelength and surface plasmon resonance wavelength as expected from the tabled values in Table 3.1.

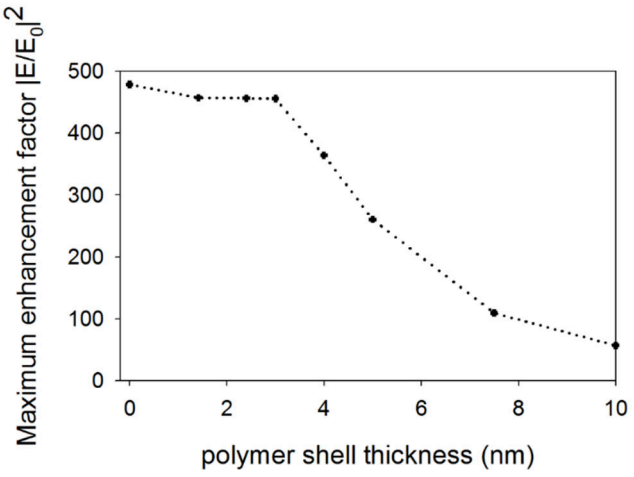

Figure 3.9. Effect of polymer shell thickness on maximum enhancement factor near the outer surface of core shell nanoparticle, as determined from finite element simulations.

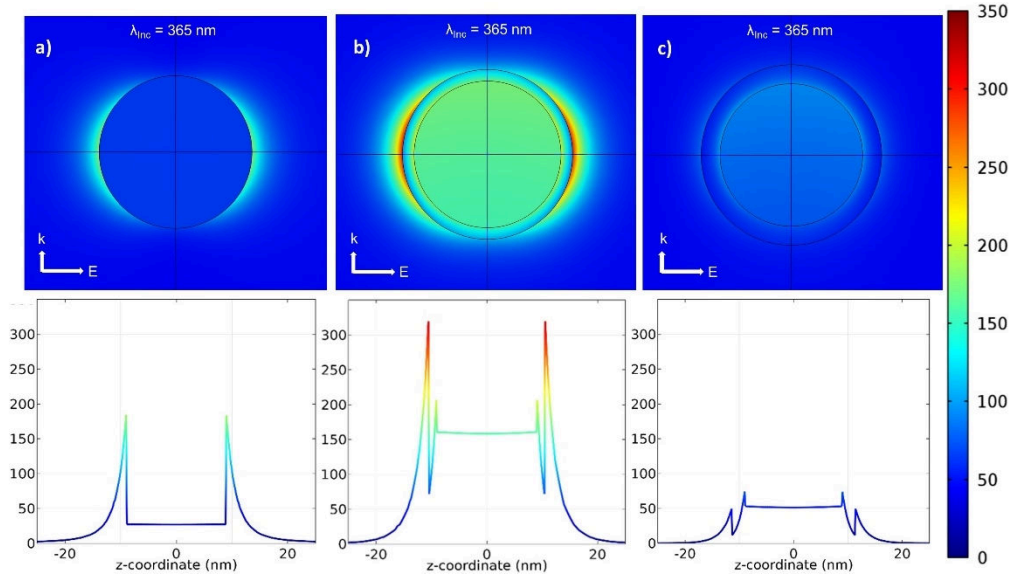

Figure 3.10. FEM simulation maps of the electric field distribution $(|E|/|E_0|)^2$ for a) bare silver nanoparticle, b) silver encapsulated by a polymer shell of thickness 1.4 nm, alike Ag_L4 and c) silver encapsulated by a polymer shell of thickness 2.4 nm, alike Ag_L8. Field enhancement along the Z-axis is plotted below the corresponding field maps. The excitation wavelength of 365 nm corresponds to the peak wavelength of the UVA lamp used in the photocatalytic activity tests. Air is the surrounding medium for all simulations.

Even though bare silver nanoparticles does seem to have lower enhancement, it should be noted that the enhancement is close to 200 and is significant enough to enhance the photocatalytic activity as discussed in previous chapter in Figure 2.13. Also, the simulation models simplify the Ag-TiO_2 plasmonic photocatalyst system, by modeling single silver nanoparticles. But in reality there is good possibility that multiple clusters of silver nanoparticles give rise to a hot spot effect of plasmonic nanoparticles in contact with TiO_2 to enhance the photocatalytic activity.

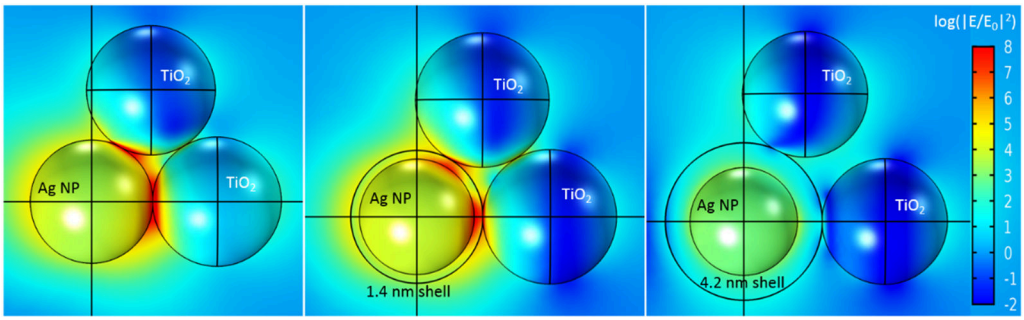

Figure 3.11. Effect of polymer spacer layer on the near-electric field at the interface of plasmonic Ag metal and semiconductor photocatalyst TiO_2 with excitation λ_{inc}= 365 nm.

The analysis of near-electric suppression was further studied by building Ag-TiO_2 plasmonic photocatalytic system models of increasing shell thickness (Figure 3.11). The near-field maps show that the contact between the silver nanoparticle and TiO_2 results in very intense near-electric field at the interface. However, with increased shell thickness suppresses the magnitude of near-electric field at the interface of plasmonic silver metal and semiconductor TiO_2 photocatalyst. In the discussion pertaining to the long-term gas-phase photocatalytic activity of Ag-TiO_2 plasmonic photocatalytic system in section 2.2.3, the formation of diffuse silver oxide layer around the silver nanoparticle was hypothesized leading to loss of photocatalytic activity. Silver nanoparticles tend to oxidize and form a diffuse silver oxide (Ag_2O) layer around the nanoparticle[126,127,140], so its effect on the near-field enhancement of the silver nanoparticles is studied by building a finite element model using wave optics physics in COMSOL Multiphysics as described previously. Figures 3.12a and 3.12b shows the normalized electric field enhancement $|E/E_0|^2$ maps of bare silver nanoparticle of d~18 nm (solid line) and silver encapsulated by a Ag_2O shell of 2 nm thickness (silver core of d~14 nm and a 2 nm thick shell of oxidized silver) respectively.

The numerical values of field enhancement emanating from the particle surface along the direction of polarization are displayed with the corresponding field enhancement legend color maps that demonstrate a significant drop. This drop is shown in line plots as a function of distance from the surface of nanoparticle in Figure 3.12c, which is around 60-fold decrease of the maximum field enhancement. The optical data for silver oxide (Ag_2O) is taken from literature[141]. This clearly supports the hypothesis that the near-field enhancement drops for oxidized silver nanoparticles resulting in a detrimental loss in plasmonic enhancement of the P25_Ag photocatalyst.

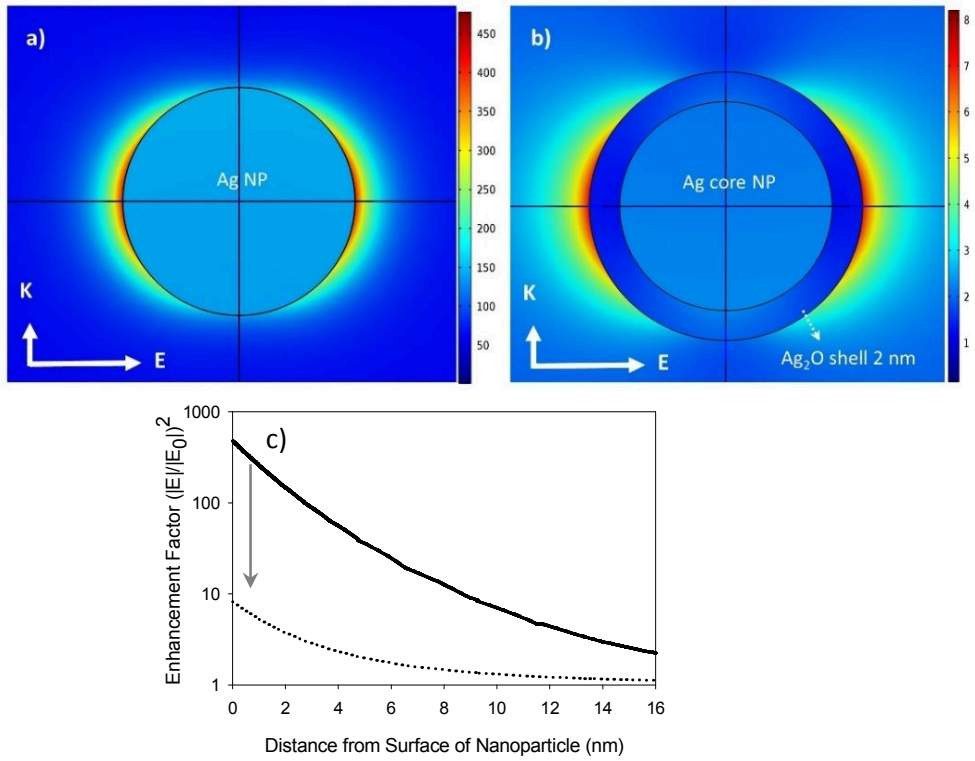

Figure 3.12. Near-electric maps (λ_{inc} 365 nm) of a) silver nanoparticle and b) Ag@Ag_2O nanoparticle with Ag_2O shell thickness of 2 nm. The legend scale c) Comparison of enhancement factors of bare silver nanoparticle (solid line) and after formation of a 2 nm thin silver oxide shell (dotted line) at the nanoparticle surface. The arrow indicates the drop in maximum enhancement factor.

3.4.2.1 Mesh refinement study

The quantification of the near-electric field is subjective to the conditions and assumptions considered during the modeling phase. The magnitude of enhancement factor (EF) of the near-electric field at the surface of the nanoparticle for all the simulation maps analyzed is dependent on the surface meshing size. So all the surface meshing sizes were kept similar so that it would not lead to results providing false trends. Additionally, a mesh analysis was performed on a nanoparticle dimer system (Figure 3.13) to see the effect of surface mesh size on the magnitude of near-electric field at the hot spot, which is typically maximum at the exact center of the distance separating the two nanoparticles. The results are listed in Table 3.2, and show that the magnitude of maximum point of near-field enhancement vary significantly, as the

mesh density along the nanoparticle surface is refined. However, highly fine-tuned meshing result in large computational times as the number of mesh elements increase. Therefore, appropriate mesh density should be chosen, so that the very high computational efforts that do not lead to significant betterment of results are avoided. So in all the models, as a minimum condition, approximately overall mesh quality value of 0.7 is maintained.

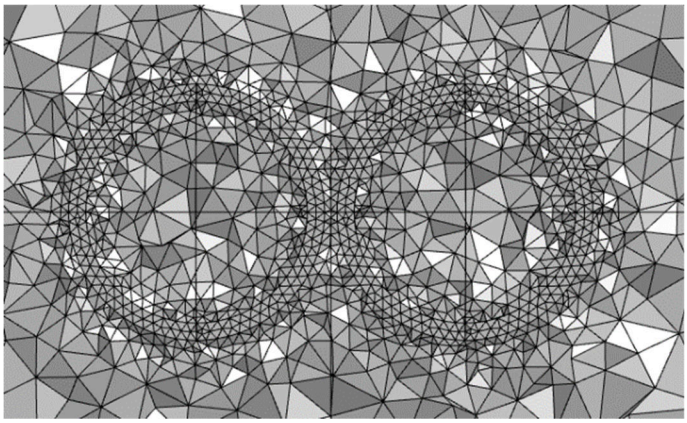

Figure 3.13. Mesh plot of nanoparticle dimer on which mesh analysis was performed.

Mesh Density	Number of Elements	Computation time [s]	Max point of (Norm. E-field)^2
Normal	10374	9	3.13E+05
Fine	16588	11	4.64E+05
Finer	42048	24	4.21E+05
Extra fine	135833	85	3.50E+05
Extremely fine	647861	609	3.45E+05

Table 3.2. Mesh analysis of the nanoparticle dimer system as shown in Figure 3.12

3.4.3 Time domain simulation of plasmonic nanoparticle interaction with light

Time domain simulations of the plasmonic nanoparticles provide an animated view of the interaction of incident light photons at the plasmonic metal-dielectric interface. This was achieved by modeling the silver nanoparticle in air medium using the time domain study of the wave optics physics in COMSOL Multiphysics®. The transient modeling in wave optics physics is simplified for a plasmonic nanoparticle by confining the particle within a small space-time domain by appropriate usage of boundary conditions as shown in the scheme in Figure 3.14. The Scheme in Figure 3.14 represents the modeling domain and methodology adopted so that the three-dimensional vector quantities that needs to be solved in time domain could be reduced and eventually decrease the computational effort. A series of multiple screen captures of the animated results from the time domain simulation are shown in Figure 3.15 for a silver nanoparticle with increments in 0.05-femtosecond units. The scale for the color map was normalized in arbitrary units to have a better visualization of the near-field mapping. From the images, it could be observed that the beam of photons in the form electromagnetic radiation in air medium polarized in the z-axis direction and propagating along the x-axis, excite the dielectric metal nanoparticle along the direction of polarization. It could be inferred that intense electric fields are generated along the metal-dielectric interface as the light/photon beam traverse past the nanoparticle leaving a trail of oscillating high-density electron clouds in the form near-electric field. This enhancement in the near-electric field in the direction of polarization of light is a distinctive feature of plasmonic nanomaterial interaction with a dielectric medium at the plasmon resonance wavelengths. The visualization of this phenomenon in a time-domain in the form of animation provides a more comprehensive understanding of the concept of surface plasmons.

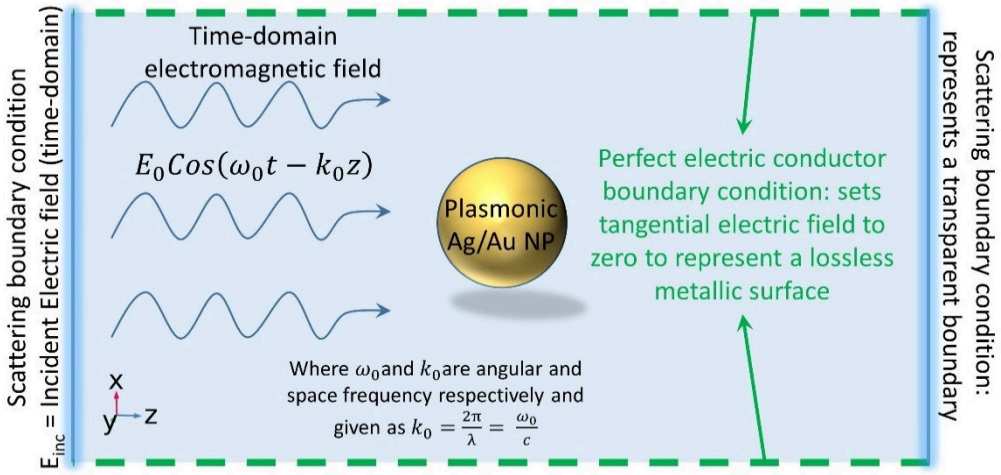

Figure 3.14. Schematic representation of modeling methodology implemented for time-domain simulations in vacuum.

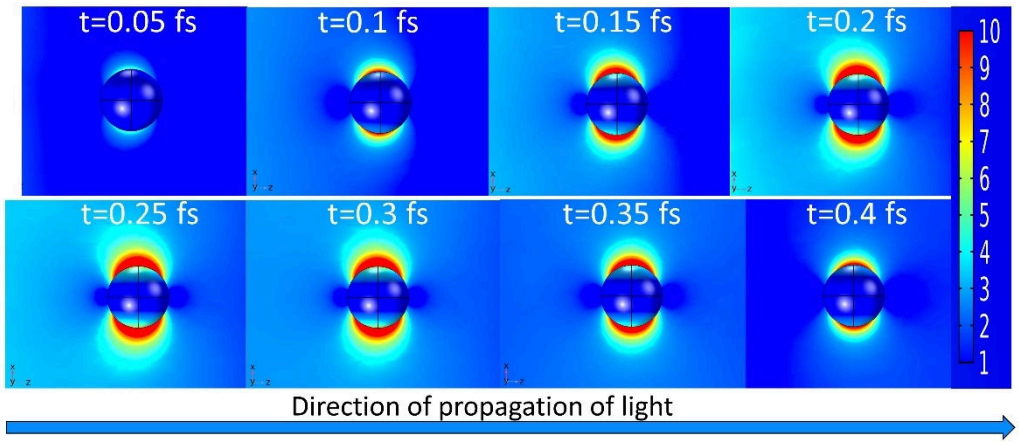

Figure 3.15. Time series images displaying the interaction of silver nanoparticle of size 20 nm in vacuum, with electromagnetic radiation incident at the surface plasmon resonance wavelength of 355 nm. The light is polarized in the direction perpendicular to propagation. The scale of the color legend is arbitrary for the field enhancement i.e., $(|E|/|E_0|)^2$.

3.5 *Conclusions*

In this chapter, a thorough study of the Mie theoretical calculations were performed by implementing the analytical solution for a coated sphere by Bohren and Huffman[78] in MATLAB. The experimental absorption spectra was compared with the theoretical estimation and a good match was found for the red shift in plasmon peak position of silver-polymer core-shell nanoparticles with the increase in shell thickness. The repeatability of the synthesis of ultrathin polyelectrolyte shell was also analyzed by performing multiple measurements and using the average value of shell thickness in the theoretical calculations. Finite element modeling was also used to estimate the surface plasmon peak position using COMSOL Multiphysics®, which is a versatile program. The process of implementing the Mie analytical solution and calculating the absorption and scattering efficiencies in COMSOL were discussed in detail, which were also in good agreement with Mie analytical solution and experiments. In the later part near-field simulations were performed for the silver and silver-polymer core-shell nanoparticles. The effect of increasing the polyelectrolyte shell thickness on the near electric field at the surface of the nanoparticle was studied and the simulations provided an in-depth perspective of the application in plasmon enhanced photocatalysis. The near-field maps at the interface of silver-polymer core-shell nanoparticle and TiO_2 corroborate the experimental photocatalytic results discussed in the prior chapter and support the hypothesis that near-electric field plays a significant role in Ag-TiO_2 plasmonic photocatalytic systems. In the following chapter, the finite element models are also used to support the experimental results to quantify the distance dependency of the near-electric field for plasmonic nanoparticle. Therefore, it could be concluded that theoretical modeling provides crucial insights into the behavior of plasmonic systems and acts as a vital mechanistic tool to corroborate the experiment results.

Chapter 4

Quantifying the distance dependency of plasmonic near-field enhancement through Surface Enhanced Raman Spectroscopy (SERS)

Based on:

***Ramesh Asapu**, Radu-George Ciocarlan, Nathalie Claes, Natan Blommaerts, Matthias Minjauw, Tareq Ahmad, Jolien Dendooven, Pegie Cool, Sara Bals, Siegfried Denys, Christophe Detavernier, Silvia Lenaerts, and Sammy Verbruggen, Plasmonic Near-Field Localization of Silver Core-Shell Nanoparticle Assemblies via Wet Chemistry Nanogap Engineering. "Reprinted (adapted) with permission from **ACS Appl. Mater. Interfaces** 2017, 9, 41577-41585. © 2017 American Chemical Society"*

Contributions: Nathalie Claes, EMAT, University of Antwerp, for TEM analysis.

Radu-Ciocarlan George, LADCA, University of Antwerp, for Raman spectroscopy measurements.

"The coming nanometer age can, therefore, also be called the age of interdisciplinary." – Heinrich Rohrer

4.1 *Introduction*

Noble metal nanoparticles has generated a significant amount of interest in the last few decades, especially in the plasmonics research domain. This is mainly because of the unique surface plasmon resonance effect of noble metals resulting from their wavelength dependent dielectric properties, that give rise to a strongly enhanced near-electric field localized at the metal-dielectric interface[68,142]. The intense near-electric fields are the primary reason why plasmonic metal nanoparticles of Ag, Au and Pt etc. find wide application in multiple fields of research in diagnostic and optical applications such as biophotonics[143–146], photocatalysis[77,124,147], photovoltaics[103,148–150] and surface enhanced Raman spectroscopy (SERS)[151–156]. Moreover, the scope of application with respect to SERS alone is so vast, of which some of the important domains range from imaging of numerous chemical and biological molecules to single molecule detection[110,157–159]. The plasmonic design of hot spots is of major importance in SERS[160–162], as controlling the shape, size and spacing of these noble metal nanoparticles through colloidal self-assembly, sputtering and nanolithographic techniques has boosted the usage of the noble metal nanoparticles in such systems[67,163–165]. Among the noble metals, which possess these unique dielectric properties, silver and gold nanoparticles are highly preferred in SERS application where the electromagnetic enhancement plays a critical role [160,163,166,167]. This is because silver has a higher near-field enhancement factor compared to other plasmonic metals and silver is also economically more favorable. However, the main drawback associated with silver nanoparticles is the lack of long-term stability and formation of a diffuse silver oxide layer, which reduces the electromagnetic enhancement and has a detrimental effect on SERS[126,168]. On the other hand, gold nanoparticles even though on the higher side with respect to cost factor, are highly stable and provide a conducive environment to modify the surface with other ligands depending on the application. Therefore, a tremendous amount of research is being done on modifying gold nanoparticle surfaces and bottom-up approaches to synthesize highly tunable gold nanostructures for SERS applications.

Different kinds of nanoparticle systems with a core-shell structures consisting of metal oxides, carbon and carbon based ligands, graphene or capping agents are also being explored to create a new generation of plasmonic materials for hotspot applications[117,151,152,163,169–171]. Nevertheless, these methods come with a caveat of shielding the intense electric fields at the near vicinity of nanoparticle since these shells commonly range from a couple of nanometers to almost the size of the core particle itself or even larger. For plasmonic applications such as SERS in which electromagnetic enhancement is crucial, this concentrated near-electric field must be available for adsorbed probe molecules to achieve a strong enhancement in the spectroscopic signal. In the second chapter[95,113], a simple yet versatile method to synthesize Ag@polymer core@shell nanospheres using the Layer-by-Layer (LbL) technique for small sized silver nanospheres (< 25nm dia.) was presented, by building an ultrathin polymer shell. The degree of freedom to control the thickness of the protective polymer shell at sub-nanometer level per layer gives the freedom to regulate the localized near-electric field available at the surface of the core shell nanoparticle. In this chapter, the LbL method was used to build polyelectrolyte layers around gold and silver nanoparticles to reduce the near-electric field available at the surface and the theoretical near-electric field estimations were quantified using surface enhanced Raman spectroscopy.

Raman experiments were performed by preparing SERS substrates using stock silver and gold nanoparticles and polyelectrolyte encapsulated silver and gold core-shell nanospheres. Rhodamine 6G was used as the Raman probe dye molecule. In addition, the ultrathin polymer shell was shown to be insulating thus inhibiting the charge transfer effect that sometimes comes into play depending on the selectivity of the probe molecule adsorption to the surface of nanoparticles. Therefore, charge transfer as a contributing factor in the estimation of enhancement could be ruled out. So the changes in the SERS enhancement in such systems could only be effected solely because of changes in the near-electric field. Consequently, it was demonstrated that the loss of signal enhancement in SERS with increasing inter-particle distance is a direct

result of decreasing electromagnetic enhancement. This was supported by the theoretical near-field simulations performed in COMSOL Multiphysics. These results provide a good estimate of the effective distance from the nanoparticle surface and the vicinity in which the enhanced near-electric fields are active for silver and gold nanoparticles.

4.2 *Experimental methods*

4.2.1 Synthesis of silver@polymer core@shell nanoparticles

The preparation of silver-polymer core-shell nanoparticles was performed as reported in second chapter chapter[172]. In brief 12 mL of the as prepared silver colloidal solution[122], which was pre centrifuged to remove excess stabilizing agents and redispersed in Milli-Q water, was added dropwise to 6 mL of 5 g/L PAH (polyallylamine hydrochloride, MW 17.5 KDa Sigma-Aldrich) solution under vigorous stirring in a glass vial. The stirring was continued at room temperature for 20 minutes in dark and the colloidal solution was centrifuged in 1.5 mL Eppendorf tubes to remove the excess polyelectrolyte. The clear supernatant was discarded and the dark-brownish gel-like pellet was redispersed in Milli-Q water. The centrifuge process was repeated one more time as a washing step and the final redispersion in Milli-Q water was adapted to obtain 12 mL of colloid. A small aliquot of this PAH coated silver colloid sample was stored for characterization purposes and labelled as Ag_L1. The deposition of the second polyelectrolyte layer i.e. polyanion of 10 g/L PAA (polyacrylic acid, MW 2 KDa Sigma-Aldrich) was continued using same procedure as described above and the aliquot is labelled as Ag_L2. The deposition of one alternate layer each of PAH and PAA is called a bilayer, and this cycle was continued until four bilayers are deposited i.e., Ag/(PAH/PAA)$_4$, resulting in eight-layered polymer shell in total. The aliquots stored after each layer deposition are labelled as Ag_LX, where X represents the layer number; for example aliquots after 4 and 8 layer depositions are labelled as Ag_L4 and Ag_L8 respectively; whereas bare silver nanoparticles are labelled as Ag_L0.

4.2.2 Synthesis of gold@polymer core@shell nanoparticles

Gold nanoparticles were synthesized as per the well-known Turkevich method[173,174]. In a typical procedure 100 mL of 0.01 wt.% $HAuCl_4.3H_2O$ solution (10 mg in 100mL) was brought to rolling boil in a round bottom flask and 3.5 mL of 1 wt.% trisodium citrate solution (500 mg in 50 mL) was rapidly injected. The solution color changes from light violet to deep red over a period of 5 minutes, and the solution was further boiled for 30 min and immediately cooled down to room temperature. The preparation of gold-polymer core-shell nanoparticles was performed as reported in literature[93,113]. Positively charged polyelectrolyte i.e, poly(allylamine) hydrochloride (PAH, 5 g/L 17.5 KDa, Sigma Aldrich) and negatively charged polyelectrolyte i.e., poly(styrene sulfonate) sodium salt (PSS, 5 g/L MW 15 KDa Polymer Standard Services GmbH) solutions were prepared in Milli-Q water. 12 mL of the as prepared gold colloidal solution, which was pre centrifuged to remove excess stabilizing citrate and redispersed in Milli-Q water, was added dropwise to 6 mL of 5 g/L PAH (polyallylamine hydrochloride, MW 17.5 KDa Sigma-Aldrich) solution under vigorous stirring in a glass vial. The stirring was continued at room temperature for 20 minutes in dark and the colloidal solution was centrifuged in 1.5 mL Eppendorf tubes to remove the excess polyelectrolyte. The clear supernatant was discarded and the dark-reddish gel-like pellet was redispersed in Milli-Q water. The centrifuge process was repeated one more time as a washing step and the final redispersion in Milli-Q water was adapted to obtain 12 mL of colloid. A small aliquot of this PAH coated gold colloid sample was stored for characterization purposes and labelled as Au_L1. The deposition of the second polyelectrolyte layer i.e. polyanion of 5 g/L PSS poly(styrene sulfonate) sodium salt was continued using same procedure as described above and the aliquot is labelled as Au_L2. The deposition of one alternate layer each of PAH and PSS is called a bilayer, and this cycle was continued until six bilayers are deposited i.e., $Au/(PAH/PAA)_6$, resulting in 12 layered polymer shell in total. The aliquots stored after each layer deposition are labelled as Au_LX, where X represents the layer number; for example aliquots after 4, 8 and 12 layers are labelled as Au_L4, Au_L8 and Au_L12 respectively.

4.2.3 Surface enhanced Raman spectroscopy (SERS)

Rhodamine 6G (Sigma Aldrich, Fluorescence bioreagent) dye was used as the Raman probe molecule for SERS measurements and all the measurements were done using glass substrates. The substrates were cleaned in acidic piranha solution (1:3 by volume of concentrated H_2O_2:H_2SO_4) followed by thoroughly rinsing in Milli-Q water. The cleaned glass substrates were dried in a nitrogen stream and immersed in a 30% methanolic solution of APTES, (3-Aminopropyl)triethoxysilane, for at least 12 hours. The substrates were rinsed with methanol and dried in nitrogen stream followed by drying at 100 °C for 30 min. These substrates were prepared for SERS measurements by dropcasting a mixture of known concentration of R6G, 10^{-4} M (10 µL in case of silver and 20 µL in the case gold colloidal solutions) and silver/gold nanoparticles or silver/gold-polymer core-shell nanoparticles. All the samples were allowed to dry in a desiccator for one full day before measurement. All the samples with bare silver/gold and silver/gold-polymer core-shell nanoparticles were adjusted to same concentration by dilution and 1 mL of all the solutions were concentrated to within 40 µL by centrifugation before addition of the dye solution. With a colloidal concentration of $4x10^{11}$ NPs/mL for silver colloid and $8x10^{11}$ NPs/mL for gold colloid, a rough estimation could be made that around 1500 R6G molecules per nanoparticle are present in the concentrated microliter sample drop. A reference neat R6G Raman substrate is prepared by dropcasting 50 µL of 10^{-2} M pure R6G dye solution. Raman spectra were recorded multiple times at different locations for each samples and the calculation of enhancement factors

4.2.4 Characterization

Spectroscopy measurements were performed with a Shimadzu 2501 spectrophotometer in a UV-cuvette of 10 mm path length to locate the SPR peak. Scans were performed in the spectral range of 300-700 nm with a resolution of 0.2 nm and an average of three measurements was taken. A FEI Tecnai Transmission Electron Microscope (TEM) operated at 200 kV was used to visualize the core-shell structure of nanoparticles. In a typical procedure 20 µL of the colloidal solution was absorbed

during 5 min on a quantifoil copper grid coated with a 3.19 nm carbon film. All the Raman measurements were done using a HORIBA XploRA PLUS Raman microscope under the same conditions. A 532 nm diode-pumped solid-state (DPSS) laser with a power of 25 mW was used for excitation and all the spectra were collected with an accumulation time of 20 s. For the nanoscopic measurements using conductive atomic force microscopy (C-AFM), dilute colloidal solution of silver-polymer core-shell nanoparticles were dropcasted on a substrate pre-coated with gold, in order to attain monolayer coverage. Substrates were attached to a stainless steel sample plate using conductive carbon tape. The sample was loaded in an Omicron VT XA ultra-high vacuum (UHV) AFM, which operates at a base pressure of 10^{-10} mbar. Durable B-doped full diamond tips (FDT) were used for optimum electrical contact, reproducibility and suitable tip resistance.

4.2.5 Near-Electric field simulations using COMSOL Multiphysics®

3D models of bare silver/gold nanospheres, silver/gold-polymer core-shell nanospheres with varying polymer shell thickness were built in the wave optics physics in COMSOL Multiphysics (ver. 5.3). A plane wave polarized in the Z-axis direction and propagating along the X-axis direction was solved for the scattered field in a wavelength domain study. COMSOL has inbuilt wavelength dependent refractive index data for silver and gold in its material database, adapted from Johnson and Christy[132], whereas for the polyelectrolyte layers a refractive index of 1.48 was taken from literature[136]. The incident light wavelength is the same as the as the excitation laser wavelength of Raman microscope used in the experiments i.e. 532 nm. Raman enhancement factors were calculated by fourth power of the ratio of near-electric field to in the incident electric field. Since an incident electric field intensity E_0 of 1 [V/m] was used in all the simulations, the enhancement factors becomes the fourth power of point electric field. Detailed information regarding the finite element modeling was previously discussed in chapter 3.

4.3 *Results and discussions*

4.3.1 LbL synthesis of silver@polymer core@shell nanoparticles

Silver-polymer core shell nanoparticles were prepared by sequential cycles of adsorption and washing of alternately charged polyelectrolytes. The alternate deposition of polycation and polyanion chains was continued until the desired number of layers was obtained which results in the encapsulation of the silver core by an ultra-thin polymer shell. UV-vis absorption spectra of the core-shell nanoparticles were recorded after each deposition step as shown in Figure 4.1a. The decrease in intensity corresponds to loss of nanoparticles during the multiple cycles of washing and centrifuging. A red shift of the plasmon peak with increasing number of adsorbed layers can be observed in Figure 4.1b, which is an indication of the gradual increase in particle size due to an increase in encapsulating polymer shell thickness as more LbL layers are added. An in-depth discussion was already undertaken in the second chapter regarding the synthesis of silver@polymer core@shell nanoaprticles.

The TEM images in Figure 4.2, indicate a gradual increase in shell thickness, with no shell for the bare silver nanoparticles (Figure 4.2a), and formation of core-shell nanospheres Ag_L4 (Figure 4.2b and 4.2c) and Ag_L8 (Figure 4.2d) encapsulated by a thin shell of thickness 1.7 nm and 2.7 nm, respectively. The TEM images in Figure 4.2b, 4.2d represent the pattern in which the core-shell nanoparticles dry on a substrate. Even though the core-shell nanoparticles seem to be aggregated when dried, the spacing between adjacent particles is controlled by the polymer layer shell thickness. Whereas for bare silver nanoparticles this kind of spacing is not present and the nanoparticles aggregate immediately after the addition into the Raman probe molecule solution.

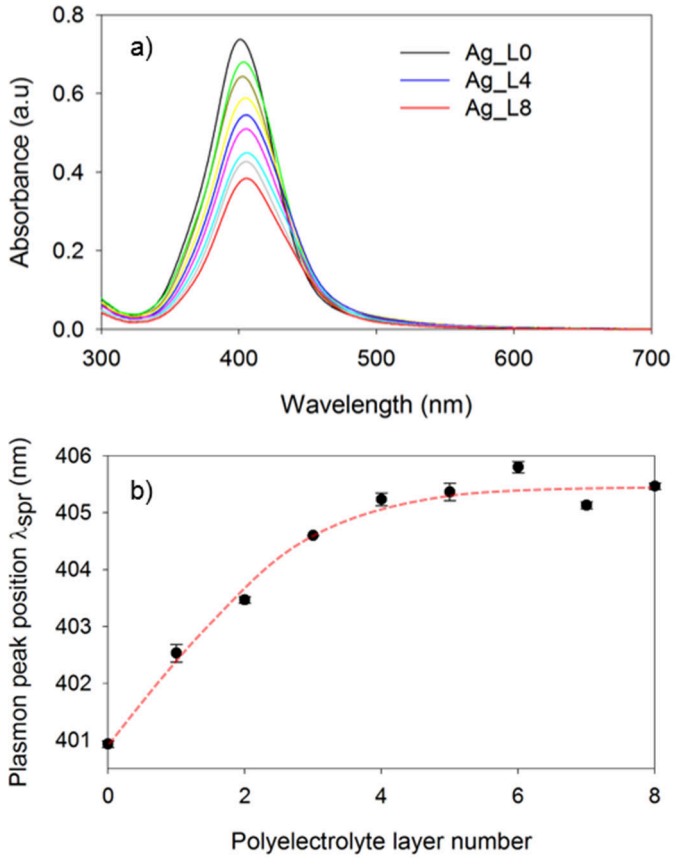

Figure 4.1. a) UV-vis absorption spectra and b) surface plasmon peak position of silver core-shell nanoparticles as a function of the number of adsorbed polyelectrolyte layers. The dotted red curve is a trend line of the shift in plasmon peak position.

4.3.2 LbL synthesis of gold@polymer core@shell nanoparticles

The synthesis of gold-poymer core-shell nanoparticles using alternatively charged polyelectrolytes i.e., polycation PAH and polyanion PSS was performed as explained in the experimental section. After the deposition of each layer of polyelectrolyte, UV-vis spectra were recorded as shown in Figure 4.3a. The slight red shift in the surface plasmon resonance peak position is clearly observed with the increasing number of polyelectrolyte layers encapsulating the gold nanoparticle. The red shift in plasmon peak position is plotted as a function of number of polyelectrolyte layers deposited in Figure 4.3b and the trend is displayed by the red dotted line. In Figure 4.3a, the drop in the intensity of absorption is because of loss of nanoparticles

during the multiple cycles of centrifuge in which the around 10-15% of nanoparticles are lost in each stage. The amount of nanoparticles is a function of intensity of absorbance or optical density and are directly related as per the Beer-Lambert's law. So a drop in absorbance was considered as loss of nanoparticles because the aliquots were not diluted for spectrophotometric measurements and care was taken during the redispersion process to have same volume of colloidal solution during the beginning of LbL process. The percentage recovery of nanoparticles and the position of surface plasmon peak as a function of polyelectrolyte numbers deposited is shown in Table 4.1.

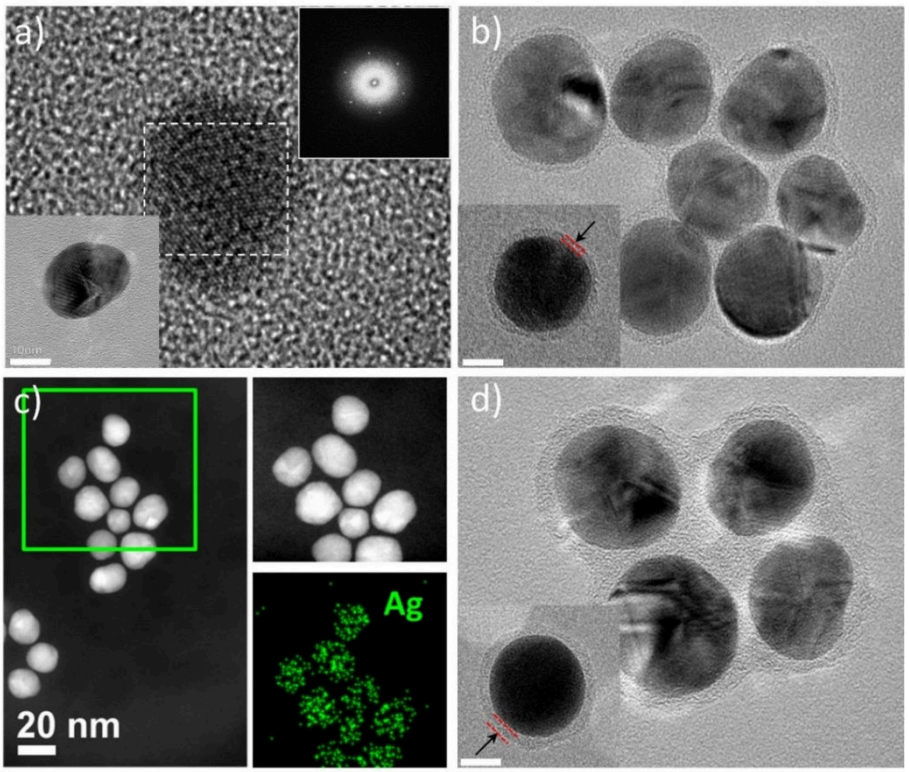

Figure 4.2. a) HR-TEM image of silver nanoparticle with SAED pattern of silver in the top right corner, b) BF-TEM images of Ag_L4: four layered core-shell nanoparticle with a shell thickness of 1.7 ± 0.4 nm, c) HAADF-STEM image of Ag_L4 core-shell nanoparticle clusters with EDX map, d) Ag_L8: eight layered core-shell nanoparticle with a shell thickness of 2.7 ± 0.6 nm. High resolution BF-TEM images in the insets are isolated single core-shell nanoparticles with a scale bar corresponding to 10 nm in a, b and d.

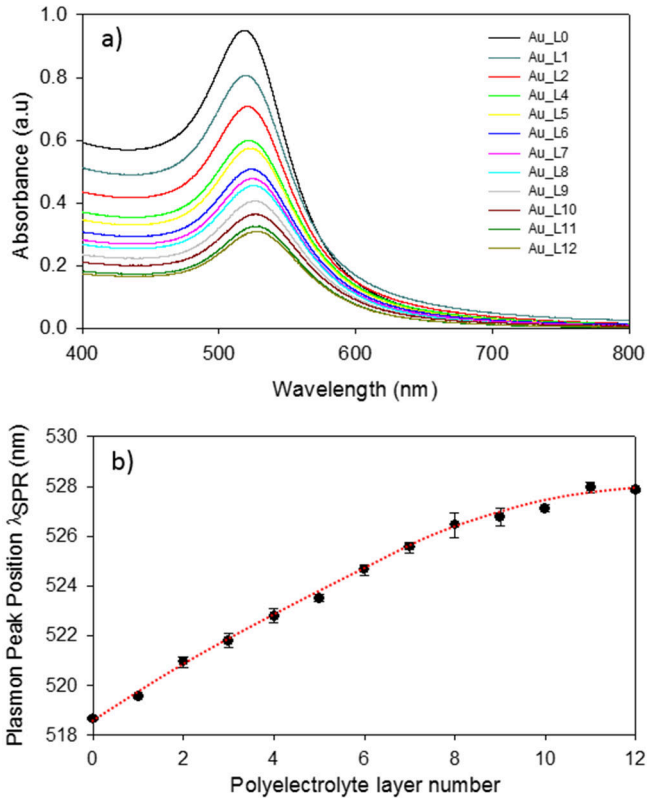

Figure 4.3. a) UV-vis absorption spectra and b) surface plasmon peak position of gold core-shell nanoparticles as a function of the number of adsorbed polyelectrolyte layers. The dotted red curve is a trend line of the shift in plasmon peak position.

Sample label	Layer #	λ_{SPR} (nm)	Abs.	% Recovery of NPs	
				per L0	per layer
Au_L0	0	518.7	0.950	-	-
Au_L1	1	519.6	0.807	85	85
Au_L2	2	521.0	0.707	74	88
Au_L3	3	521.8	0.599	63	85
Au_L4	4	522.8	0.574	60	96
Au_L5	5	523.5	0.508	53	89
Au_L6	6	524.7	0.477	50	94
Au_L7	7	525.6	0.455	48	95
Au_L8	8	526.5	0.406	43	89
Au_L9	9	526.8	0.364	38	90
Au_L10	10	527.1	0.325	34	89
Au_L11	11	528.0	0.309	33	95
Au_L12	12	527.9	0.279	29	90

Table 4.1. Plasmon peak position and percentage recovery of gold nanoparticles as a function of polyelectrolyte layer number during the LbL synthesis of gold-polymer core-shell nanoparticles.

The TEM images of the gold-polymer core-shell nanoparticles, shown in Figure 4.4, also reveal that with the increase in number of layers encapsulating the gold nanoparticle, the shell thickness is also increased. The average diameter of the gold nanoparticle was taken as 17 nm from multiple measurements of different nanoparticles using imageJ program. The shell thickness for a four layered polyelectrolyte shell i.e., Au_L4 is 1.7 ± 0.5 nm, eight layered polyelectrolyte shell i.e., Au_L8 is 2.1 ± 0.6 nm and twelve layered polyelectrolyte shell i.e., Au_L12 is 3.2 ± 0.8 nm. The TEM images also show increase in the inter-particle distance for a trimer nanoparticle system in Figures 4.4b and 4.4c as the shell thickness is increased from Au_L4 to Au_L8 Au@polymer core@shell nanoparticles. This also proves that the polymer encapsulates individual nanoparticles, and during the drying process of TEM sample preparation, the individual core-shell nanoparticles coalesce together forming dimer/trimer nanoclusters.

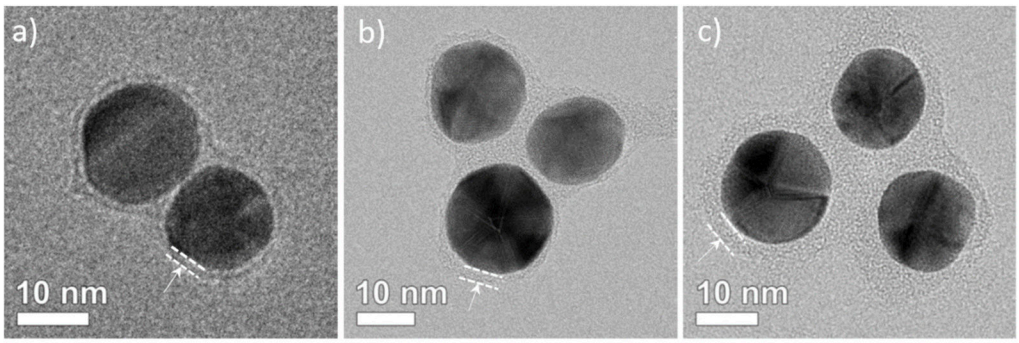

Figure 4.4. a) BF-TEM images of gold-polymer core-shell nanoparticles with the corresponding shell thickness distributions. a) BF-TEM images of Au_L4: four layered core-shell nanoparticle with a shell thickness of 1.7 ± 0.5 nm, b) Au_L8: eight layered core-shell nanoparticle with a shell thickness of 2.1 ± 0.6 nm, and c) Au_L12: twelve layered core-shell nanoparticle with a shell thickness of 3.2 ± 0.8 nm. The white dotted line with arrow indicates the shell thickness for each gold-polymer core nanoparticle

4.3.3 Surface enhanced Raman spectroscopy (SERS)

As discussed earlier, for plasmonic nanomaterials like silver and gold nanoparticles, enhanced near-fields are the main asset for plasmonic applications such as SERS and plasmon enhanced photocatalysis. Therefore, it is important to study how the shell affects these near-field properties. In addition, another main scope of this work is to find out the distance or vicinity from the surface of the nanosphere to which

the enhanced near-electric field is confined. For this specific purpose, SERS was used as an experimental tool to quantify the distance dependency of near-field from the surface of silver and gold nanoparticles. The resulting SERS enhancement factors were analyzed by applying polymer shells of varying thicknesses as an interface spacer material between the nanoparticles to adjust the near-field localization of hot spots for silver and gold plasmonic nanoparticles. In other words, by building polymer shells with high control over the shell thickness, the nanogap between two adjacent silver/gold cores could be tuned and the resulting hot spot effect can be regulated. The experimental SERS enhancement factors were corroborated with near-electric field simulations and theoretically estimated SERS enhancement factor using COMSOL Multiphysics®. For the ease of simulations and calculation efforts, all the nanoparticles and core-shell nanoparticles were assumed to be of spherical shape. The results for silver and gold SERS studies are discussed separately in the following sections to maintain a clear distinction between the two plasmonic nanoparticle systems.

4.3.3.1 Calculation of SERS enhancement factors

SERS substrates were prepared by dropcasting a mixture of R6G dye molecules with silver and gold nanoparticles. In this mixture a ratio of 1500 R6G dye molecules per nanoparticle is maintained by mixing 10 µL (V_{surf}) of 10^{-4} M (C_{surf}) R6G solution with 1 ml of colloidal silver or silver-polymer core-shell nanoparticle solution ($4x10^{11}$ NPs/mL, concentrated to 40 µL from a volume of 1mL by centrifuge). Similar ratio was maintained in case of gold colloidal nanoparticles (8×10^{11} NPs/mL, concentrated to 30 µL from a volume of 1 mL by centrifuge) by mixing with 20 µL (V_{surf}) of 10^{-4} M (C_{surf}) R6G solution. At these concentrations, complete coverage of nanoparticle surface is possible by maintaining an excess of R6G molecules and could be estimated with respect to the surface area of molecules to the nanoparticle. The size of R6G molecule is taken from literature[175]. Also for silver-polymer core-shell and gold-polymer core-shell nanoparticles, the shell thickness of the thickest shell samples i.e. Ag_L8 and Au_L12 in case of silver and gold respectively, was taken into account for surface area

calculations as shown below. Eventually it could be estimated that the number of R6G molecules is always in excess, even in the case of core-shell nanoparticles.

Surface area of 1500 R6G molecules = $1500 \times 1.1 \times 1.6\ nm^2 = 2640\ nm^2$

Surface area of Ag NP = $4\pi \times 10 \times 10\ nm^2 = 1256\ nm^2$

Surface area of Au NP = $4\pi \times 8.5 \times 8.5\ nm^2 = 908\ nm^2$

Surface area of Ag-polymer core-shell NP i.e., Ag_L8

$$= 4\pi \times 12.7 \times 12.7\ nm^2 = 2026\ nm^2$$

Surface area of Au-polymer core-shell NP i.e., Au_L12

$$= 4\pi \times 11.7 \times 11.7\ nm^2 = 1720\ nm^2$$

For neat R6G substrate, 50 µL (V_{norm}) of 10^{-2} M (C_{norm}) was dropcasted for normal Raman measurements. The enhancement factor (EF) could be calculated as:

$$EF = \frac{I_{surf} N_{norm}}{I_{norm} N_{surf}}$$

Where N_{surf} , N_{norm} are the number of molecules probed in SERS and neat R6G substrates respectively and I_{surf}, I_{norm} are the corresponding SERS and normal Raman intensities. The R6G molecules mixed with silver and gold nanoparticles were dropcasted on cleaned glass substrates as circular spots of approx. 8 mm in diameter for most of the samples with the exception of one sample prepared using Au_L8 gold-polymer core-shell nanoparticles. For the neat R6G solution, the deposition area was around 100 mm^2. For all the calculations shown here, the unit of length is mm.

$$N_{surf} = (V_{surf} \times C_{surf} \times N_A \times coverage\ of\ NPs/deposition\ area) \times laser\ spot\ area$$

The Laser spot diameter = 1.22 λ /NA, where λ is the wavelength of the laser in SERS measurements and NA is the numerical aperture of the microscope objective being used. With a 532 nm laser, and a 0.90/100x objective ((NA=0.9), the theoretical spot diameter will be 721 nm. N_A is Avogadro's number.

In the case of SERS experiments with silver and gold nanoparticles, the variable N_{surf} is calculated as:

$$N_{surf} = (V_{surf} \times 10^{-6} \times 10^{-4} \times 6.023 \times 10^{23}/16 \times \pi) \times \pi \times (721/2 \times 10^{-6})^2$$

The value of V_{surf} is 10 for silver and 20 for gold, as the volume of R6G used in mixing with the nanoparticles are different for gold and silver. The number of dye molecules probed in normal Raman mode for neat R6G substrate i.e., N_{norm}, is the same for both the cases of gold and silver SERS experiments, calculated as below:

$$N_{norm} = (50 \times 10^{-6} \times 10^{-2} \times 6.023 \times 10^{23}/100) \times \pi \times (721/2 \times 10^{-6})^2$$

$$\frac{N_{norm}}{N_{surf}} = \frac{(50 \times 10^{-6} \times 10^{-2} \times 6.023 \times 10^{23}/100) \times \pi \times (721/2 \times 10^{-6})^2}{(10 \times 10^{-6} \times 10^{-4} \times 6.023 \times 10^{23}/16 \times \pi) \times \pi \times (721/2 \times 10^{-6})^2}$$

= 251 (ca.) for silver experiments

$$\frac{N_{norm}}{N_{surf}} = \frac{(50 \times 10^{-6} \times 10^{-2} \times 6.023 \times 10^{23}/100) \times \pi \times (721/2 \times 10^{-6})^2}{(20 \times 10^{-6} \times 10^{-4} \times 6.023 \times 10^{23}/16 \times \pi) \times \pi \times (721/2 \times 10^{-6})^2}$$

= 126 (ca.) for gold SERS experiments

The Raman and SERS intensities were recorded from the spectra, averaged for multiple measurements and the calculated values are shown below in Table 4.2.

Substrate	Avg. shell thickness (nm)	I_{norm}	I_{surf} Avg.	I_{surf} std.dev.	EF Avg.	EF std.dev.
Ag_L0+R6G	0	97.5	4971.4	601.8	12798	1549
Ag_L4+R6G	1.7	97.5	706.6	30.7	1819	79
Ag_L8+R6G	2.7	97.5	96.5	-	248	-
Au_L0+R6G	0	103.9	12815.6	635	15488	767
Au_L4+R6G	1.7	103.9	6769	358	8181	433
Au_L8+R6G	2.1	103.9	4721.3	254	7221	388
Au_L12+R6G	3.2	103.9	2505.1	503	3028	608

Table 4.2. Enhancement factors calculated from experimental Raman spectra

4.3.3.2 Analysis of SERS results using silver nanoparticles

As explained in the experimental section, SERS substrates are prepared using bare silver nanospheres (Ag_L0) and silver-polymer core-shell nanospheres with two different shell thicknesses (Ag_L4, Ag_L8). As seen from Figure 4.5, there is significant difference in the color of the samples, especially between bare silver nanoparticles (L0) and polymer encapsulated silver nanoparticles (L4 and L8). This is because when bare silver nanoparticles are added to rhodamine 6G (R6G) solution, the dye molecules immediately initiate the aggregation of nanoparticles. In the case of L4 and L8 substrates, the polyelectrolyte layer protects the silver nanoparticles and thus inhibit the aggregation of nanoparticles. Nevertheless, the nanoparticles still coalesce to form nanoclusters because of surface charge difference between the R6G molecules and polyelectrolytes. It is important to note that both the surface of bare silver nanoparticle and the outer polyelectrolyte layer for silver-polymer core-shell nanoparticles are negatively charged. Indeed it has been observed that R6G has a preferential adsorption for negatively charged nanoparticles which is optimally required for achieving better enhancements in SERS[176]. Irrespective of the clustering of either bare silver nanoparticles (Ag_L0) or silver-polymer core-shell nanoparticles (Ag_L4/Ag_L8), uniform films with similar coverage on the glass substrate by all nanoparticle systems could be seen in the Raman microscopic images (Figure 4.6). SERS substrates prepared by drying of samples always experience a coffee ring effect where dense layers of particles accumulate along the edge of the ring in the dried film (Figure 4.5b). Therefore, the measurements were performed at multiple locations for all the films to check for consistency in the enhanced signal of the surface enhanced Raman spectroscopy. The Raman spectra were not recorded specifically along the ring and islands of nanoparticles, as it would be difficult to focus the incident Raman laser light.

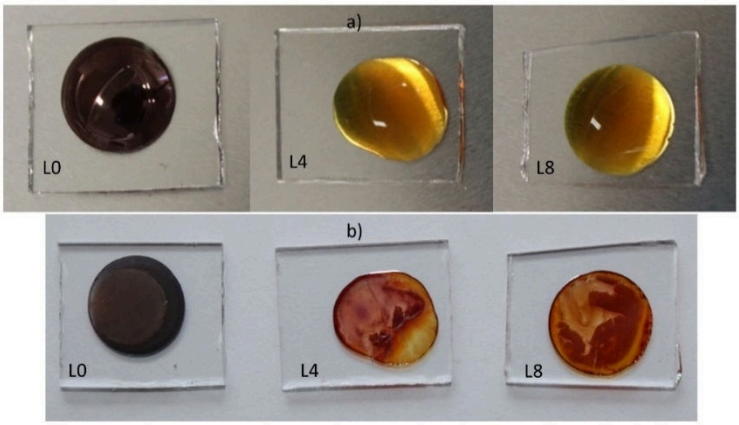

Figure 4.5. Photographic images of Raman substrates a) immediately after mixing the R6G dye with bare Ag NPs (Ag_L0) and silver-polymer core-shell nanoparticles (Ag_L4, Ag_L8) and dropped on glass substrate and b) same Raman substrates after drying in a desiccator for 24 h.

Figure 4.7 shows the SERS measurements of different substrates, and significant enhancements are found for 10^{-4} M R6G in the presence of both bare silver nanospheres (Ag_L0) and silver-polymer core-shell nanospheres with a shell thickness of 1.7 nm (Ag_L4). The Raman intensity for the neat R6G substrate of 0.01 M R6G is amplified five times for better visualization. However, little to no enhancement/signal could be detected for R6G in presence of core-shell nanoparticle with a shell thickness of 2.7 nm (Ag_L8).

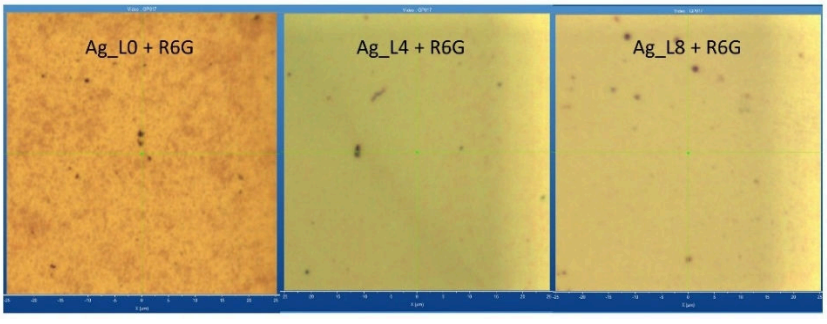

Figure 4.6. Raman microscopic images of the surface of dried SERS substrates prepared by mixing rhodamine 6G molecules with bare silver nanoparticles (Ag_L0) and silver-polymer core-shell nanoparticles (Ag_L4/Ag_L8)

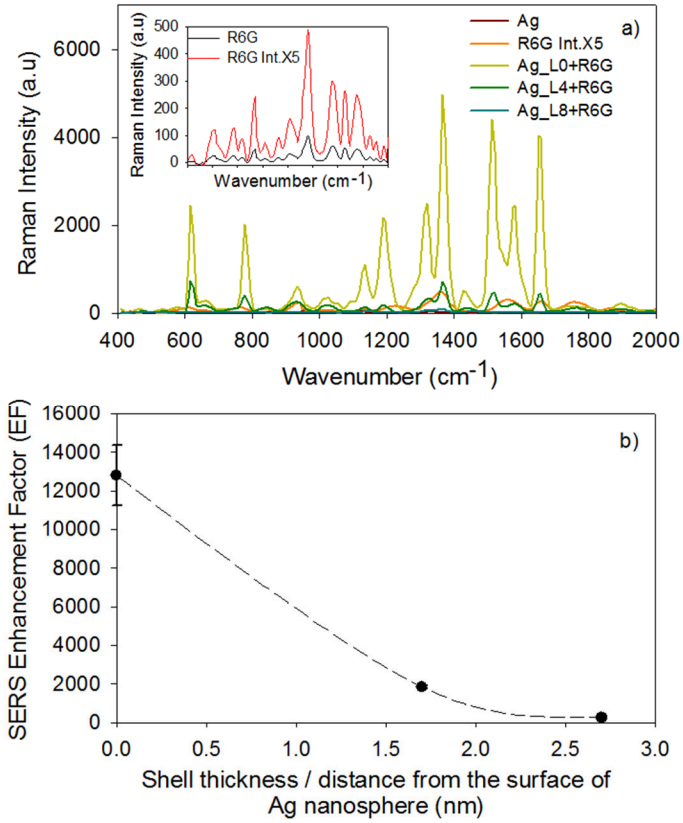

Figure 4.7. a) SERS measurements of pure Ag nanoparticles, 10 mM R6G (intensity amplified 5 times, original and amplified spectra shown in inset), and 0.1 mM R6G with substrates of Ag nanoparticles, Ag_L4 and Ag_L8 core-shell nanoparticles; b) SERS enhancement factor as a function of distance from the silver nanoparticle surface.

The decrease in the experimental SERS enhancement factors (EFs) calculated from the Raman measurements are shown in Figure 4.7b. The SERS enhancement factors are calculated by using the integrated intensity of the 1365 cm^{-1} band of the C-C/C-N stretch of the R6G molecule at which major enhancement in signal is recorded. From the measurements, it can be observed that significantly high enhancement (EF ~ 1.2 x 10^4) is shown by bare silver nanoparticles. And a considerable decline in EF (~ 1.8 x 10^3) is observed when the Ag nanoparticles coated with a shell thickness of 1.7 nm are used. In addition, when the silver nanoparticles are coated with a shell of thickness 2.7 nm or more, insignificant experimental enhancement of the Raman signal is achieved. This trend indicates that the shell thickness i.e., the distance from the surface of the Ag nanoparticles plays a major role in regulating the enhanced near-

electric fields available at the surface of the nanoparticle. In other words tuning the distance between the Raman probe molecules and the surface of the Ag nanospheres was achieved by controlling the thickness of polyelectrolyte layers. Therefore, investigating the effect of shell thickness on the near-field enhancement through field simulations using FEM, will be very helpful. In this work, COMSOL Multiphysics was used to perform the near-field simulations using FEM as described in the previous chapter, and the results are shown in Figure 4.8. The experimental SERS EM enhancement can be a result of near-field generated by either a single nanosphere, or from the hot spots created in-between the nanogap of nanoparticle assemblies. Analyzing the field simulation maps in Figure 4.8a-c and the quantified theoretical EFs (using the $|E/E_0|^4$ estimation[155,156]), the maximum EF is found to be only in the order of 10^2 for single Ag nanoparticles (Figure 4.9) and drops significantly with increasing shell thickness. Such low theoretical EFs do not match the high experimentally observed EF. So, the high EFs achieved from SERS experiments can only be explained by a major contribution from the intense near-fields produced in the hot spots[159,160,177] i.e., the nanogaps between nanoparticles.

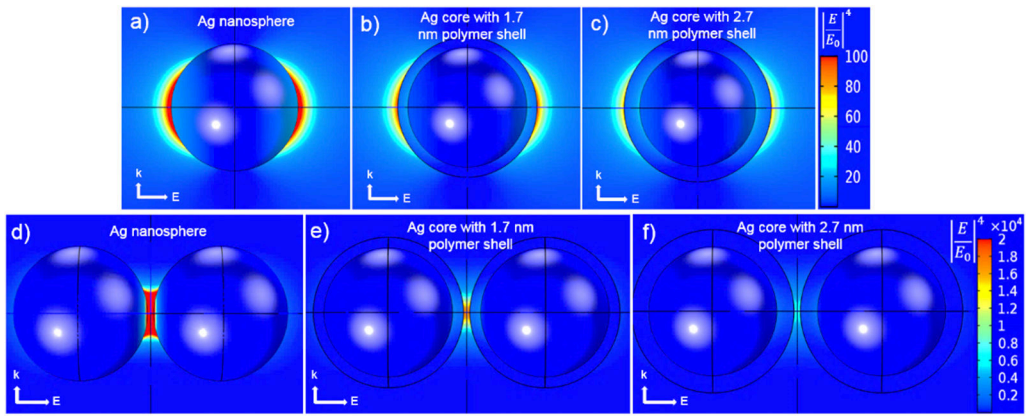

Figure 4.8. a) Near-field simulation maps at the Raman excitation wavelength of 532 nm in air for a) Ag nanosphere and Ag-polymer core-shell nanosphere with a shell thickness of b) 1.7 nm (Ag_L4) and c) 2.7 nm (Ag_L8), and the corresponding dimers of the nanospheres d), e), f). The scale of $|E/E_0|^4$ is normalized at 100 for single nanospheres and $2x10^4$ for dimers respectively for better visualization of the enhanced fields.

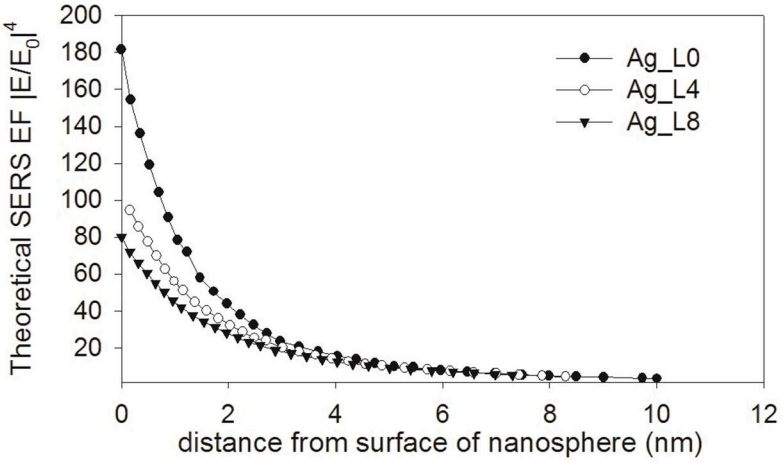

Figure 4.9. Theoretical SERS enhancement factor calculated from near-field simulations as a function of distance from the surface of single nanosphere.

It could be assumed that the hot spot in the nanosphere dimer is of the same order of magnitude as in nanoparticle clusters with the exception of formation of high spatial localization in 3D structures. This assumption is mainly for ease of visualization and analysis of hot spots in field simulation maps. In addition, the mapping distribution and intensity of the near-field in nanogaps of dimers, trimers or tetramers do not vary significantly as evidenced by theoretical simulations (Figure 4.10). The field enhancement maps for the dimer systems, with a nanogap of 1 nm, are shown in Figure 4.8d-f and one can observe that the hot spot intensity decreases for a shell thickness of 1.7 nm, and becomes almost non-existent for shell thickness of 2.7 nm. This is in good agreement with the experimental observation of the SERS EFs which is also observed from Figure 4.11 which shows a comparison between theoretical and experimental SERS EF. Moreover, there is a very good match for the decay ratio of SERS EF with increasing shell thickness. To estimate the theoretical enhancement factor from simulations, a nanogap of two nanometers between two nanoparticles is considered to match the condition when a single R6G dye molecule is adsorbed on each of the adjacent particles providing a spacing layer.

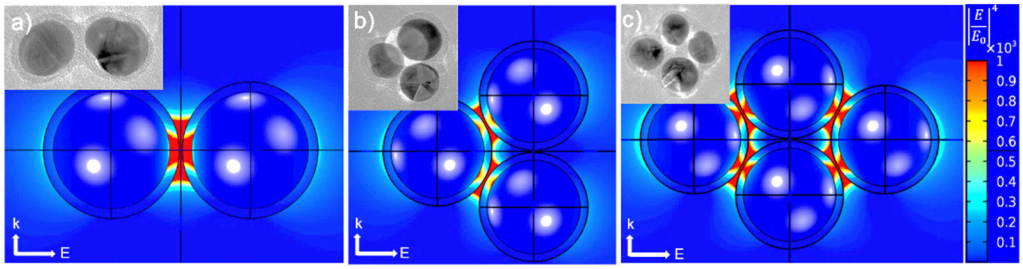

Figure 4.10. Field enhancement maps for a) dimer b) trimer and c) tetramer silver-polymer core-shell nanoparticle clusters with TEM inset images for representation. The color legends are in the scale of $|E/E_0|^4$ representing the magnitude of maximum theoretical SERS EF which are normalized at 1000.

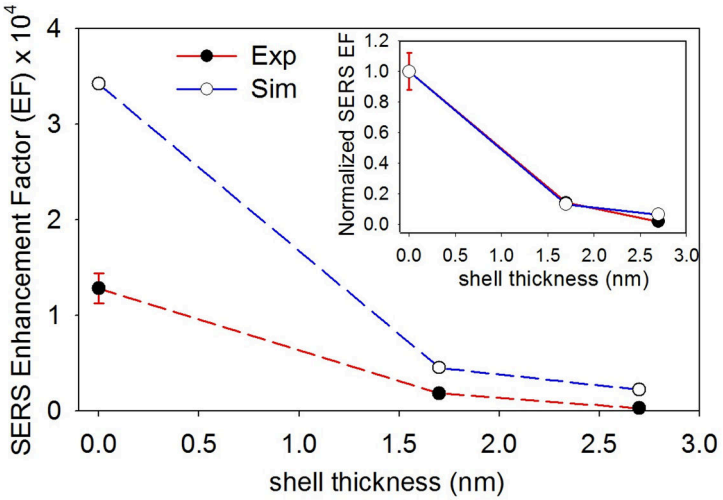

Figure 4.11. Comparison of theoretical and experimental SERS enhancement factors using silver nanoparticles. Inset shows the comparison with a normalized enhancement factor.

4.3.3.3 Analysis of SERS results for gold nanoparticles

The SERS substrate preparation for gold nanoparticles is similar to the methods used for silver nanoparticles. The Raman probe molecule i.e., R6G dye was mixed with a concentrated drop of gold and gold-polymer core-shell colloidal nanoparticles by maintaining a ratio of approximately 1500 R6G molecules per nanoparticle. After drying the substrates in desiccator overnight, the pattern of dried films looked identical to the substrates prepared using silver nanoparticles. As seen from Figure 4.12, a coffee ring drying effect is clearly observed, and the analyses was specifically avoided at the edge of the dried films.

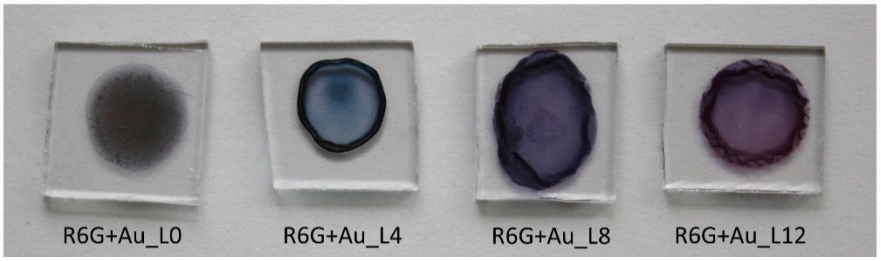

4.12. Photographic images of dried Raman substrates prepared by mixing the probe molecule R6G and bare gold nanoparticles (Au_L0), and polymer encapsulated gold nanoparticles (Au_L4/L8/L12)

The dried Raman substrates also vary in color with respect to different spacing or nanogaps between the nanoparticle clusters. The bare gold nanoparticles are immediately clustered into black-greyish aggregates induced by the addition of R6G molecules. Whereas the polymer encapsulated gold nanoparticles retain the dark red color of the colloid until dried, but slight variation in color could still be observed among the dried cluster films of Au_L4, Au_L8 and Au_L12. This is because of the minute difference in the nanogap within the nanoclusters for each film which could be significant enough to exhibit distinctive optical properties. However, the surface enhanced Raman spectra show a clear trend in the drop in enhancement as the nanogap or distance between the nanoparticles as observed from Figure 4.13. The experimentally calculated enhancement factor for SERS (Figure 4.13b) indicate that very high enhancements in the order of 10^4 could be achieved using bare gold nanoparticles (Ag_L0+R6G). This is because the Raman probe molecules are adsorbed directly on the surface of gold nanoparticle and very intense near-electric fields are generated in the immediate vicinity of the surface of nanoparticles upon excitation of light[151,156]. In the case of substrates prepared with gold-polymer core-shell nanoparticles, the dye molecules adsorb onto the polymer shell outer surface that act as a spacer layer between the gold nanoparticle and dye molecule. This spacer layer or the polymer shell thickness is increased from 1.7 nm to 2.1 nm to 3.2 nm for substrates labeled as Au_L4+R6G, Au_L8+R6G and Au_L12+R6G respectively. From Figure 4.13, it is clear that when the spacer polymer shell thickness is increased from 1.7 to 3.2, the enhancement drops from 8×10^3 to around 3×10^3.

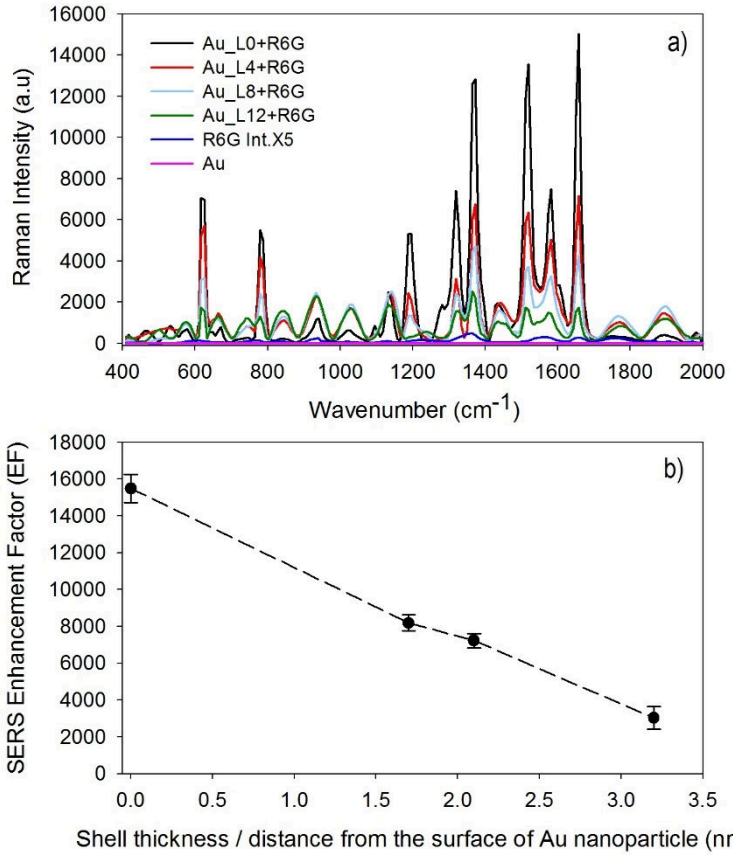

Figure 4.13. a) SERS measurements of pure Au nanoparticles, 10 mM R6G (intensity amplified 5 times), and 0.1 mM R6G with substrates of Au nanoparticles, Au_L4, Au_L8 and Au_L12 core-shell nanoparticles respectively. b) SERS enhancement factor as a function of distance from the gold nanoparticle surface.

The decrease in the intensity of near-electric field available at the surface of polymer shell results in the drop in the enhancement of Raman signal. This is supported by the near-field simulations performed using COMSOL, for gold and gold-polymer core-shell nanoparticle dimer systems as shown in Figure 4.14. The theoretical SERS enhancement factor were estimated from the near-electric field simulations, with the assumption that the hot spots created in a dimer nanoparticle system are similar to nanoparticle clusters as analyzed in Figure 4.10 for silver nanoparticle systems.

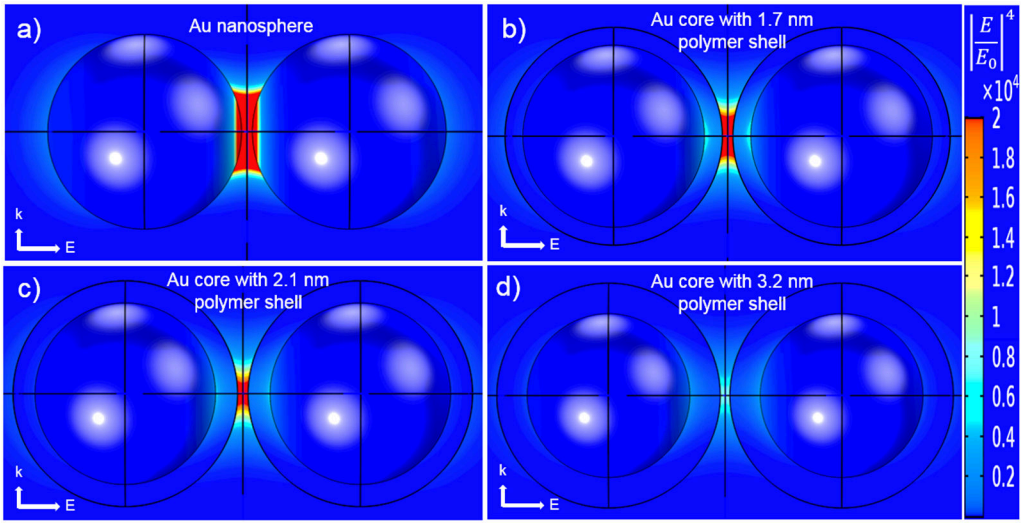

Figure 4.14. Near-field simulation maps at the Raman excitation wavelength of 532 nm in air for dimer systems of a) Au nanosphere and Au-polymer core-shell nanosphere with a shell thickness of b) 1.7 nm (Au_L4), c) 2.1 nm (Au_L8) and d) 3.2 nm (Au_L12). The scale of $|E/E_0|^4$ is normalized at $2x10^4$ for better visualization of the enhanced fields.

The comparison between the experimental enhancement factor and theoretically estimated SERS EF i.e., the fourth power of field enhancement $|E/E_0|^4$[155,156] is shown in Figure 4.15. The absolute value of SERS enhancement factor (EF) seems to be in good agreement with the exception of bare gold nanoparticles. When the SERS EF was normalized with respect to EF of the bare gold nanoparticles, the experimental and simulation enhancement factors seem to differ significantly.

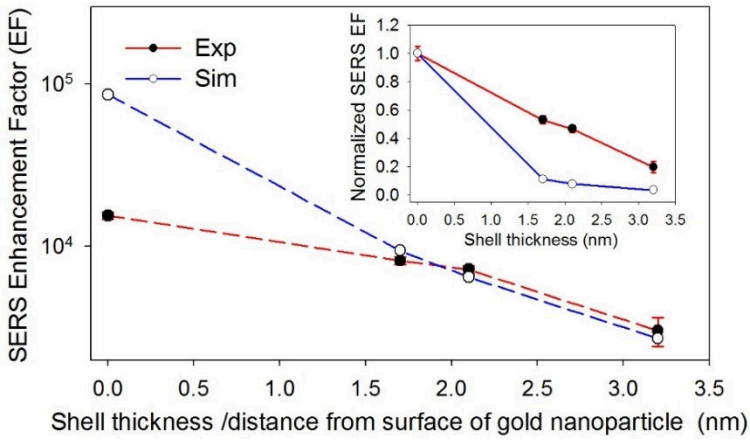

Figure 4.15. Comparison of theoretical and experimental SERS enhancement factors for gold nanoparticles as a function of shell thickness/distance from surface of gold nanoparticle. Inset shows the comparison with a normalized enhancement factor.

However the trend in the drop of EF because of reduction of near-electric field as the shell thickness (which is the also the distance from the surface of gold nanoparticle) is clear from the plots. This provides a good understanding in the decay ratio of near electric field with respect to distance from the surface of nanoparticle.

It is interesting to observe that SERS substrates prepared using gold/gold-polymer core-shell nanoparticles (Figure 4.13) exhibit significantly better enhancement factors compared to silver/silver-polymer core-shell nanoparticles (Figure 4.7). The absolute values were listed in Table 4.2 for better understanding. There are two important reasons behind the better enhancement factors displayed by gold nanoparticle systems. One of the important feature is the overlap of surface plasmon resonance wavelength of plasmonic nanoparticles with the Raman laser wavelength used for excitation of the SERS substrates. In SERS, it is important to match the wavelengths of the incident light source and the surface plasmon resonance of the plasmonic nanoparticles used, to achieve the best possible enhancement of Raman signal. Since the surface plasmon resonance (SPR) wavelength is dependent on the size and shape of plasmon nanoparticle, the SERS EFs are influenced by the physical property parameters of plasmonic nanoparticles. The SPR wavelength of silver and gold nanoparticles are located far apart in the light spectrum depending on their size and shape. An analytical study was performed using FEM in COMSOL, to estimate the theoretical SERS EFs for gold and silver nanoparticle dimer systems in air, assuming an approximate size of 20 nm diameter for the nanoparticles. The resulting theoretical SERS EFs as a function of wavelength are shown in Figure 4.16. It could be observed that the gold dimer nanoparticle system has a better overlap with the laser wavelength used in Raman experiments. The dipolar resonance is a typical property of silver dimer nanoparticles[178,179]. The theoretical SERS EF for gold nanoparticles is at least ten times higher than silver nanoparticles that would corroborate the higher level of EFs achieved, even at a distance of 3.2 nm from the surface of gold nanoparticle. The other reason for the better enhancements achieved by gold nanoparticle systems is that the shape of the as-synthesized gold nanoparticles are not always perfectly spherical. The

TEM analysis of gold-polymer core-shell nanoclusters (Figure 4.17) reveals that there are different shapes in the gold nanoparticle clusters such as triangular prisms, tetrahedrons and rods with rounded corners. The multi-facetted nanoparticles possess higher near-electric field that would result in higher enhancement factors (Figure 4.18), especially the triangular and rod shaped nanoparticles. It is important to note that the theoretical EFs estimated from FEM simulations had an underlying assumption that all nanoparticles are spherical in shape. Therefore, the anisotropic nature of the plasmonic gold nanoparticles would result in divergence in the comparison of theoretical and experimental EFs. In the case of SERS experiments with silver nanoparticles, most of the nanoparticles were spheroid with minor deviations, if not perfectly spherical. Nevertheless, the drop in the SERS EFs with increasing shell thickness i.e., distance from the surface of nanoparticle, could be assigned as a direct consequence of decrease in near-electric field.

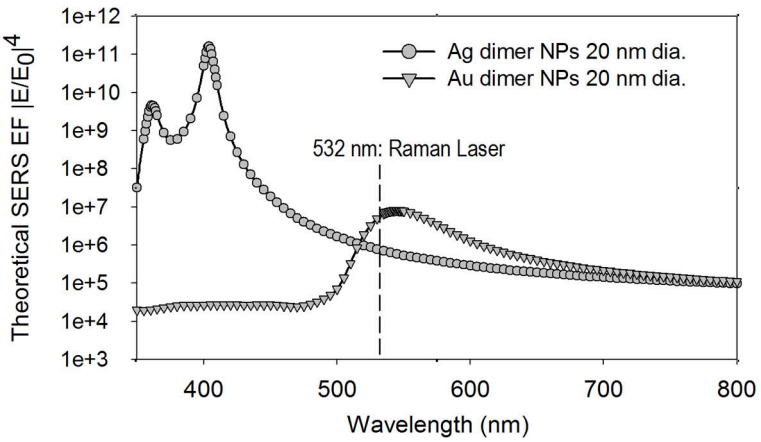

Figure 4.16. Comparison of theoretical SERS EF for gold and silver nanoparticle dimers of size 20 nm in dimeter separated by a gap of one nm.

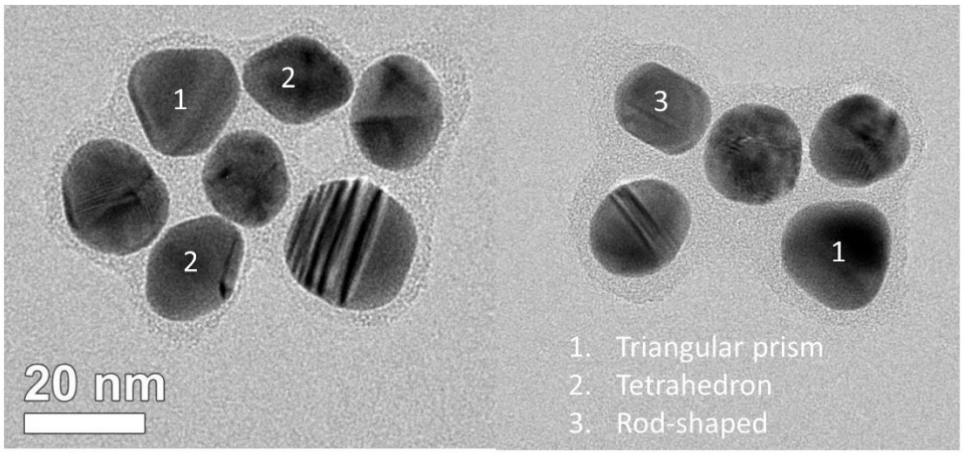

Figure 4.17. TEM images of gold-polymer core-shell nanoparticle clusters analyzed from the same batch of colloidal nanoparticles (Au_L12). The different shapes of the nanoparticles are numbered for better identification.

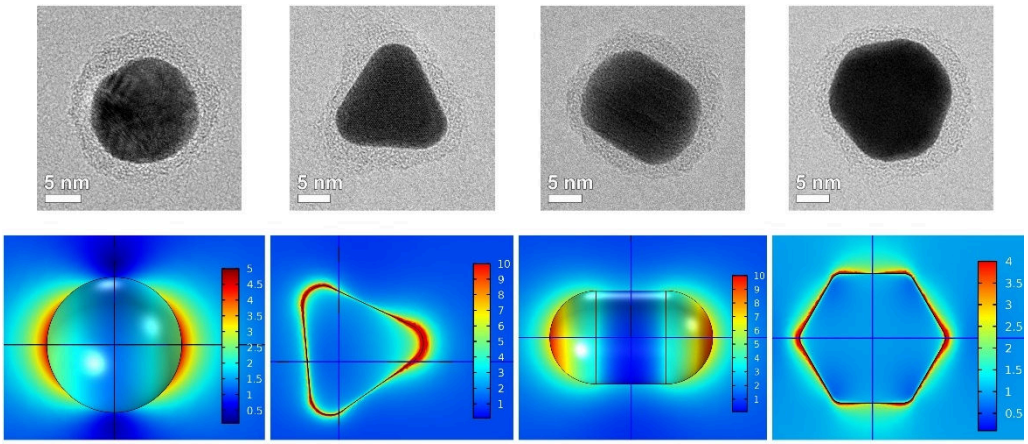

Figure 4.18. Transmission electron micrograph images and the corresponding near-electric distribution maps of different shapes of gold nanoparticles from a single batch of as-synthesized gold colloidal solution. The scale legend represents the normalized electric field $|E/E_0|$ for an incident light wavelength of 532 nm.

4.4 *Distance dependency of near-electric field for silver and gold plasmon nanoparticles*

The SERS analyses using silver and gold nanoparticles provided a more realistic picture that beyond a distance/vicinity of couple of nanometers from the surface of nanoparticle the electromagnetic enhancement becomes negligible. These results are in line with the literature[126,156,180], where it has been reported that within 1-2 nanometers from the surface of plasmonic nanoparticle, the enhancement is radically reduced. There is a possibility that the ultrathin polyelectrolyte layer may be inherently enhancing the Raman signal through chemical enhancement. This is possible when the adsorbed R6G molecule interacting with the polymer chain allows for a quick charge transfer. To investigate this potential contribution, conductive tip atomic force microscopy (C-AFM) measurements were performed to find the charge transfer properties of silver-polymer core-shell nanoparticles. The results for conductive tip AFM measurements of silver-polymer core-shell nanoparticles, are already discussed in second chapter, revealed that the polyelectrolyte bilayer combination of PAH/PAA is insulating. The conductive tip AFM results supported the preliminary IV voltammetry studies that showcased that the polyelectrolyte layer is highly resisting to flow of electrons or charge transfer.

Similar studies were performed on gold@polymer core@shell nanoclusters and the results revealed that the encapsulating polymer shell around gold is also insulating in nature. This measurement rules out chemical enhancement due to charge transfer through the ultrathin polymer shell. This also supports the fundamental theory that near-field or EM enhancement is the major mechanism responsible for SERS in this study, as also established in the literature[151–153,181]. As a final remark it should be noted that due to the size- and shape dependence of SPR on metal nanoparticles like silver and gold, this can and will affect the hot spots and correlated intensity enhancement that can be achieved in SERS[163,165,182]. Additionally, using different polymer materials for the shell (either insulating or conductive) will also have an impact as long as there is a significant change in the refractive index of the polymer

materials used. Nonetheless, the replication of the LbL procedure and resulting parameters of shell thickness and corresponding red-shifts confirm excellent repeatability which was discussed in previous chapter. The corresponding polyelectrolyte combinations to tune the nanogap should therefore be regarded as a more generic approach to fine-tune the near-field localization of plasmonic nanoparticles. Specifically, it can be concluded that the near-electric field boosts the plasmonic hot spot application oriented processes, for example SERS, with a distance dependency limitation of within few nanometers, 2 nm in case of silver and 3 nm in case of gold, from the surface of the nanoparticle.

4.5 *Conclusions*

This study demonstrates how experimental methods in conjunction with theoretical simulations can act as a vital mechanistic tool to understand the plasmonic properties of silver and gold nanoparticles. In this way, the effect of shell thickness on the optical properties of core-shell nanoparticles and nanoparticle assemblies is thoroughly examined. The application of a spacer layer through wet chemical methods such as LbL can be used to effectively engineer the size of the nanogap in-between adjacent particles. This is important, as it is shown that the distance from the particle core greatly affects the near-field and resulting SERS enhancement. Comparison with theoretical FEM field simulations indicates that experimentally obtained enhancement factors in SERS are mainly determined by the enhanced near electric field generated at the hot spot zones in-between particles, of which the nanogap can be regulated through the thickness of the spacer shell layer. It is also important to maintain an overlap of the surface plasmon resonance wavelength of the plasmonic nanoparticles with the light source wavelength for optimal performance of the plasmonic nanoparticle system.

These studies point out that the near-electric field is only active within a few couple of nanometers from the surface of plasmonic nanoparticle. Additionally, these tools and insights will facilitate more straightforward nano-engineering of substrates

for plasmonic applications to target the localized vicinity of field enhancement and make use of hot spot effects of such plasmonic nanoparticles. Moreover, it will help identify and engineer the optimal interparticle distance, customized to a particular plasmonic application.

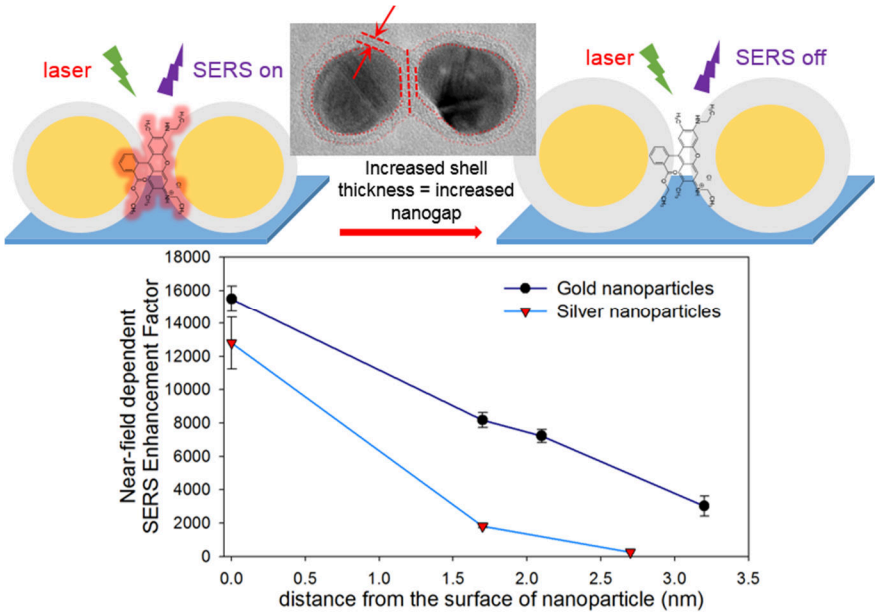

Figure 4.19. Graphical representation of the summary of the chapter.

Chapter 5

Gold plasmon enhanced photocatalysis: investigating the responsible mechanism

Contributions: Nathalie Claes, EMAT, University of Antwerp, for TEM analysis.

Matthias Minjauw and Tareq Ahmad, CoCooN, Gent University, for C-AFM measurements.

A photon checks into a hotel. The bellhop asks, "Can I help you with your luggage?" It replies, "I don't have any. I'm traveling light." – WWW

5.1 *Introduction*

The diverse application of plasmonic gold nanoparticles in multiple fields of research such as photocatalysis[63,74,183–186], sensing and biomedical applications [145,157,187–190] has driven tremendous amount of research. In the field of plasmon-enhanced photocatalysis, extensive research has been done with gold nanoparticles as it has been shown to improve the photocatalytic efficiency[81–83,191–193]. Gold titanium dioxide plasmon enhanced photocatalytic systems are widely reported to have better performance than pristine TiO_2 systems. However, the primary mechanism responsible for the enhancement of TiO_2 photocatalysis in the presence of gold plasmonic nanoparticles is still under debate[77,186,194,195]. This chapter tries to provide an insight onto the important contribution from both the charge transfer and near-field mechanism aspects, from excited plasmonic gold nanoparticles for Au-TiO_2 photocatalytic systems. Different types of Au-TiO_2 plasmonic photocatalytic systems were prepared using polyelectrolyte spacer layers and compared with the pristine reference TiO_2 photocatalytic activity. This was achieved by encapsulating the gold nanoparticle by either an insulating or conductive polymer shell that acts as a separating interface layer between the semiconductor photocatalyst and plasmon metal nanoparticle. With a spacer layer that could be either insulating or conductive, a clear distinction can be made between the charge transfer and near-field induced resonant energy transfer. Additionally the spacer layer thickness can be fine-tuned by changing the polyelectrolyte shell thickness using simple wet chemical methods. By increasing the space layer thickness, the near-field could be suppressed, and by using either insulating or conductive polymer shell one of the mechanism could be ruled out. The suppression of the near-electric field was analyzed by finite element modeling (FEM) simulations using COMSOL Multiphysics®. The accuracy of the near-electric field simulations are already corroborated by surface enhanced Raman spectroscopic (SERS) experimental measurements in the previous chapter. Additionally SERS serves as an experimental support to corroborate the near-field studies to find the distance dependency from the surface of nanoparticle at which near-electric field is active.

Comparison of the photocatalytic activity of all the different systems will provide a definitive idea that could be hypothesized for the enhancement of TiO_2 semiconductor photocatalysis using gold nanoparticles. These studies will provide an understanding on how to make the best use of plasmonic nanostructures to enhance the TiO_2 based photocatalytic systems.

5.2 *Experimental methods*

5.2.1 Synthesis of gold colloidal solution

Gold nanoparticles were synthesized as per the well-known Turkevich method[173,174]. In a typical procedure 100 mL of 0.01 wt.% $HAuCl_4.3H_2O$ solution (10mg in 100mL) was brought to rolling boil in a round bottom flask and 3.5 mL of 1 wt.% trisodium citrate solution (500 mg in 50 mL) was rapidly injected. The solution color changes from light violet to deep red over a period of 5 minutes, and the solution was further boiled for 30 min and immediately cooled down to room temperature.

5.2.2 Synthesis of gold@polymer core@shell nanoparticles

Polymer encapsulated gold nanoparticles were synthesized using the layer-by-layer method as described in chapter 4 and from the literature[95,113]. In brief, pre-centrifuged gold colloidal solution was added dropwise to 6 mL of 5 g/L PAH solution under vigorous stirring in a glass vial. The stirring was continued at room temperature for 20 minutes in dark and centrifuged and washed to remove the excess polyelectrolyte and finally redispersed in Milli-Q water. This was followed by the deposition of the second layer i.e. polyanion PSS (5 g/l) and the cycle was continued until the desired number of layers were obtained. The LbL process was continued until 12 layers of polyelectrolytes were encapsulating the gold core nanoparticle. The aliquots are labeled as per the corresponding layer number for convenience i.e., Au_LX where X is the number of layers.

5.2.3 Synthesis of gold@PANI core@shell nanoparticles

Polyaniline (PANI) encapsulated gold core-shell nanoparticles were synthesized by in-situ polymerization of aniline at the surface of bare gold nanoparticles using the method described in literature[99]. As a first step, 12 mL of gold colloidal nanoparticles were centrifuged to remove the excess stabilizing citrate and concentrated to final volume of around 100 µL. This concentrated drop of gold nanoparticle suspension was added to aqueous mixture of sodium dodecyl sulfonate (SDS, 0.9 mL of 40 mM concentration) and aniline (4.5 mL of 2 mM concentration) under stirring. The stirring was continued for 10 minutes followed by addition of 4.5 mL of 2 mM ammonium persulfate solution. The stirring was stopped and the solution was allowed to incubate at room temperature under dark conditions. Aliquots were removed after a time duration of 30, 90 and 180 minutes, which were centrifuged and redispersed in either 4 mM SDS solution or water as a washing step and remove left over reactants. Spectrographic measurements were performed after allowing the solutions to stand overnight. The three different aliquots are labeled as Au_PANI30, Au_PANI90 and Au_PANI180 for the samples with polymerization time of 30, 90 and 180 minutes respectively. The samples were analyzed with transmission electron microscopy for morphology and shell thickness determination and UV—vis spectroscopy.

5.2.4 Characterization

Spectroscopy measurements were performed with a Shimazdu 2501 spectrophotometer in a UV-cuvette of 10 mm path length to locate the SPR peak. Scans were performed in the spectral range of 300-900 nm with a resolution of 0.2 nm and an average of three measurements was taken. A FEI Tecnai Transmission Electron Microscope (TEM) operated at 200 kV was used to visualize the core-shell structure of nanoparticles. In a typical procedure 20 µL of the colloidal solution was absorbed during 5 min on a quantifoil copper grid coated with a 3.19 nm carbon film. Photometric measurements were performed to determine the gold mass concentration per unit volume in the colloids by appropriate dilution to detection

limits using the Spectroquant® gold test kit. The Current-Voltage (IV) measurements were performed using a potentiostat (Versastat 3, Princeton Applied Research, AMETEK Sci. Inst.). For the nanoscopic measurements using conductive atomic force microscopy (C-AFM), dilute colloidal solution of gold-polymer core-shell nanoparticles were dropcasted on a substrate pre-coated with gold, in order to attain monolayer coverage. Substrates were attached to a stainless steel sample plate using conductive carbon tape. The sample was loaded in an Omicron VT XA ultra-high vacuum (UHV) AFM, which operates at a base pressure of 10^{-10} mbar. Durable B-doped full diamond tips (FDT) were used for optimum electrical contact, reproducibility and suitable tip resistance.

5.2.5 Photocatalytic activity measurements

Photocatalytic measurements were performed by studying the degradation of stearic acid using different photocatalytic systems. The Au-TiO_2 plasmonic photocatalytic systems were prepared by dropcasting 50 µL of 1 wt.% ethanol suspension of commercial TiO_2 (P25, Aeroxide) onto six silicon wafers, which were pre-cleaned in methanol. So around 0.5 mg of the photocatalyst is present on each silicon wafer, which were dried overnight at 90 ^{0}C. Five of these substrates were loaded with gold (Au_L0), polymer encapsulated gold (Au_L4, Au_L12) and PANI encapsulated gold (Au_PANI30, Au_PANI180) nanoparticles. Equal metal loading (0.015 mg) on the substrates were maintained by quantified Spectroquant® measurements i.e., 50 mg/L colloidal solutions were used. The reference substrate that contained the pristine TiO_2 was loaded with equal volume of water to adapt for the enhancement effect of hydroxyl radicals. All the substrates were dried at 90 ^{0}C for 6 hours in an oven. The substrates were then spin coated with 100 µL of the 0.15 wt.% stearic acid solution in chloroform and allowed to dried at 80 °C for 15 minutes. The reference system is labeled as TiO_2_ref in which the samples were prepared by drop casting suspension of pristine TiO_2. Whereas, the Au-TiO_2 plasmonic photocatalytic systems prepared with bare gold nanoparticles, insulating polymer encapsulated gold nanoparticles and conductive polyaniline encapsulated gold nanoparticles are labeled as per the aliquot

of samples used. The designations of the different Au-TiO_2 plasmonic systems are listed in Table 5.1 for ease of understanding. A photographic image of all the samples is shown in Figure 5.1, where the gold loaded samples show a light pink color that is typical of SPR effect of plasmonic gold nanoparticles. The photocatalytic activity of the samples was tested under the visible light by using a green LED light (Figure 5.1). The rate of degradation was compared by measuring the decrease in stearic acid absorbance using an FTIR spectrophotometer (Nicolet 380, Thermo Fisher Sci.).

Type of sample	Shell thickness (nm)	Sample label
TiO_2	-	**TiO_2_ref**
TiO_2 loaded with Au NPs	0 nm	**TiO_2_AuL0**
TiO_2 loaded with Au@polymer core@shell NPs - Au_L4	1.7 ± 0.5 nm	**TiO_2_AuL4**
TiO_2 loaded with Au@polymer core@shell NPs - Au_L12	3.2 ± 0.8 nm	**TiO_2_AuL12**
TiO_2 loaded with Au@PANI core@shell NPs - Au_PANI30	1.4 ± 0.5 nm	**TiO_2_AuPANI30**
TiO_2 loaded with Au@PANI core@shell NPs - Au_PANI180	7.5 ± 1.6 nm	**TiO_2_AuPANI180**

Table 5.1. Different types of Au-TiO_2 plasmonic photocatalytic systems used for photocatalytic tests in this work.

Figure 5.1. Photocatalytic samples and illumination set-up of the substrates under a green LED irradiation with an emission wavelength 515 nm.

5.3 *Results and discussions*

5.3.1 LbL synthesis of gold@polymer core@shell nanoparticles

The layer by layer deposition of alternatively charged polyelectrolytes around the colloidal gold nanoparticles results in the red shift of the SPR peak position. In Figure 5.2a, the shift in SPR peak position is clearly seen in the normalized absorption spectra with the zoomed inset of the SPR peak positions. This magnitude of the red shift is plotted as a function of polyelectrolyte number in Figure 5.2b. The red dotted line displays a trendline in the red shift of SPR peak position as more number of polyelectrolyte layers encapsulate the gold core nanoparticle. A total SPR peak red shift of 9.2 nm is observed after the encapsulation of bare gold nanoparticle (Au_L0) with twelve layers of polyelectrolyte layers (Au_L12).

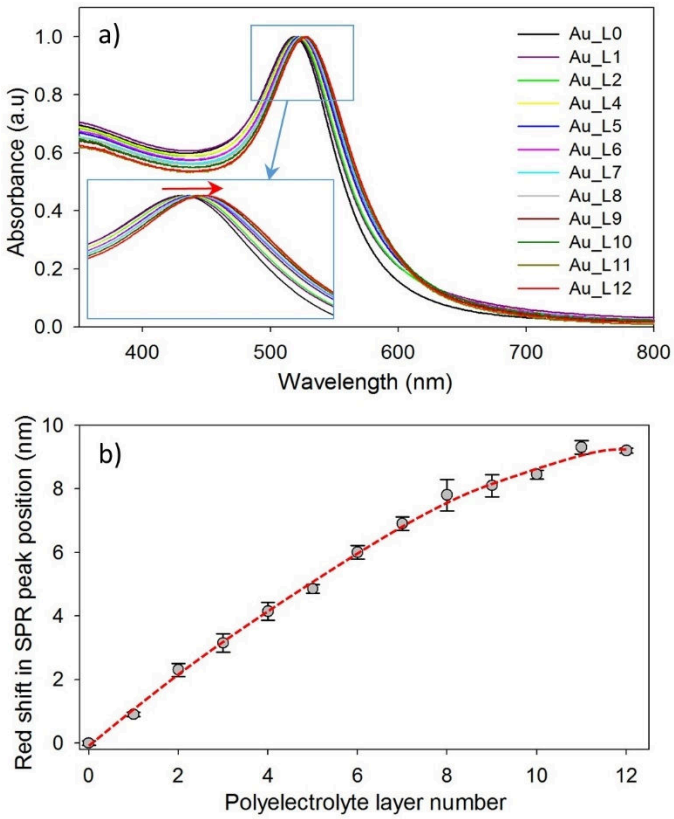

Figure 5.2. a) UV-vis absorption spectra and b) surface plasmon peak position of gold core-shell nanoparticles as a function of the number of adsorbed polyelectrolyte layers. The dotted red curve is a trend line of the red shift in plasmon peak position.

The TEM images (Figure 5.3) show the ultra-thin polyelectrolyte shell build-up with the increase in encapsulating polyelectrolyte layers. The shell thickness for a four layered polyelectrolyte shell i.e., Au_L4 is 1.7 ± 0.5 nm (Figure 5.3a), eight layered polyelectrolyte shell i.e., Au_L8 is 2.1 ± 0.6 nm (Figure 5.3b) and twelve layered polyelectrolyte shell i.e., Au_L12 is 3.2 ± 0.8 nm (Figure 5.3c). The shell thickness was determined by at least 100 measurements of multiple gold-polymer core-shell nanoparticles. The shell thickness distribution is shown at the bottom of the corresponding TEM images of the gold-polymer core-shell nanoparticles. The average particle size of the gold nanoparticles was around 17 nm in diameter, as measured by analysis of multiple nanoparticles using ImageJ program. The particle size distribution of gold nanoparticles is shown in Figure 5.4a and a prediction of relation between the shell thickness and number of polyelectrolytes deposited is shown in Figure 5.4b.

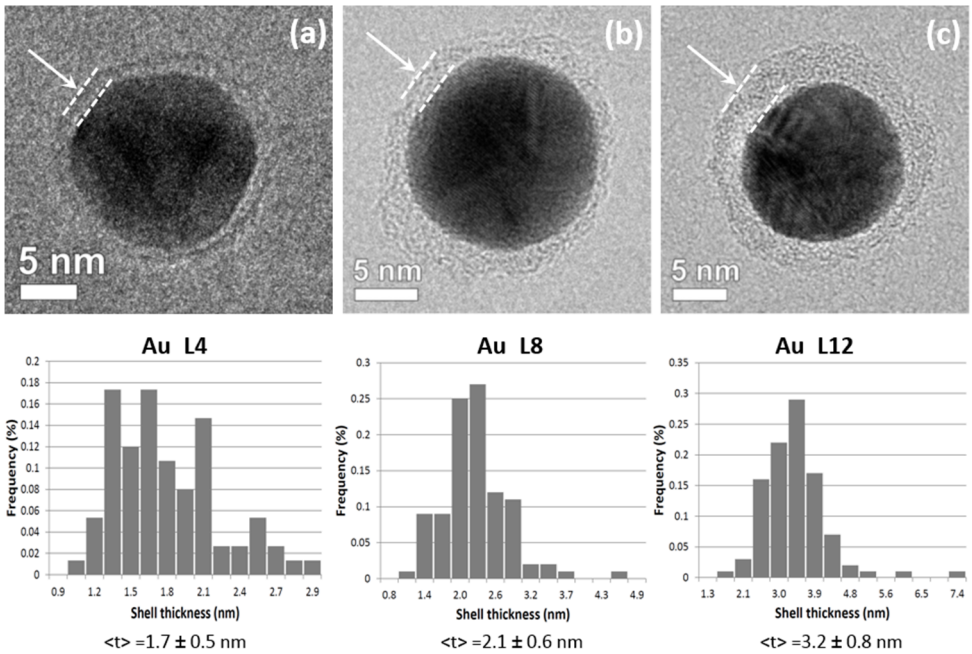

Figure 5.3. TEM images of gold@polymer core@shell nanoparticles and the corresponding mean shell thickness with the distribution for a) four-layered (Au_L4), b) eight-layered (Au_L8) and c) twelve-layered (Au_L12) gold-polymer core-shell nanoparticles.

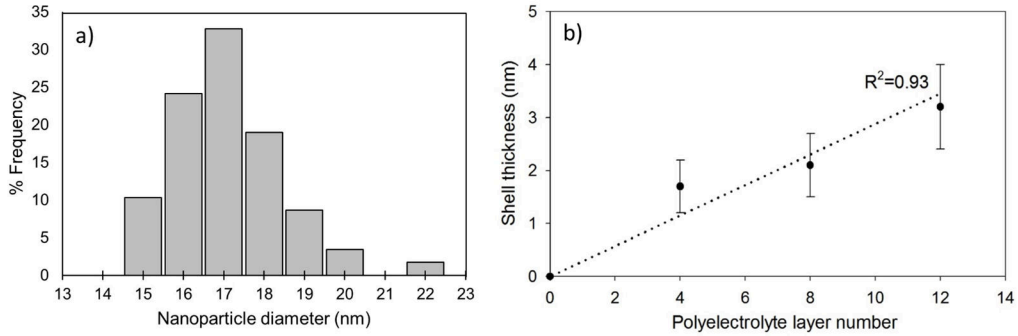

Figure 5.4. a) Gold nanoparticle size distribution (average diameter of 17 nm) from multiple measurements. b) Shell thickness as a function of polyelectrolyte number and a linear fit for gold@polymer core@shell nanoparticles.

5.3.2 Synthesis of gold@PANI core@shell nanoparticles

Gold@PANI core@shell nanoparticles were synthesized by in-situ oxidative polymerization of aniline using acidic ammonium persulfate as the oxidant. The presence of the surfactant (SDS) is important for uniform adsorption of aniline molecules around the nanoparticle surface before the oxidant is added. The pH of the reactant mixture is also crucial for chain initiation and propagation during the polymerization[102]. The polymerization of aniline with ammonium persulfate is a fast reaction and the polymerization ends after one of the reactant is depleted. Therefore, the polymerization begins immediately after the addition of solution of ammonium persulfate to the mixture of SDS, aniline and gold nanoparticles. The UV-vis absorption spectra of the aliquots removed after a polymerization time of 30 (Au_PANI30), 90 (Au_PANI90) and 180 minutes (Au_PANI180) are shown in Figure 5.5a. The spectra were normalized (Abs_{450}=0.5) for better visualization of the conducting peaks of PANI and SPR peak of gold nanoparticles. The conducting form of the PANI have distinctive bands at around 800 and 420 nm[101], which are clearly seen in the spectra. The red shift in the gold SPR peak position (Figure 5.5b) is an evidence of the encapsulation of gold core by PANI shell, but it seems to have reached a plateau after 90 minutes. As the polymerization time increases, the increase in shell thickness of PANI is indicated by the increase in the absorption intensity at around 800 nm.

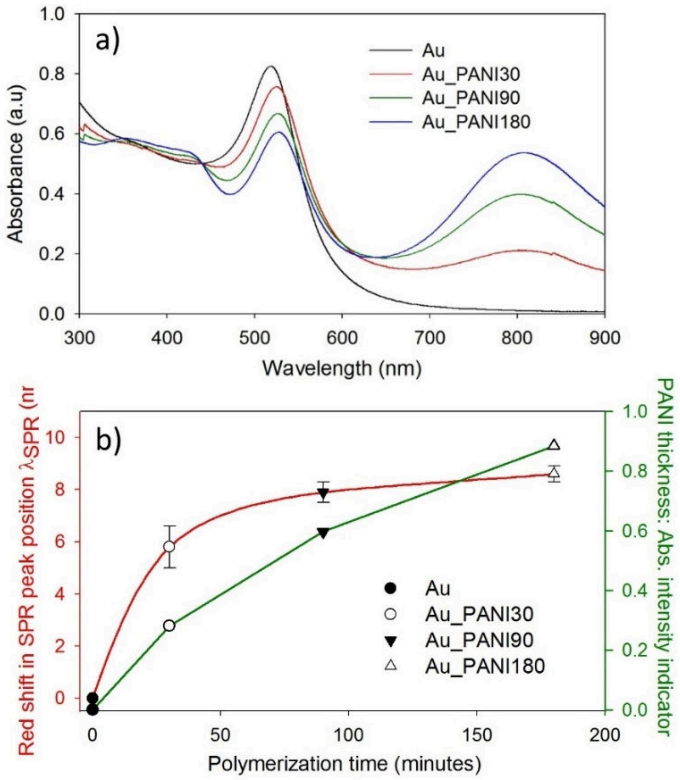

Figure 5.5. a) UV-vis absorption spectra of gold and PANI encapsulated gold nanoparticle colloidal solutions. b) Magnitude of the red shift (red curve) in SPR peak position as a function of polymerization time. The PANI thickness indicator is shown with a green solid line and the axis is represented on the right side as a secondary y-axis.

This was quantified by a ratio of absorption intensity of PANI peak to gold SPR peak, and the increase of this PANI thickness indicator (Figure 5.5b) proves that the shell thickness is increasing. The shell thickness measurements were obtained by TEM analysis as shown in Figure 5.6. The increase in shell thickness is evident as the polymerization time in increased from 30 to 180 minutes. An ultra-thin PANI shell of thickness 1.4 ± 0.5 nm is obtained for a polymerization time of 30 minutes (Figure 5.6a, Au_PANI30) which increases to 4.1 ± 1.4 nm after 90 minutes (Figure 5.6b, Au_PANI90) and finally a thickness of 7.5 ± 1.6 nm (Figure 5.6c, Au_PANI180) after 180 minutes of polymerization. The shell thickness distributions are shown at the bottom of the corresponding images.

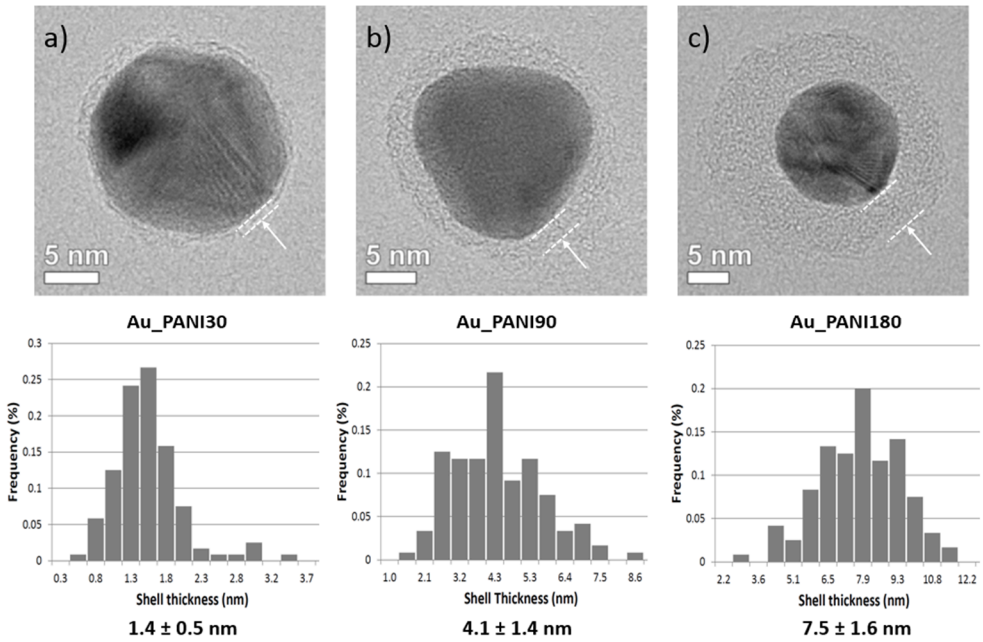

Figure 5.6. TEM images of gold@PANI core@shell nanoparticles and the corresponding shell thickness distribution after a polymerization time of **a)** 30 minutes (Au_PANI30), **b)** 90 minutes (Au_PANI90) and **c)** 180 minutes (Au_PANI180). The shell thickness distributions were obtained from 120 measurements.

5.3.3 Conductivity analysis of core@shell nanoparticles

In the second chapter, an in-depth analysis on the electrical conductivity of the silver-polymer core-shell nanoparticles was performed using conductive tip AFM methodology. The results were consistent with the IV voltammetry measurements, which indicated that the polyelectrolyte layers are insulating in nature and resists the flow of electrons through its domain. Therefore, by measuring the current-voltage (IV) properties of the as-prepared gold@polymer, gold@PANI nanocluster films can provide a relative comparison in resistivity between bare gold nanoparticles and polymer encapsulated gold nanoparticles. A similar methodology of performing IV voltammetry using the flexible interdigitated electrode chips (IDE) was adapted. Additional measurements using conductive tip AFM were also performed. The detailed description regarding this procedure was already discussed in chapter 2. The IV voltammetry plots obtained using IDE chips are shown in Figure 5.7 and the conductive

tip AFM measurements are shown in Figure 5.8. From the IV plots (Figure 5.7 and 5.8) it is clear that gold and gold@PANI nanoparticles are conducting in nature, whereas the four-layered (Au_L4) gold@polymer nanoparticles display typical behavior of insulating material with high resistivity. This means that the polyelectrolyte shell of the core@shell sample Au_L4, composed of polymers $(PAH/PSS)_2$, does not allow for electron or charge transfer through its medium. On the contrary, the similar core@shell structure of Au@PANI, i.e. sample Au_PANI180, exhibit good conductive property. This proves that the PANI shell allows transfer of charges or flow of electrons through its shell domain around the gold core. This analysis of the electrical conductivity properties is of utmost importance since the polymer and PANI shell act as a spacer layer between the gold nanoparticle and semiconductor photocatalyst. Therefore, this study provides a clarity on the charge-transfer inhibition property of polymer shell and validate the conventional understanding that PANI is conducting.

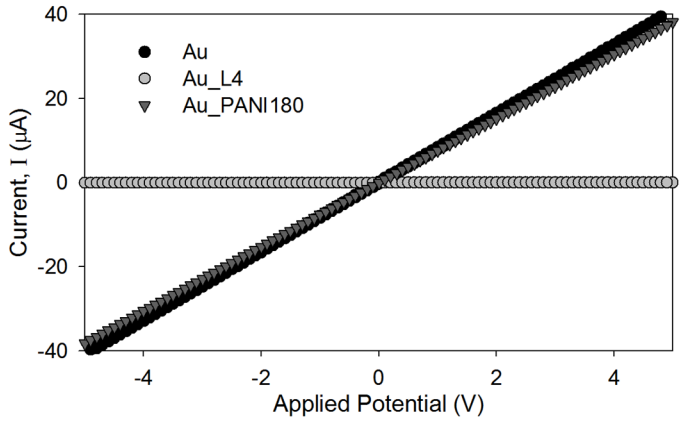

Figure 5.7. Current-Voltage (IV) voltammetry of as synthesized gold nanoparticles (black circles), gold@polymer core@shell nanoparticles (grey circles) and gold@PANI core@shell nanoparticles (dark grey triangles).

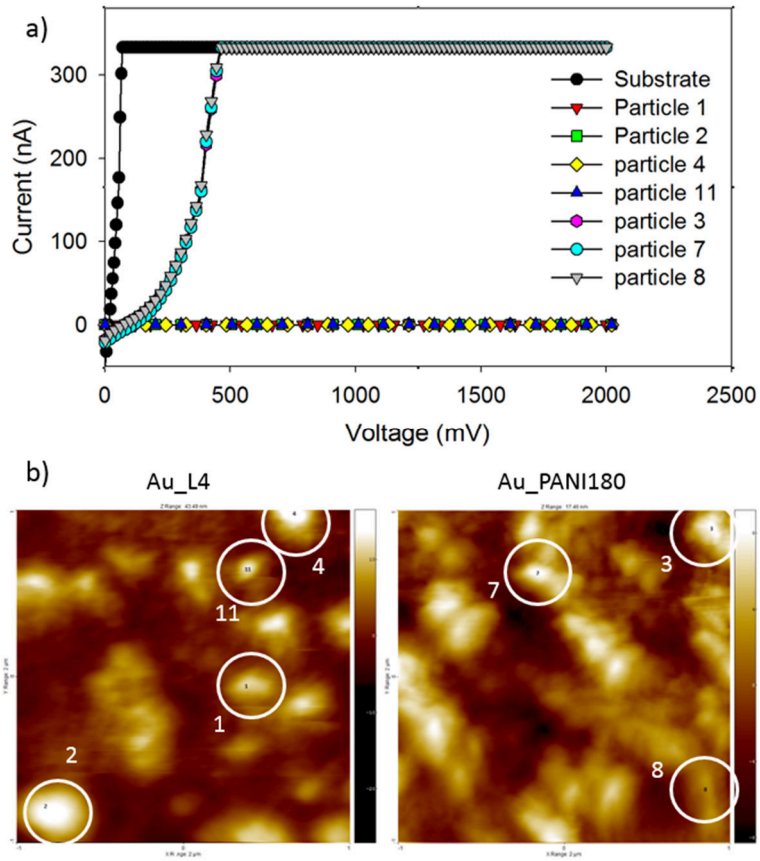

Figure 5.8.a) Current-voltage (I-V) data performed on particles with corresponding numbers shown in AFM profile maps. **b)** AFM surface profile maps of Au_L4 and Au_PANI180 nanoparticles dropcasted on gold-coated silicon substrate. The numbered particles on which the conductive-tipped AFM IV measurements were performed are shown in white circles.

5.3.4 Mechanism elucidation Au-TiO_2 plasmonic photocatalytic system.

The main objective for the synthesis of different types of Au-TiO_2 plasmonic photocatalytic systems using core@shell nanoparticles, with encapsulated gold nanoparticle in the core, is to understand the underlying mechanism for enhancement of photocatalysis using gold plasmonic nanoparticles. For this purpose, different photocatalytic samples were prepared as described in the experimental section and tested for photocatalytic degradation of stearic acid. Stearic acid was chosen as a model pollutant because of its stability and the degradation kinetics are independent

of the photocatalytic film thickness[196]; and is a model component for standardized comparison of ISO tests of the self-cleaning properties of photocatalysts[197]. The decrease in the stearic acid film thickness, which was spin coated on top of the photocatalyst sample, was monitored by measuring the integrated absorbance in the wavenumber range of 2800 – 3200 cm^{-1}. The results from the stearic acid degradation of different Au-TiO_2 photocatalytic systems, which are listed in Table 5.1, are plotted in Figure 5.9. Since it is well known that stearic acid degradation follows a zero order kinetic reaction in the case of flat and dense films[104,196], a linear estimation fit for the degradation with the corresponding R-squared values are also shown in the Figure 5.9a. The rates of the reaction are shown in Figure 5.9b, which provides a clear picture on the differences in the photocatalytic activity between the samples.

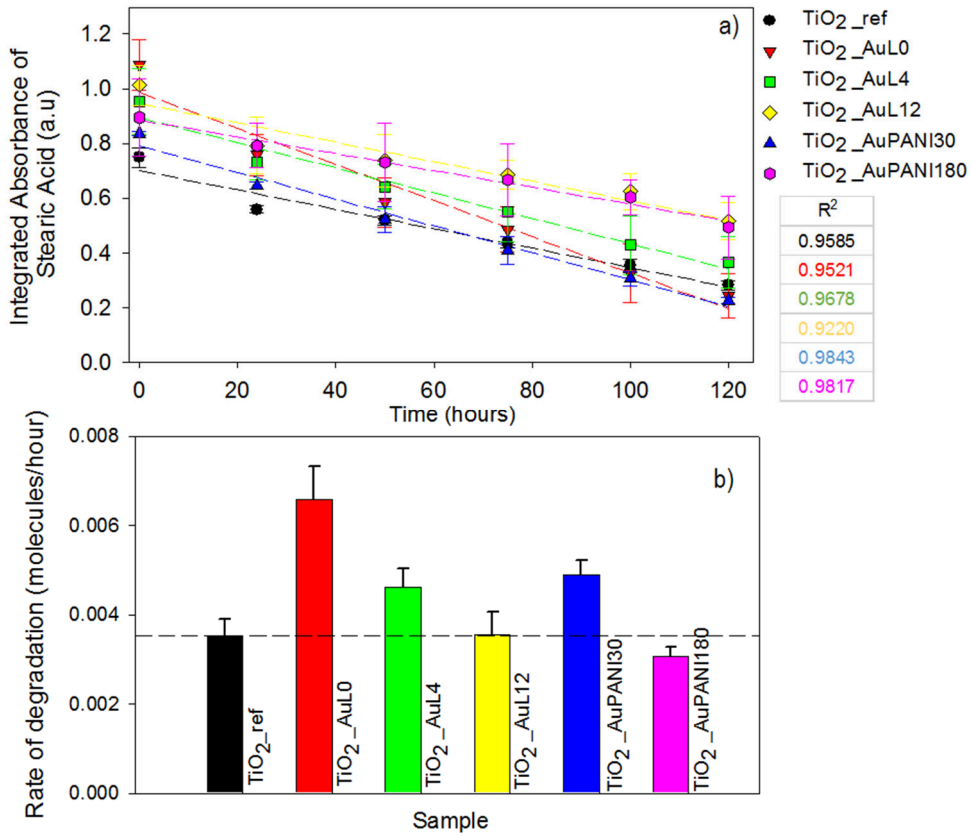

Figure 5.9. Photocatalytic degradation of stearic acid using different Au-TiO_2 systems under visible green LED light (λ = 515 nm). The zero order rate and the R^2 of the linear fit of the kinetics are shown below the legend on right side in corresponding color code.

From Figure 5.9, it is interesting to observe the visible light activity of the reference TiO_2 sample (P25). However it has been reported that P25, which consists of 80-20 ratio of anatase-rutile phase crystals, show reasonable visible light activity because of defects at the anatase-rutile "hot-spot" interface[198]. Some researchers also demonstrated the visible light response by means of EPR and photoluminescence measurements of P25[199,200]. The highest rate is shown when bare gold nanoparticles are loaded onto TiO_2 i.e., sample TiO_2_AuL0, which could be assigned to the synergetic effect of the LSPR i.e., direct electron transfer and near–electric field, and the Schottky contact effect that keeps the charges separated at the metal-semiconductor interface. These processes would boost the activity by increasing the rate of charge carrier formation resulting in enhanced stearic acid degradation compared to the reference system. When TiO_2 is loaded with gold nanoparticles encapsulated with an ultrathin insulating polymer shell of thickness 1.7 ± 0.5 nm (TiO_2_AuL4), the ultrathin polymer layer acts as an insulating spacer layer. In such scenario, the direct electron transfer is not possible and the enhancement in the rate of reaction (green bar) is due to the near-electric field at the active sites on the surface of TiO_2 that contain defects[64,81,186]. Since TiO_2 is not photoactive under visible light, this could be the only possibility that near-field boosts the visible light active defect sites of P25-TiO_2. The sample with polymer shell thickness of 3.2 nm (TiO_2_AuL12), increases the insulating spacer layer thickness and eventually reduces the near-electric field intensity available at the surface of TiO_2 resulting in the drop in the enhancement (yellow bar).

The field simulation maps as seen from Figures 5.10b, 5.10c and 5.10d also corroborate the drop in near-electric field at the surface of TiO_2 because of the increased spacer layer thickness. In the previous chapter, this drop in the near-electric field was corroborated with experimental evidence using SERS. The modeling and simulation methodology is described in detail in chapter 3; the refractive index (n=1.4, k=0.027) and conductivity (σ = 50 S/m) data of PANI were taken from literature[101,201]. The results provided the distance dependency of near-electric field from the surface of nanoparticle and at a distance of 3.2 ± 0.8 nm (Au_L12) the field effects become

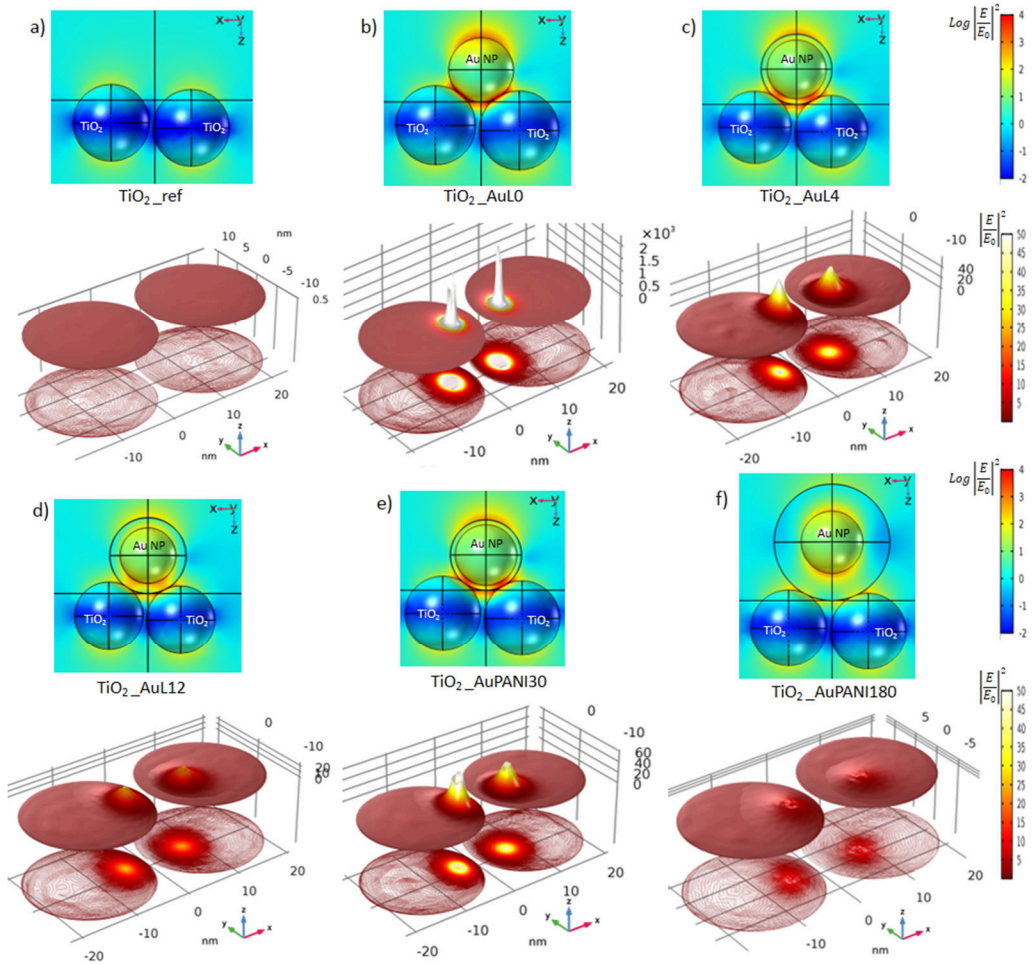

Figure 5.10. Near-field enhancement distribution maps of Au-TiO_2 systems with the TiO_2 surface contours and the projection of enhancement along the surface of two TiO_2 nanoparticles with a height intensity scale at the bottom of corresponding system. The different systems shown here are depiction of the samples used for photocatalytic tests with the idea of a gold nanoparticle on top of two TiO_2 nanoparticles.

insignificant. This trend is also shown by the photocatalytic activity rate of sample TiO_2_AuL12 (Figure 5.9), which shows no enhancement compared to the reference system. The sample with a conductive spacer layer (TiO_2_AuPANI30) shows a significant improvement in the stearic acid degradation rate. This is because of the direct electron transfer from the excited electrons from the conduction band of gold that is injected through the PANI spacer layer towards the TiO_2 surface. The thickness of the conductive spacer layer is 1.4 ± 0.5 nm, which is similar to insulating spacer layer

thickness of sample TiO_2_AuL4 resulting in similar near-electric field available at TiO_2 surface (Figures 5.10c and 5.10e). Therefore, the near-electric field and direct electron transfer should be both possible for TiO_2_AuPANI30 system. However, the improvement in the rate is not significantly higher than TiO_2_AuL4, as one would expect the synergetic effect of both the LSPR process i.e., near-electric field and direct electron transfer. There is a possibility that the conductive PANI spacer interferes with the enhancement effect of either the electric field or the electron transfer process. This is because PANI itself also has a visible light absorption behavior and leads to formation of hot-holes when in contact with gold nanoparticles under visible light[202]. So the hot electrons have more chance of recombination at the hot holes induced by the PANI interface layer and reduces the amount of charge carriers available for the photoreaction. When the conductive spacer layer thickness is increased to 7.5±1.6 nm i.e., sample TiO_2_AuPANI180, there is no improvement in the rate and a decrease in the photocatalytic activity is observed from Figure 5.9. At this shell thickness, there is no electric field enhancement (Figure 5.10f) but electron transfer should be possible. However, the shell thickness of 7.5 nm is more than the mean free path of conduction band electrons for gold nanoparticles[138,203]. The relation between the nanoparticle size and mean free path of electrons is given as below[203].

$$\frac{1}{\mathrm{l_m}} = \frac{1}{\mathrm{l_{m_b}}} + \frac{1}{\mathrm{R}}$$

Where l_m, $l_{m_b}$are the mean free path lengths in nanoparticle and bulk gold respectively and R is the radius of the nanoparticle. The mean free path length in bulk for gold is 42 nm[138], and the average size of gold nanoparticles used in this study is 8.5 nm in radius (Figure 5.4), so the calculated mean free path l_m is 7.1 nm. Therefore, the ease of direct electron transfer induced by SPR of Au is diminished and is also dependent on coupling of electronic states of Au and PANI for the system TiO_2_AuPANI180. Moreover, the efficiency of charge transfer is also dependent on the distance/spacing between the plasmon and semiconductor surface, and the electron transport characteristics of PANI. As the near-electric field effect could be excluded at

a spacer layer thickness of 7.5 ± 1.6 nm (Figure5.10f), the enhancement in photocatalytic activity is not possible which is evident from the minor decrease in the rate of reaction in Figure 5.9. Therefore, the overall reduction in photocatalytic activity enhancement for system TiO_2_AuPANI180 could be because of the combination of the aforementioned phenomenon.

5.4 *Conclusions*

It can be summarized that both the LSPR phenomenon i.e., direct electron transfer and near-electric field enhancement contribute to the plasmonic enhancement of photocatalysis in the case of direct contact between the metal and semiconductor. However, finding the dominant mechanism by the idea of a spacer layer such as PANI does not yield clear results owing to the high complexity of the system with multiple interfaces between TiO_2, PANI and gold. In such systems multiple processes occur concurrently in both ways, they can be both augmenting and counterproductive at the same time. Nevertheless, this study provides definitive analysis on the importance of maintaining close vicinity of less than two nanometers between the plasmonic nanoparticles and semiconductor to achieve plasmonic enhancement in photocatalysis.

Chapter 6

Conclusion and prospects

“Science is about knowing; Engineering is about doing.” – Henry Petroski

6.1 *General conclusions*

Noble metal nanoparticles have a unique plasmonic property called surface plasmon resonance, which can be utilized to enhance processes such as photocatalysis and Raman spectroscopy. The main conclusions reached in this thesis with respect to the application of silver and gold plasmonic nanoparticles (average diameter of ca. 20 nm) for enhancement of TiO_2 based photocatalysis and Raman spectroscopy are:

- Near-electric field at the interface of silver and TiO_2 is a crucial mechanism for silver plasmon enhanced gas phase photocatalysis. The enhancement becomes ineffective if the semiconductor and silver plasmonic nanoparticle are not in contact or within the vicinity of a couple of nanometers.
- Near-electric field or electromagnetic enhancement is the major factor in attaining high enhancement factor when silver or gold nanoparticles are used in surface enhanced Raman spectroscopy. The Raman probe molecule has to be confined within two nanometers from the surface of the plasmonic nanoparticle to achieve significant improvement in Raman signal. The overlap of the surface plasmon resonance of the plasmonic nanostructure and the Raman laser excitation wavelength is also crucial for effective Raman enhancement.
- Gold plasmon enhanced photocatalysis using visible light is effective, provided there is a direct contact or conductive interface of less than 2 nm, between the TiO_2 semiconductor photocatalyst and gold nanoparticle. In other words, charge transfer, although unknown in direction i.e., from gold to TiO_2 or vice-versa, is a major factor in improvement of photocatalytic activity using gold nanoparticles.

The intense near-electric fields generated at the surface of plasmonic nanoparticle and the charge transfer mechanism were studied in detail in this work through a spacer layer, which is either insulating or conductive. A mechanistic approach to study the mechanism of plasmon-enhanced photocatalysis was provided in the first chapter. A prelude to the application of photocatalysis in pollution remediation and the boosting of photocatalytic activity using plasmonic nanoparticles

was provided with a brief overview on the widespread deterioration of urban air quality through the world as a problem statement.

A generic overview of this thesis consists of an approach to tune the intensity of near-electric field at the surface of silver/gold plasmon nanoparticles was shown by building an ultra-thin polyelectrolyte shell encapsulating the plasmonic nanoparticle. This was done by using a simple wet chemical synthesis technique called layer-by-layer method. The layer-by-layer method is based on the principle of alternate deposition of positive and negative charged polyelectrolytes on colloidal templates i.e., silver and gold plasmonic nanoparticle. The layer-by-layer method provides a very good control of the thickness of the layers deposited around the plasmonic nanoparticle. Typically, the average thickness of layer-by-layer synthesized polyelectrolyte shell is in the order of one nanometer per four layers of polyelectrolytes for nanoparticles in the size range of 15-20 nm. The polyelectrolyte encapsulated plasmonic nanoparticle had a core-shell morphology as analyzed from transmission electron micrograph images, and were termed as (silver/gold)@polymer core@shell nanoparticle. The effect of the polyelectrolyte layered shell thickness on the red shift of plasmon peak wavelength position was established by spectrophotometric measurements. The shell thickness measurements obtained by TEM analysis were used in theoretical calculations to estimate the red shift in plasmon peak position of the plasmonic nanoparticle using analytical solutions of Mie thoery. The experimental and theoretical red shifts in plasmon peak position showed a good fit showcasing the accuracy of the theoretical models, which were used to analyze the effect of polymer shell thickness on the intensity of the near-electric field at the outer surface of plasmonic nanoparticle-polymer core-shell nanoparticles. Three-dimension models were created using finite element method in COMSOL Multiphysics® to estimate the extent of the availability of near-electric field in the close vicinity of plasmonic nanoparticle surface. The COMSOL models and the near-field simulations also provided crucial hypothesis to corroborate the experimental results. The near-electric field distribution maps were used extensively throughout this thesis as a theoretical evidence to support the conclusions.

In the second chapter silver@polymer core@shell nanoparticles were used for plasmonic enhancement of gas phase TiO_2 photocatalysis using acetaldehyde as a model indoor air pollutant. The results provided a crucial insight into the distance dependency of plasmonic enhancement at which the plasmons enhance the photocatalysis. This found to be in the order of less than two nanometers, as the insulating polyelectrolyte shell acted as a spacer layer between the TiO_2 and silver nanoparticle. A similar study using a conductive spacer layer, as described in the introduction chapter by the synthesis of a conductive PANI shell around silver nanoparticle, was not possible. This is because the synthesis of conductive polyaniline shell was unsuccessful after multiple attempts. This could be because of the unstable nature of silver colloidal nanoparticles that are very sensitive to pH of the solutions used in the in-situ synthesis protocol of conductive polyaniline shell. However, the trend provided by the photocatalytic activity results using the 1.4 nm and 4.1 nm thick insulting polyelectrolyte shell, suggests at the importance of near-electric field induced photocatalytic enhancement. The repeatability of the layer-by-layer synthesis of encapsulated silver nanoparticles by polyelectrolyte shell, and corresponding shell thickness deviations were analyzed in chapter 3. Theoretical Mie calculations using the coated sphere solution implemented in MATLAB and COMSOL, for the silver@polymer core@shell nanoparticles, provided a good fit with the experimental optical properties. The near-field maps of the Ag-TiO_2 interface had a good fit with the experimental results which reiterates the crucial role of near-electric field enhancement. Chapter 3 also provides an in-depth analysis of the modeling techniques needed to achieve the accuracy and highlights some of the pitfalls of using the COMSOL models.

To verify the hypothesis that near-field is confined to within few nanometers from the surface of plasmonic nanoparticle, SERS was used as an experimental evidence in chapter 4. SERS substrates were prepared using gold and silver nanoparticles and the distance dependency of the near-field is tested by using the (gold/silver)@polymer core@shell nanoparticles with different shell thickness. And a

significant drop or no enhancement in SERS was found for nanoparticles with shell thickness more than 1.4 nm for silver and 2.1 nm for gold. Therefore, the SERS experiments provided a convincing proof that the near-field enhancement is confined to within two nanometers, which could be utilized for improving the plasmon application-oriented process such as photocatalysis. It is important to note that this conclusion is specific to silver and gold nanoparticles with an average size not more than 25 nm.

In chapter 5, the mechanistic approach outlined in the introduction chapter was applied to study the mechanism responsible for gold plasmon enhanced TiO_2 photocatalysis. However, even after repeated photocatalytic measurements, a clear trend was not attainable, although the study provides some clues. Different methods of incorporation of gold nanoparticles into TiO_2 were explored, but the random nature of enhancement was ambiguous. The best possible results were showcased and probable causes of different mechanisms were discussed. The highest levels of enhancement for the Au-TiO_2 systems was achieved when the metal and semiconductor are in direct contact. This hints at the dominant role played by the charge transfer and Schottky contact phenomenon in Au-TiO_2 plasmonic photocatalytic systems, but more tests should be carefully planned and executed with due consideration of the sensitive nature of delicate polyelectrolyte shell. As discussed in chapter 2, synthesis of photo-deposited Au-TiO_2 similar to Ag-TiO_2 powder samples revealed that the polymer shell is not stable under the processes of centrifuge, drying and grinding. Similar mechanistic study was planned in the initial stages using ALD methodology to create spacer layers between plasmonic nanoparticles and TiO_2. However, it was found that usage of different types of plasma during the deposition of silver nanoparticles on crystalline TiO_2 destroys the photocatalytic nature of TiO_2. This was confounded with the fact that repeatability is an issue using zeolite templates to enhance the surface area factor. Additional tests to analyze the effect of plasma on the crystalline surface of TiO_2 also presented significant roadblocks in using ALD methods for investigating the mechanism of plasmon-enhanced photocatalysis. In

conclusion, this thesis takes a significant step forward in understanding the role played by the near-field enhancement and direct electron transfer in plasmonic systems. To summarize in a single sentence, plasmonic nanoparticles should be in close vicinity i.e., less than two nanometers, of the probe molecule in case of SERS and semiconductor in case of TiO_2 photocatalysis, to achieve the best possible enhancements of the process.

6.2 *Future prospects*

The outcome of this thesis work has led to an important reiteration regarding the stability of silver nanoparticles and the related drawbacks with respect to application of silver plasmonic nanoparticles in different process. Ultra-stable polyelectrolyte encapsulated silver nanoparticles could be a good alternative for applications involving the usage of plasmonic silver nanoparticles. Additionally, the polymer protected silver or gold plasmonic nanoparticles showed significant enhancements in Raman spectroscopy, which is promising for the development of stable long-lasting SERS substrates. The SERS experiments also provided crucial insight on achieving highest possible enhancements through overlap of surface plasmon resonance wavelength and Raman laser excitation wavelength. This concept could be used to synthesize plasmonic nanoparticles of single metal or alloys by fine-tuning the size and SPR wavelength and eventually boost the SERS enhancements to maximum attainable level. The importance of hot spots and periodic arrangement of plasmonic nanoparticles demonstrated in this work could be utilized to incorporate plasmonic nanoparticles in the highly ordered silica nanostructures of diatoms (algae). Some studies have reported development of such plasmon incorporated silica nanostructures that can be useful because of their broadband properties[204,205]. Such nanostructures also have interesting optical properties that could be utilized for the development of sensors based on colorimetric detection. The other most important outlook this work has provided is that finite element models and near-electric field simulations could be used to accomplish crucial insights and act as a vital mechanistic tool for studying plasmonic systems.

Bibliography

[1] *"WHO | Air pollution," can be found under http://www.who.int/topics/air_pollution/en/,* ***2018****.*

[2] *"WHO | Media Centre. News release, Geneva 25th March 2014," can be found under http://www.who.int/mediacentre/news/releases/2014/air-pollution/en/,* ***2014****.*

[3] *I. Bos, P. De Boever, L. Int Panis, R. Meeusen,* Sport. Med. ***2014****,* 44*, 1505–1518.*

[4] WHO | Ambient (Outdoor) Air Quality and Health*, World Health Organization,* ***2016****.*

[5] *A. Seaton, D. Godden, W. MacNee, K. Donaldson,* Lancet ***1995****,* 345*, 176–178.*

[6] *H. Orru, K. L. Ebi, B. Forsberg,* Curr. Environ. Heal. reports ***2017****,* 4*, 504–513.*

[7] *R. A. Silva, J. J. West, J.-F. Lamarque, D. T. Shindell, W. J. Collins, S. Dalsoren, G. Faluvegi, G. Folberth, L. W. Horowitz, T. Nagashima, et al.,* Atmos. Chem. Phys. ***2016****,* 16*, 9847–9862.*

[8] *K. L. Ebi, G. McGregor,* Environ. Health Perspect. ***2008****,* 116*, 1449–55.*

[9] *R. M. Doherty, M. R. Heal, F. M. O'Connor,* Environ. Heal. ***2017****,* 16*, 118.*

[10] *J. Burney, V. Ramanathan,* Proc. Natl. Acad. Sci. U. S. A. ***2014****,* 111*, 16319–24.*

[11] *E. Paoletti, M. Schaub, R. Matyssek, G. Wieser, A. Augustaitis, A. M. Bastrup-Birk, A. Bytnerowicz, M. S. Günthardt-Goerg, G. Müller-Starck, Y. Serengil,* Environ. Pollut. ***2010****,* 158*, 1986–1989.*

[12] *S. Kephalopoulos, O. Geiss,* European Collaborative Action Urban Air, Indoor Environment and Human Exposure Report No. 29*,* ***2013****.*

[13] *J. H. Seinfeld, S. N. Pandis,* Atmospheric Chemistry and Physics: From Air Pollution to Climate Change*, Wiley-VCH Verlag GmbH,* ***2016****.*

[14] *A. H. Goldstein, C. D. Koven, C. L. Heald, I. Y. Fung,* Proc. Natl. Acad. Sci. U. S. A. ***2009****,* 106*, 8835–40.*

[15] *M. Fischetti,* Sci. Am. ***2014****,* 310*, 14–14.*

[16] *J. Jouzel, C. Lorius, J. R. Petit, C. Genthon, N. I. Barkov, V. M. Kotlyakov, V. M. Petrov,* Nature ***1987****,* 329*, 403–408.*

[17] *A. Neftel, E. Moor, H. Oeschger, B. Stauffer,* Nature ***1985****,* 315*, 45–47.*

[18] *J. M. Barnola, D. Raynaud, Y. S. Korotkevich, C. Lorius,* Nature ***1987****,* 329*, 408–414.*

[19] *D. Lüthi, M. Le Floch, B. Bereiter, T. Blunier, J.-M. Barnola, U. Siegenthaler, D. Raynaud, J. Jouzel, H. Fischer, K. Kawamura, et al.,* Nature ***2008****,* 453*, 379–382.*

[20] *J. R. Petit, J. Jouzel, D. Raynaud, N. I. Barkov, J.-M. Barnola, I. Basile, M. Bender, J. Chappellaz, M. Davis, G. Delaygue, et al.,* Nature ***1999***, 399, *429–436.*

[21] *"Climate Change: Climate Resource Center - Graphic: The relentless rise of carbon dioxide," can be found under https://climate.nasa.gov/climate_resources/24/,* ***2018****.*

[22] *US EPA Office of Air and Radiation, "Particulate Matter (PM) Pollution," can be found under https://www.epa.gov/pm-pollution,* ***2017****.*

[23] *"Air pollution — European Environment Agency," can be found under https://www.eea.europa.eu/themes/air,* ***2017****.*

[24] *J. S. Brown, T. Gordon, O. Price, B. Asgharian,* Part. Fibre Toxicol. ***2013***, 10, *12.*

[25] *R. Beelen, G. Hoek, P. A. van den Brandt, R. A. Goldbohm, P. Fischer, L. J. Schouten, M. Jerrett, E. Hughes, B. Armstrong, B. Brunekreef,* Environ. Health Perspect. ***2007***, 116, *196–202.*

[26] *G. B. Hamra, N. Guha, A. Cohen, F. Laden, O. Raaschou-Nielsen, J. M. Samet, P. Vineis, F. Forastiere, P. Saldiva, T. Yorifuji, et al.,* Environ. Health Perspect. ***2014***, 122, *906–911.*

[27] *R. T. Burnett, I. Pope, C. Arden, M. Ezzati, C. Olives, S. S. Lim, S. Mehta, H. H. Shin, G. Singh, B. Hubbell, M. Brauer, et al.,* Environ. Health Perspect. ***2014***, 122, *397–403.*

[28] *K. Katsouyanni, G. Touloumi, C. Spix, J. Schwartz, F. Balducci, S. Medina, G. Rossi, B. Wojtyniak, J. Sunyer, L. Bacharova, et al.,* BMJ ***1997***, 314, *1658–63.*

[29] *S. Fuzzi, U. Baltensperger, K. Carslaw, S. Decesari, H. Denier van der Gon, M. C. Facchini, D. Fowler, I. Koren, B. Langford, U. Lohmann, et al.,* Atmos. Chem. Phys. ***2015***, 15, *8217–8299.*

[30] *F. Laden, L. M. Neas, D. W. Dockery, J. Schwartz,* Environ. Health Perspect. ***2000***, 108, *941–7.*

[31] *"Professor Ed Hawkins : UoR, Dept Of Meteorology," can be found under http://www.met.reading.ac.uk/~ed/home/index.php,* ***2016****.*

[32] *"Standards - Air Quality - Environment - European Commission," can be found under http://ec.europa.eu/environment/air/quality/standards.htm,* ***2008****.*

[33] *"Environmental Quality Standards in Japan - Air Quality [MOE]," can be found under https://www.env.go.jp/en/air/aq/aq.html,* ***2009****.*

[34] *US EPA Office of Air and Radiation, "NAAQS Table," can be found under https://www.epa.gov/criteria-air-pollutants/naaqs-table,* ***2010****.*

[35] *Ministry of Environmental Protection The People's Republic of China, "Ambient air quality standards - MEP PRC," can be found under http://english.sepa.gov.cn/Resources/standards/Air_Environment/quality_standard1/201605/t20160511_337502.shtml,* ***2012****.*

[36] *"Central Pollution Control Board - India," can be found under http://cpcb.nic.in/air-pollution/,* ***2009****.*

[37] *"Air Pollution in World: Real-time Air Quality Index Visual Map," can be found under http://aqicn.org/map/world/,* ***2018****.*

[38] *"Worldwide Air Pollution Map and live air quality levels," can be found under https://air.plumelabs.com/en/,* ***2018****.*

[39] *"AirVisual Earth - 3D Real-time Air pollution map," can be found under https://www.airvisual.com/earth,* ***2018****.*

[40] *"European Air Quality Index," can be found under http://airindex.eea.europa.eu/,* ***2018****.*

[41] *J. Cyrys, A. Peters, J. Soentgen, H.-E. Wichmann,* J. Air Waste Manage. Assoc. ***2014****,* 64*, 481–487.*

[42] *H. Boogaard, N. A. H. Janssen, P. H. Fischer, G. P. A. Kos, E. P. Weijers, F. R. Cassee, S. C. van der Zee, J. J. de Hartog, K. Meliefste, M. Wang, et al.,* Sci. Total Environ. ***2012****,* 435–436*, 132–140.*

[43] *P. Panteliadis, M. Strak, G. Hoek, E. Weijers, S. van der Zee, M. Dijkema,* Atmos. Environ. ***2014****,* 86*, 113–119.*

[44] *A. Fujishima, X. Zhang, D. A. Tryk,* Int. J. Hydrogen Energy ***2007****,* 32*, 2664–2672.*

[45] *A. Mills, S. Le Hunte,* J. Photochem. Photobiol. A Chem. ***1997****,* 108*, 1–35.*

[46] *M. R. Hoffmann, S. T. Martin, W. Choi, D. W. Bahnemann,* Chem. Rev. ***1995****,* 95*, 69–96.*

[47] *A. Fujishima, T. N. Rao, D. A. Tryk,* J. Photochem. Photobiol. C Photochem. Rev. ***2000****,* 1*, 1–21.*

[48] *K. Hashimoto, H. Irie, A. Fujishima,* Jpn. J. Appl. Phys. ***2005****,* 44*, 8269–8285.*

[49] *A. Fujishima, K. Honda,* Nature ***1972****,* 238*, 37–38.*

[50] *M. Anpo, P. V. Kamat,* Environmentally Benign Photocatalysts : Applications of Titanium Oxide-Based Materials*, Springer,* ***2010****.*

[51] *Y. Ohama, D. Van Gemert, Eds. ,* Applications of Titanium Dioxide Photocatalysis to Construction Materials*, Springer Netherlands, Dordrecht,* ***2011****.*

[52] *K. Nakata, A. Fujishima,* J. Photochem. Photobiol. C Photochem. Rev. ***2012****,* 13*, 169–189.*

[53] *U. Diebold,* Surf. Sci. Rep. ***2003****,* 48*, 53–229.*

[54] *G. Odling, N. Robertson,* ChemSusChem ***2015****,* 8*, 1838–1840.*

[55] *T. Luttrell, S. Halpegamage, J. Tao, A. Kramer, E. Sutter, M. Batzill,* Sci. Rep. ***2015****,* 4*, 4043.*

[56] *Y. Nosaka, A. Y. Nosaka,* Chem. Rev. ***2017****,* 117*, 11302–11336.*

[57] ASTM G173 - 03(2012) Standard Tables for Reference Solar Spectral Irradiances: Direct Normal and Hemispherical on 37° Tilted Surface*, West Conshohocken, PA,* ***2012****.*

[58] J. Schneider, M. Matsuoka, M. Takeuchi, J. Zhang, Y. Horiuchi, M. Anpo, D. W. Bahnemann, Chem. Rev. ***2014****,* 114*, 9919–9986.*

[59] A. Fujishima, X. Zhang, Comptes Rendus Chim. ***2006****,* 9*, 750–760.*

[60] Y. Wang, J. Li, H. Jing, Q. Zhang, J. Jiang, P. Biswas, Aerosol Sci. Technol. ***2015****,* 49*, 1063–1077.*

[61] W. Hou, S. B. Cronin, Adv. Funct. Mater. ***2013****,* 23*, 1612–1619.*

[62] K. Awazu, M. Fujimaki, C. Rockstuhl, J. Tominaga, H. Murakami, Y. Ohki, N. Yoshida, T. Watanabe, J. Am. Chem. Soc. ***2008****,* 130*, 1676–1680.*

[63] S. W. Verbruggen, J. Photochem. Photobiol. C Photochem. Rev. ***2015****,* 24*, 64–82.*

[64] S. Linic, P. Christopher, D. B. Ingram, Nat. Mater. ***2011****,* 10*, 911–921.*

[65] C. Clavero, Nat. Photonics ***2014****,* 8*, 95–103.*

[66] S. W. Verbruggen, M. Van Hal, T. Bosserez, J. Rongø, B. Hauchecorne, J. A. Martens, S. Lenaerts, ***2017****, 1–7.*

[67] K. L. Kelly, E. Coronado, L. L. Zhao, G. C. Schatz, J. Phys. Chem. B ***2003****,* 107*, 668–677.*

[68] W. A. Murray, W. L. Barnes, Adv. Mater. ***2007****,* 19*, 3771–3782.*

[69] X. Zhou, G. Liu, J. Yu, W. Fan, J. Mater. Chem. ***2012****,* 22*, 21337.*

[70] S. W. Verbruggen, M. Keulemans, M. Filippousi, D. Flahaut, G. Van Tendeloo, S. Lacombe, J. a. Martens, S. Lenaerts, Appl. Catal. B Environ. ***2014****,* 156–157*, 116–121.*

[71] N. Zhang, S. Liu, X. Fu, Y. J. Xu, J. Phys. Chem. C ***2011****,* 115*, 9136–9145.*

[72] D. B. Ingram, P. Christopher, J. L. Bauer, S. Linic, ACS Catal. ***2011****,* 1*, 1441–1447.*

[73] K. H. Leong, A. A. Aziz, L. C. Sim, P. Saravanan, M. Jang, D. Bahnemann, Beilstein J. Nanotechnol. ***2018****,* 9*, 628–648.*

[74] X. Zhang, Y. L. Chen, R.-S. Liu, D. P. Tsai, Reports Prog. Phys. ***2013****,* 76*, 046401.*

[75] K. Ishibashi, A. Fujishima, T. Watanabe, K. Hashimoto, J. Photochem. Photobiol. A Chem. ***2000****,* 134*, 139–142.*

[76] S. K. Cushing, J. Li, J. Bright, B. T. Yost, P. Zheng, A. D. Bristow, N. Wu, J. Phys. Chem. C ***2015****,* 119*, 16239–16244.*

[77] C. Boerigter, R. Campana, M. Morabito, S. Linic, Nat. Commun. ***2016****,* 7*, 10545.*

[78] C. F. Bohren, D. R. Huffman, Absorption and Scattering of Light by Small Particles*, Wiley-VCH Verlag GmbH, Weinheim, Germany,* ***1998****.*

[79] S. Link, M. A. El-Sayed, Annu. Rev. Phys. Chem. ***2003****,* 54*, 331–366.*

[80] *P. K. Jain, K. S. Lee, I. H. El-Sayed, M. A. El-Sayed,* J. Phys. Chem. B ***2006***, 110, *7238–7248.*

[81] *E. Kowalska, O. O. P. Mahaney, R. Abe, B. Ohtani,* Phys. Chem. Chem. Phys. ***2010***, 12, *2344.*

[82] *Z. Bian, T. Tachikawa, P. Zhang, M. Fujitsuka, T. Majima,* J. Am. Chem. Soc. ***2014***, 136, *458–465.*

[83] *C. Gomes Silva, R. Juárez, T. Marino, R. Molinari, H. García,* J. Am. Chem. Soc. ***2011***, 133, *595–602.*

[84] *M. J. Kale, T. Avanesian, P. Christopher,* ACS Catal. ***2014***, 4, *116–128.*

[85] *J. R. Adleman, D. A. Boyd, D. G. Goodwin, D. Psaltis,* Nano Lett. ***2009***, 9, *4417–4423.*

[86] *M. K. Kumar, S. Krishnamoorthy, L. K. Tan, S. Y. Chiam, S. Tripathy, H. Gao,* ACS Catal. ***2011***, 1, *300–308.*

[87] *G. Decher,* Science (80). ***1997***, 277, *1232–1237.*

[88] *G. Decher, J. B. Schlenoff,* Multilayer Thin Films, *Wiley-VCH Verlag GmbH & Co. KGaA, Weinheim, Germany,* ***2012***.

[89] *P. Podsiadlo, M. Michel, J. Lee, E. Verploegen, N. Wong Shi Kam, V. Ball, J. Lee, Y. Qi, A. J. Hart, P. T. Hammond, et al.,* Nano Lett. ***2008***, 8, *1762–1770.*

[90] *S. Srivastava, N. A. Kotov,* Acc. Chem. Res. ***2008***, 41, *1831–1841.*

[91] *D. I. Gittins, F. Caruso,* J. Phys. Chem. B ***2001***, 105, *6846–6852.*

[92] *N. Kato, P. Schuetz, A. Fery, F. Caruso,* Macromolecules ***2002***, 35, *9780–9787.*

[93] *G. F. Schneider, G. Decher,* Nano Lett. ***2008***, 8, *3598–604.*

[94] *A. P. R. Johnston, C. Cortez, A. S. Angelatos, F. Caruso,* Curr. Opin. Colloid Interface Sci. ***2006***, 11, *203–209.*

[95] *G. Schneider, G. Decher,* Langmuir ***2008***, 24, *1778–1789.*

[96] *C. Peng, Electrostatic Layer-by-Layer Assembly of Hybrid Thin Films Using Polyelectrolytes and Inorganic Nanoparticles. PhD Thesis, Georgia Institute of Technology, USA,* ***2011***.

[97] *J. J. Richardson, D. Teng, M. Björnmalm, S. T. Gunawan, J. Guo, J. Cui, G. V. Franks, F. Caruso,* Langmuir ***2014***, 30, *10028–10034.*

[98] *M. Björnmalm, A. Roozmand, K. F. Noi, J. Guo, J. Cui, J. J. Richardson, F. Caruso,* Langmuir ***2015***, 31, *9054–9060.*

[99] *S. Xing, L. H. Tan, M. Yang, M. Pan, Y. Lv, Q. Tang, Y. Yang, H. Chen,* J. Mater. Chem. ***2009***, 19, *3286.*

[100] *W. W. Focke, G. E. Wnek, Y. Wei,* J. Phys. Chem. ***1987***, 91, *5813–5818.*

[101] *P. M. McManus, R. J. Cushman, S. C. Yang,* J. Phys. Chem. ***1987***, 91, *744–747.*

[102] *I. Sapurina, J. Stejskal,* Polym. Int. ***2008***, 57, *1295–1325.*

[103] *H. A. Atwater, A. Polman,* Nat. Mater. ***2010***, 9, *205–13.*

[104] *S. W. Verbruggen, M. Keulemans, B. Goris, N. Blommaerts, S. Bals, J. A. Martens, S. Lenaerts,* Appl. Catal. B Environ. ***2016***, 188, *147–153.*

[105] *P. Christopher, D. B. Ingram, S. Linic,* J. Phys. Chem. C ***2010***, 114, *9173–9177.*

[106] *W. Li, P. H. C. Camargo, L. Au, Q. Zhang, M. Rycenga, Y. Xia,* Angew. Chemie Int. Ed. ***2010***, 49, *164–168.*

[107] *J. N. Anker, W. P. Hall, O. Lyandres, N. C. Shah, J. Zhao, R. P. Van Duyne,* Nat. Mater. ***2008***, 7, *442–53.*

[108] *S. W. Verbruggen, M. Keulemans, J. A. Martens, S. Lenaerts,* J. Phys. Chem. C ***2013***, 117, *19142–19145.*

[109] *M. Liong, S. Angelos, E. Choi, K. Patel, J. F. Stoddart, J. I. Zink,* J. Mater. Chem. ***2009***, 19, *6251.*

[110] *D. Radziuk, H. Moehwald,* Phys. Chem. Chem. Phys. ***2015***, 17, *21072–21093.*

[111] *X. Liu, M. Atwater, J. Wang, Q. Huo,* Colloids Surf. B. Biointerfaces ***2007***, 58, *3–7.*

[112] *F. Caruso,* Adv. Mater. ***2001***, 13, *11–22.*

[113] *G. Schneider, G. Decher,* Nano Lett. ***2004***, 4, *1833–1839.*

[114] *O. Tzhayik, P. Sawant, S. Efrima, E. Kovalev, J. T. Klug,* Langmuir ***2002***, 18, *3364–3369.*

[115] *W. Wang, S. Efrima, O. Regev,* Langmuir ***1998***, 7463, *602–610.*

[116] *L. Kvítek, A. Panáček, J. Soukupová, M. Kolář, R. Večeřová, R. Prucek, M. Holecová, R. Zbořil,* J. Phys. Chem. C ***2008***, 112, *5825–5834.*

[117] *T.-M. Liu, J. Yu, C. A. Chang, A. Chiou, H. K. Chiang, Y.-C. Chuang, C.-H. Wu, C.-H. Hsu, P.-A. Chen, C.-C. Huang,* Sci. Rep. ***2015***, 4, *5593.*

[118] *Y. Zhang, L. Wang, J. Tian, H. Li, Y. Luo, X. Sun,* Langmuir ***2011***, *2170–2175.*

[119] *X. Sun, Y. Li,* Langmuir ***2005***, 21, *6019–6024.*

[120] *J. C. Flores, V. Torres, M. Popa, D. Crespo, J. M. Calderón-Moreno,* J. Non. Cryst. Solids ***2008***, 354, *5435–5439.*

[121] *M. Lisunova, M. Mahmoud, N. Holland, Z. A. Combs, M. A. El-Sayed, V. V Tsukruk,* J. Mater. Chem. ***2012***, 22, *16745–16753.*

[122] *N. G. Bastús, F. Merkoçi, J. Piella, V. Puntes,* Chem. Mater. ***2014***, 26, *2836–2846.*

[123] *T. Tytgat, B. Hauchecorne, M. Smits, S. W. Verbruggen, S. Lenaerts,* J. Lab. Autom. ***2012***, 17, *134–43.*

[124] *S. W. Verbruggen, S. Deng, M. Kurttepeli, D. J. Cott, P. M. Vereecken, S. Bals, J. A. Martens, C. Detavernier, S. Lenaerts,* Appl. Catal. B Environ. ***2014***, 160–161, *204–210.*

[125] *N. Claes, R. Asapu, N. Blommaerts, S. W. Verbruggen, S. Lenaerts, S. Bals,* Nanoscale ***2018***, 10, *9186–9191.*

[126] *Y. Han, R. Lupitskyy, T. M. Chou, C. M. Stafford, H. Du, S. Sukhishvili,* Anal. Chem. ***2011***, 83, *5873–5880.*

[127] *R. Sachan, V. Ramos, A. Malasi, S. Yadavali, B. Bartley, H. Garcia, G. Duscher, R. Kalyanaraman,* Adv. Mater. ***2013***, 25, *2045–2050.*

[128] *V. Bliznyuk, Y. Galabura, R. Burtovyy, P. Karagani, N. Lavrik, I. Luzinov,* Phys. Chem. Chem. Phys. ***2014***, 16, *1977–1986.*

[129] *V. Iliev, D. Tomova, L. Bilyarska, A. Eliyas, L. Petrov,* Appl. Catal. B Environ. ***2006***, 63, *266–271.*

[130] *G. Mie,* Ann. Phys. ***1908***, 330, *377–445.*

[131] *J. R. Adleman, Plasmonic Nanoparticles for Optofluidic Applications. PhD Thesis, California Institute for Technology, USA,* ***2009***.

[132] *P. B. Johnson, R. W. Christy,* Phys. Rev. B ***1972***, 6, *4370–4379.*

[133] *E. D. Palik, G. Ghosh,* Handbook of Optical Constants of Solids, *Academic Press,* ***1998***.

[134] *K. Ripken,* Zeitschrift für Phys. ***1972***, 250, *228–234.*

[135] *D. J. Segelstein, The Complex Refractive Index of Water. Masters Thesis, University of Missouri Kansas City, Missouri, USA,* ***1981***.

[136] *K.-H. Kyung, K. Fujimoto, S. Shiratori,* Jpn. J. Appl. Phys. ***2011***, 50, *035803.*

[137] *Y. Kim, R. C. Johnson, J. Li, J. T. Hupp, G. C. Schatz,* Chem. Phys. Lett. ***2002***, 352, *421–428.*

[138] *W. Haiss, N. T. K. Thanh, J. Aveyard, D. G. Fernig,* Anal. Chem. ***2007***, 79, *4215–4221.*

[139] COMSOL Multiphysics® v. 5.3 COMSOL Inc., *Stockholm, Sweden,* ***2017***.

[140] *A. A. Schmidt, J. Offermann, R. Anton,* Thin Solid Films ***1996***, 281–282, *105–107.*

[141] *L. A. A. Pettersson, P. G. Snyder,* Thin Solid Films ***1995***, 270, *69–72.*

[142] *T. Hutter, F. M. Huang, S. R. Elliott, S. Mahajan,* J. Phys. Chem. C ***2013***, 117, *7784–7790.*

[143] *J. L. West, N. J. Halas,* Annu. Rev. Biomed. Eng. ***2003***, 5, *285–292.*

[144] *A. J. Haes, C. L. Haynes, A. D. McFarland, G. C. Schatz, R. P. Van Duyne, S. Zou,* MRS Bull. ***2005***, 30, *368–375.*

[145] *N. G. Khlebtsov,* Quantum Electron. ***2008***, 38, *504–529.*

[146] *K. A. Willets, R. P. Van Duyne,* Annu. Rev. Phys. Chem. ***2007***, 58, *267–297.*

[147] *D. B. Ingram, Composite Silver / Titania Photocatalysts for Visible Light Water Splitting: The Role of Silver Surface Plasmons. PhD Thesis, University of Michigan, USA,* ***2011****.*

[148] *M. D. Brown, T. Suteewong, R. S. S. Kumar, V. D'Innocenzo, A. Petrozza, M. M. Lee, U. Wiesner, H. J. Snaith,* Nano Lett. ***2011****,* 11*, 438–445.*

[149] *M. Sharma, P. R. Pudasaini, F. Ruiz-Zepeda, E. Vinogradova, A. A. Ayon,* ACS Appl. Mater. Interfaces ***2014****,* 6*, 15472–15479.*

[150] *S. Sandén, K. Akitsu, B. Törngren, A. Ylinen, J. H. Smått, T. Kubo, M. Matsumura, N. Otani, H. Segawa, R. Österbacka,* J. Phys. Chem. C ***2015****,* 119*, 5570–5576.*

[151] *B. Sharma, R. R. Frontiera, A.-I. Henry, E. Ringe, R. P. Van Duyne,* Mater. Today ***2012****,* 15*, 16–25.*

[152] *S. Schlücker,* Angew. Chemie - Int. Ed. ***2014****,* 53*, 4756–4795.*

[153] *A. D. McFarland, M. A. Young, J. A. Dieringer, R. P. Van Duyne,* J. Phys. Chem. B ***2005****,* 109*, 11279–11285.*

[154] *N. Leopold, B. Lendl,* J. Phys. Chem. B ***2003****,* 107*, 5723–5727.*

[155] *P. L. Stiles, J. A. Dieringer, N. C. Shah, R. P. Van Duyne,* Annu. Rev. Anal. Chem. ***2008****,* 1*, 601–626.*

[156] *J. A. Dieringer, A. D. McFarland, N. C. Shah, D. A. Stuart, A. V Whitney, C. R. Yonzon, M. A. Young, X. Zhang, R. P. Van Duyne,* Faraday Discuss. ***2006****,* 132*, 9–26.*

[157] *D.-K. Lim, K.-S. Jeon, H. M. Kim, J.-M. Nam, Y. D. Suh,* Nat. Mater. ***2010****,* 9*, 60–67.*

[158] *R. Liu, B. Liu, G. Guan, C. Jiang, Z. Zhang,* Chem. Commun. (Camb). ***2012****,* 48*, 9421–3.*

[159] *E. J. Blackie, E. C. Le Ru, P. G. Etchegoin,* J. Am. Chem. Soc. ***2009****,* 131*, 14466–14472.*

[160] *H. Xu, J. Aizpurua, M. Käll, P. Apell,* Phys. Rev. E - Stat. Physics, Plasmas, Fluids, Relat. Interdiscip. Top. ***2000****,* 62*, 4318–4324.*

[161] *S. L. Kleinman, R. R. Frontiera, A.-I. Henry, J. a Dieringer, R. P. Van Duyne,* Phys. Chem. Chem. Phys. ***2013****,* 15*, 21–36.*

[162] *W. Li, P. H. C. Camargo, X. Lu, Y. Xia,* Nano Lett. ***2009****,* 9*, 485–490.*

[163] *D. Radziuk, H. Möhwald,* ACS Nano ***2015****,* 9*, 2820–2835.*

[164] *G. H. Chan, J. Zhao, E. M. Hicks, G. C. Schatz, R. P. Van Duyne,* Nano Lett. ***2007****,* 7*, 1947–1952.*

[165] *K. G. Stamplecoskie, J. C. Scaiano, V. S. Tiwari, H. Anis,* J. Phys. Chem. C ***2011****,* 115*, 1403–1409.*

[166] *R. Gill, L. J. Tian, W. R. C. Somerville, E. C. Le Ru, H. van Amerongen, V. Subramaniam,* J. Phys. Chem. C ***2012****,* 116*, 16687–16693.*

[167] *P. White, J. Hjortkjaer,* J. Raman Spectrosc. ***2014****,* 45*, 32–40.*

[168] *M. Erol, Y. Han, S. K. Stanley, C. M. Stafford, H. Du, S. Sukhishvili,* J. Am. Chem. Soc. ***2009***, 131, *7480–7481.*

[169] *D. Yang, L. Xia, H. Zhao, X. Hu, Y. Liu, J. Li, X. Wan,* Chem. Commun. ***2011***, 47, *5873–5875.*

[170] *D. Li, S. Wu, Q. Wang, Y. Wu, W. Peng, L. Pan,* J. Phys. Chem. C ***2012***, 116, *12283–12294.*

[171] *G. V. Naik, V. M. Shalaev, A. Boltasseva,* Adv. Mater. ***2013***, 25, *3264–3294.*

[172] *R. Asapu, N. Claes, S. Bals, S. Denys, C. Detavernier, S. Lenaerts, S. W. Verbruggen,* Appl. Catal. B Environ. ***2017***, 200, *31–38.*

[173] *J. Turkevich,* Gold Bull. ***1985***, 18, *125–131.*

[174] *G. Frens,* Nat. Phys. Sci. ***1973***, 241, *20–22.*

[175] *A. J. Bain, P. Chandna, G. Butcher, J. Bryant,* J. Chem. Phys. ***2000***, 112, *10435–10449.*

[176] *E.-O. Ganbold, J.-H. Park, U. Dembereldorj, K.-S. Ock, S.-W. Joo,* J. Raman Spectrosc. ***2011***, 42, *1614–1619.*

[177] *Y. Fang, N.-H. Seong, D. D. Dlott,* Science (80). ***2008***, 321, *388–392.*

[178] *D. M. Solís, J. M. Taboada, F. Obelleiro, L. M. Liz-Marzán, F. J. García de Abajo,* ACS Nano ***2014***, 8, *7559–7570.*

[179] *P. Nordlander, C. Oubre, E. Prodan, K. Li, M. I. Stockman,* Nano Lett. ***2004***, 4, *899–903.*

[180] *J.-H. Tian, B. Liu, Li, Z.-L. Yang, B. Ren, S.-T. Wu, Tao, Z.-Q. Tian,* J. Am. Chem. Soc. ***2006***, 128, *14748–14749.*

[181] *K. Kneipp, M. Moskovits, H. Kneipp, Eds.* , Surface-Enhanced Raman Scattering, *Springer-Verlag Berlin Heidelberg, Berlin,* ***2006****.*

[182] *C. E. Talley, J. B. Jackson, C. Oubre, N. K. Grady, C. W. Hollars, S. M. Lane, T. R. Huser, P. Nordlander, N. J. Halas,* Nano Lett. ***2005***, 5, *1569–1574.*

[183] *S. Yanagida, Y. Kosakai, A. Yasumori,* Colloids Surfaces A Physicochem. Eng. Asp. ***2014***, 456, *55–61.*

[184] *C. Fang, H. Jia, S. Chang, Q. Ruan, P. Wang, T. Chen, J. Wang,* Energy Environ. Sci. ***2014***, 7, *3431–3438.*

[185] *A. Tanaka, A. Ogino, M. Iwaki, K. Hashimoto, A. Ohnuma, F. Amano, B. Ohtani, H. Kominami,* Langmuir ***2012***, 28, *13105–13111.*

[186] *I. Caretti, M. Keulemans, S. W. Verbruggen, S. Lenaerts, S. Van Doorslaer,* Top. Catal. ***2015***, 58, *776–782.*

[187] *M. Becker, T. Stelzner, a. Steinbrück, a. Berger, J. Liu, D. Lerose, U. Gösele, S. Christiansen,* ChemPhysChem ***2009***, 10, *1219–1224.*

[188] *G. Schneider, G. Decher, N. Nerambourg, R. Praho, M. H. V. Werts, M. Blanchard-Desce,* Nano Lett. ***2006***, 6*, 530–536.*

[189] *C. Caucheteur, T. Guo, J. Albert,* Anal. Bioanal. Chem. ***2015***, 407*, 3883–3897.*

[190] *M. C. Daniel, D. Astruc,* Chem. Rev. ***2004***, 104*, 293–346.*

[191] *S. Sakthivel, M. V. Shankar, M. Palanichamy, B. Arabindoo, D. . Bahnemann, V. Murugesan,* Water Res. ***2004***, 38*, 3001–3008.*

[192] *D. Tsukamoto, Y. Shiraishi, Y. Sugano, S. Ichikawa, S. Tanaka, T. Hirai,* J. Am. Chem. Soc. ***2012***, 134*, 6309–6315.*

[193] *V. Iliev, D. Tomova, L. Bilyarska, G. Tyuliev,* J. Mol. Catal. A-Chemical ***2007***, 263*, 32–38.*

[194] *S. Mukherjee, F. Libisch, N. Large, O. Neumann, L. V. Brown, J. Cheng, J. B. Lassiter, E. A. Carter, P. Nordlander, N. J. Halas,* Nano Lett. ***2013***, 13*, 240–247.*

[195] *S. K. Cushing, J. Li, F. Meng, T. R. Senty, S. Suri, M. Zhi, M. Li, A. D. Bristow, N. Wu,* J. Am. Chem. Soc. ***2012***, 134*, 15033–15041.*

[196] *A. Mills, J. Wang,* J. Photochem. Photobiol. A Chem. ***2006***, 182*, 181–186.*

[197] *A. Mills, C. Hill, P. K. J. Robertson,* J. Photochem. Photobiol. A Chem. ***2012***, 237*, 7–23.*

[198] *D. C. Hurum, A. G. Agrios, K. A. Gray, T. Rajh, M. C. Thurnauer,* J. Phys. Chem. B ***2003***, 107*, 4545–4549.*

[199] *F. J. Knorr, D. Zhang, J. L. McHale,* Langmuir ***2007***, 23*, 8686–8690.*

[200] *Y. Yang, T. Zhang, L. Le, X. Ruan, P. Fang, C. Pan, R. Xiong, J. Shi, J. Wei,* Sci. Rep. ***2015***, 4*, 7045.*

[201] *C. M. G. S. Cruz,* J. Electroanal. Chem. ***1997***, 428*, 185–192.*

[202] *T. Barman, A. A. Hussain, B. Sharma, A. R. Pal,* Sci. Rep. ***2016***, 5*, 18276.*

[203] *U. Kreibig, C. v. Fragstein,* Zeitschrift für Phys. ***1969***, 224*, 307–323.*

[204] *J. Toster, Q. L. Zhou, N. M. Smith, K. S. Iyer, F. Rosei, C. L. Raston,* Green Chem. ***2013***, 15*, 2060.*

[205] *A. Biswas, H. Eilers, F. Hidden, O. C. Aktas, C. V. S. Kiran,* Appl. Phys. Lett. ***2006***, 88*, 013103.*

Curriculum Vitae

Personal Information

Name	Ramesh Asapu
Place of birth	Visakhapatnam, Andhra Pradesh (Province)
Nationality	India
Permanent Address	58-30-88/2, Sakethapuram, NAD Post Visakhapatnam, Andhra Pradesh, India 530009
E-mail (personal)	ramesh.asapu@gmail.com
Telephone	+32 483050114 (Belgium), +91 8374542820 (India)

Education

2014 - 2018 PhD in Bioscience Engineering, University of Antwerp
Sustainable Energy, Air and Water Technology (DuEL) Lab.

Funding projects: FOTOKAT (collaboration between Gent University, University of Antwerp and KU Leuven) and GOA (Collaboration between EMAT, DuEL and LADCA research groups)

2008 - 2010 Master of Engineering Science, Chemical Engineering,
Lamar University, Texas, USA. GPA: 4.0/4.0

Thesis: Synthesis of phosphorus doped titania nanotubes and assembly of multilayered titania films.

2003 - 2007 Bachelor of Technology, Chemical Engineering,
MVGR College of Engineering, JNTU, India. Aggregate 78%

Professional Experience

2011 Feb. – 2011 Aug. Graduate Engineer Trainee
Plant Commissioning – Batch reactors, Project Department
SNF (India), SNF Floerger Group, Visakhapatnam, India

2011 Sep. – 2014 Nov. Engineer
HVAC Dynamic Simulations Team
Mercedes-Benz R&D India, Daimler AG., Bengaluru, India

Publications

R. Asapu, N. Claes, S. Bals, S. Denys, C. Detavernier, S. Lenaerts, S.W. Verbruggen, Silver-polymer core-shell nanoparticles for ultrastable plasmon-enhanced photocatalysis, Appl. Catal. B Environ. 200 (2017) 31–38.

R. Asapu, R-G. Ciocarlan, N. Claes, N. Blommaerts, M.M. Minjauw, T. Ahmad, J. Dendooven, P. Cool, S. Bals, S. Denys, C. Detavernier, S. Lenaerts, S.W. Verbruggen, Plasmonic near-field localization of silver core-shell nanoparticle assemblies via wet chemistry nanogap engineering, ACS Appl. Mater. Interfaces. (2017) acsami.7b13965.

N. Blommaerts, **R. Asapu**, N. Claes, S. Bals, S. Lenaerts, S.W. Verbruggen, Gas phase photocatalytic spiral reactor for fast and efficient pollutant degradation, Chem. Eng. J. 316 (2017) 850–856.

N. Claes, **R. Asapu**, N. Blommaerts, S.W. Verbruggen, S. Lenaerts, S. Bals, Characterization of silver-polymer core-shell nanoparticles using electron microscopy., Nanoscale. 10 (2018), 9186-9191.

M.M. Minjauw, E. Solano, S.P. Sree, **R. Asapu**, M. Van Daele, R.K. Ramachandran, G. Heremans, S.W. Verbruggen, S. Lenaerts, J.A. Martens, C. Detavernier, J. Dendooven, Plasma-Enhanced Atomic Layer Deposition of Silver Using Ag(fod)(PEt_3) and NH_3-Plasma, Chem. Mater. 29 (2017) 7114–7121.

R. Asapu, V.M. Palla, B. Wang, Z. Guo, R. Sadu, D.H. Chen, Phosphorus-doped titania nanotubes with enhanced photocatalytic activity, J. Photochem. Photobiol. A Chem. 225 (2011) 81–87.

S. Wei, P. Mavinakuli, Q. Wang, D. Chen, **R. Asapu**, Y. Mao, N. Haldolaarachchige, D.P. Young, Z. Guo, Polypyrrole-Titania Nanocomposites Derived from Different Oxidants, J. Electrochem. Soc. 158 (2011) K205.

Conference Proceedings

Oral Presentations

R. Asapu, R-C. George, N. Claes, N. Blommaerts, P. Cool, S. Bals, S. Denys, S. W. Verbruggen, S. Lenaerts. Nanogaps in Ag and Au nanoparticle clusters: A crucial parameter for SERS application. 19th Netherlands Catalysis and Chemistry Conference (NCCC), Noordwijkerhout, The Netherlands (05/03/2018 – 07/03/2018)

R. Asapu, S. W. Verbruggen, N. Claes, S. Bals, S. Denys, S. Lenaerts. Near-Field FEM Simulations: A Vital Tool for Studying Silver-Based Plasmonic Systems. COMSOL Conference 2016, Munich, Germany (12/10/2016-14/10/2016)

R. Asapu, R. Ciocarlan, N. Claes, N. Blommaerts, S. Bals, P. Cool, S. Denys, S. W. Verbruggen, S. Lenaerts. Evaluating Nanogaps in Ag and Au Nanoparticle Clusters for SERS Applications Using COMSOL Multiphysics®. COMSOL Conference 2017, Rotterdam, The Netherlands (18/10/2017-20/10/2017)

Poster Presentations

R. Asapu, S.W. Verbruggen, N. Claes, S. Bals, S. Denys and S. Lenaerts. Ultrastable silver-polymer core-shell nanoparticles for plasmonic applications. MELiSSA mini-symposium & master class, Antwerp - Belgium (30/03/2017)

R. Asapu, Sammy Verbruggen, Nathalie Claes, Sara Bals, Siegfried Denys, Silvia Lenaerts. Ultrastable Silver-polymer core-shell nanoparticles for plasmonic applications. Chemical Research in Flanders (CRF-1), Blankenberge – Belgium (24/10/16 – 26/10/16)

R. Asapu, N. Claes, S. Bals, S. Denys, S.W. Verbruggen and S. Lenaerts, Stability of silver modified TiO2 thin films for gas phase photocatalysis. 17th Netherlands Catalysis and Chemistry Conference (NCCC), Noordwijkerhout, The Netherlands (07/03/2016 - 09/03/2016)